High-order solution of elliptic partial differential equations in domains containing conical singularities

Thesis by

Zhiyi Li

In Partial Fulfillment of the Requirements

for the Degree of

Doctor of Philosophy

California Institute of Technology

Pasadena, California

2009

(Defended July 28, 2008)

Acknowledgments

The work performed in this thesis is largely due to the inspiration and guidance provided by my advisor, Professor Oscar P. Bruno. I would like to thank him very much for his kind and professional advice on my research over the last few years. In addition, throughout the computational work performed in this thesis, I used a code written by Professor Christophe Geuzaine for solution of integral equations on a smooth surface, and received countless suggestions from Tim Elling and Randy Paffenroth, for which I feel grateful. I would also like to thank the staff members of the Applied and Computational Mathematics department, Sydney Garstang, Chad Schumtzer, and Sheila Shull for all their help, as well as my thesis committee members, Professors Oscar P. Bruno, Thomas Y. Hou, Peter Schröder and Joseph E. Shepherd for their time and effort. Finally, I would like to acknowledge the excellent study environment that Caltech provides for all students, and many people in the school who have influenced me.

Abstract

In this thesis we introduce an algorithm, based on the boundary integral equation method, for the numerical evaluation of singular solutions of the Laplace equation in three dimensional space, with singularities induced by a conical point on an otherwise smooth boundary surface. This is a model version of a fundamental problem in science and engineering: accurate evaluation of solutions of Partial Differential Equations in domains whose boundaries contain geometric singularities. For simplicity we assume a small region near the conical point coincides with a straight cone of given cross section; otherwise the boundary surface is not restricted in any way. Our numerical results demonstrate excellent convergence as discretizations are refined, even at the singular point where the solutions tend to infinity.

Contents

List of Figures

List of Tables

Chapter 1

Introduction

The problem of evaluating numerical solutions of Partial Differential Equations (PDE) under conditions that give rise to solution singularities (such as reduced differentiability and even blow up of the solutions themselves) is one of fundamental importance in science and engineering. Yet, a wide variety of such problems have not been adequately addressed from a computational perspective. In this thesis we consider a central and prototypical problem of this type, namely, solution of Laplace's equation in domains containing conical singularities. Many other problems in domains containing conical singularities, including problems of wave propagation and scattering, electromagnetics, diffraction, solid mechanics and acoustics, can be tackled by similar techniques; further, many of the ideas developed in this text can be applied to other types of geometric singularities, including edge and polyhedral singularities. As mentioned above, however, our presentation will be restricted to the fundamental example provided by the Laplace equation in domains which, containing conical singularities, are otherwise smooth.

In Section 1.1 we mention a class of engineering and scientific problems closely related to the PDE conical-singularity problem considered in this thesis. In Section 1.2 we present some background concerning singular integral equation formulations, and in Section 1.3 we then outline our new approach for the solution of conical-singularity problems—presenting illustrative examples that demonstrate, in simple contexts, the character and main elements of our methodology. A detailed presentation of this methodology, including a variety of numerical results, is then presented in Chapters 2 through 7; an outline of the contents of these chapters is presented in Section 1.4.

1.1 Background

As indicated above, a wide variety of areas of science and engineering give rise to problems containing geometric singularities of the type considered in this thesis. In fracture mechanics, for example, treatments are often needed for interior and surface flaws that are often found in solid structures. Analysis leading to predictions of whether these flaws may grow and become liable to produce catastrophic failure of the structure, are, clearly, of great importance. Mathematically, the stress field σ, a quantity that derives from solution of a system of PDEs akin to Laplace's equation, becomes infinite at the crack-tips—thus giving rise to singular problems closely related to the main model problem considered in this thesis [18, 21, 25, 35]. In aerodynamics, in turn, the problem of evaluating the flow around an airfoil is one of great interest. In an inviscid fluid, the speed of air around the trailing edge of a moving airfoil can be infinite. Of course, in a real fluid, air does not move infinitely fast, but strong viscous forces are caused near the trailing edge: vortexes are accumulated and carried along with the moving airfoil, until a stagnation point moves to the trailing edge, and the Kutta condition is satisfied. In any case, generally, solution of the Laplace equation in singular domains arising from airfoil and wing geometries is of significant importance in theoretical and computational aerodynamics [8, 28].

Problems of diffraction of acoustic and electromagnetic waves by domains containing geometric singularities arise in a wide range of contexts—including optics, remote sensing, antenna design, electromagnetic compatibility, etc. In the optics case, for example, diffraction effects such as those originating at geometric singularities set a fundamental limit to the resolution of camera, telescope, or microscope. It is to be noted that, as is the case in the Laplace problems considered in this thesis, at sharp edges of the diffracting obstacle, the electromagnetic field vectors become infinite [14, 41].

In view of these and other scientific applications, the problem of evaluating numerically solutions of PDEs akin to the Laplace equation in geometries containing geometric singularities has drawn significant attention from the mathematics community: singular solutions induced by non-smooth domains have been actively studied in the last few decades. Theoretical contributions such as the ones in References [1, 11–13, 19, 22, 37, 42, 43] discuss singularity structures and degrees of smoothness expected in solutions around singular points. Refer-

ence [30] provides a theoretical analysis of the behavior of solutions for Laplace equations in polyhedral domains.

Significant contributions regarding the numerical solutions of such problems have been put forward as well. For the sake of completenes we first mention references concerning 2D elliptic equations with singular boundaries, although, we must note, problems in 2D are significantly simpler than their 3D counterparts. Early 2D contributions, in which the problem is approached through use of spatially refined meshes in the singularity region include [3, 4, 15–17]; References [20, 24, 29, 40], in turn, use singular basis functions as part of finite element spaces. A different approach, which is well suited to the two-dimensional context, is proposed in References [26, 44, 45]: A separation of the domain near the geometrical singularity is introduced, and "DtN" conditions are imposed on the artificial boundary. Other recent contributions include [38] (which gives a method for evaluation of the number of singular terms for a two-dimensional elasticity problem with two different wedge-shaped elastic materials bonded together along a common edge and subject to tractions on the boundary); Reference [46] (which uses the infinite element method to obtain singular solutions of the Helmholtz equation), and [36] (which, using the infinite element method, seeks solutions for composite-material problem with singular interfaces); References [2, 7] (which treat elliptic equations with boundary singularities using the singular complement method); Reference [23, 27] (which provides high-order integral equation methods for elliptic equations), and Reference [23] (which provides a comparison of a method based on use of special basis functions with an approach based on adaptive mesh refinement); and finally, Reference [33] (which treats the Maxwell equations with boundary singularities, using the Fourier finite element method).

We now mention some important references for the 3D case. We first consider Reference [32], in which Laplace equation with conical boundary points is considered; in this work the solution of these problems are decomposed into the singular components and a smoother remainder. This contribution also provides us with an analytical formula for the order of singularity for a straight circular cone surface. Reference [5] also considers the Laplace equation, and assumes bounding geometries containing both conical points and edges. In this reference a Steklov problem is used to compute the order of singularity, while finite element methods of various types are otherwise used to evaluate solutions. Reference [39] describes

an approximate asymptotic method, valid in the high-frequency regime, for evaluation of the scattering of a plane polarized electromagnetic wave by a perfectly conducting cone. Reference [31] studies the boundary element method for integral equations of the first kind in 2D and 3D for problems of scattering. Reference [34] treats the Maxwell equations with boundary singularities, using the Fourier finite element method.

As mentioned above, in this thesis we address one of the main problems in this area, namely, solutions of elliptic equations around *conical singularities;* as shown in what follows, our work resulted in solvers that can produce solution to 3D problems containing conical singularities with a high order of accuracy obtained. In detail, our work focuses on Laplace equation with constant coefficients;

$$\begin{cases} \Delta u = 0 & \text{in } D \\ u = f \quad \text{or} \quad \frac{\partial u}{\partial n} = g & \text{on } \partial D, \end{cases} \tag{1.1}$$

in domains whose boundaries contain conical points. The solution u of such a problem is smooth for smooth boundaries; in presence of boundary singularities, however, the solution becomes singular itself. In many cases, a straightforward numerical implementation of such problems (e.g., a finite element, variational formulation or a direct quadrature rule for an equivalent integral equation) will give rise to poor accuracies, as a result of the singular characteristics inherited by the solution. An extension of these methods with more complicated basis functions does tend to produce beneficial effects, but, as suggested in what follows, previous contributions in these regards leave significant room for improvement. In Reference [5], for example, the hp-version of the finite element method is used to compute singular solutions of Laplace's equation. A full implementation is given for the case in which the solution is bounded, and for which a mild singularity takes the form of a relatively small but positive power of the distance from the conical point. This positive power is evaluated by means of a Steklov problem; in addition to this exponent, only values of average quantities such as mean square norms and vertex intensity-factors are reported—no indications are given in this contribution of the errors arising in the solution itself. Other algorithms have also been developed in References [30, 32]. Once again, these methods are only implemented for rather special cases, or only report on a few particular quantities (such as the intensity factor) but not on the full solutions. As we shall show, the contributions introduced in this

thesis give rise to significant improvements in the numerical accuracy of the singular components and the full solution—*even for cases containing negative exponents for which integral densities blow up at the singular point*. These integral densities correspond to physically meaningful quantities such as solution derivatives or, in the electromagnetic case, to the electrical current itself. To the best of our knowledge, this is the first contribution enabling accurate numerical evaluation of such types of singularities for solution of PDEs in domains bounded by closed singular boundaries.

The approach introduced in this thesis is based on consideration of integral equations and algorithms that can provide high-order accuracy for approximation of singular integrals. To achieve such high accuracies our methods proceed by first splitting off the most singular part of the solution. These singular parts are determined by means of a novel (surface) nonlinear eigenvalue problem which, to the best of our knowledge, has not been considered previously. Our algorithm then proceeds to evaluate integrals whose integrands involve such singular functions. Evaluation of these integrals amounts to a rather challenging problem; in our approach these quantities are obtained, with high order accuracy, by means of appropriate series expansions we developed. With singular parts pulled out, the remaining relatively smooth(er) part of the solution can be computed by means of an application of high-order quadrature rules based on the use of graded meshes around the singular points. With this high order quadrature rule in place, our algorithm proceeds to formulate the full discrete linear-algebra problem, which is solved by means of the iterative linear-algebra solver GMRES. As shown in Chapter 4, finally, a small modification of the integral operator can be used to reduce the number of iterations required by the iterative linear-algebra solver to fully separate the singular parts from the smooth parts of the solution.

1.2 Integral equation formulations

The method of boundary integral equations is commonly used in the solution of boundary problems of mathematical physics, including the two main boundary value problems for

Laplace equations that are considered in this thesis, namely

$$\begin{cases} \Delta u^i &= 0 \quad \text{in} \quad D^i \\ u^i &= f \quad \text{on} \quad \partial D \end{cases} \qquad \text{(Interior Dirichlet Problem)} \tag{1.2}$$

and

$$\begin{cases} \Delta v^e &= 0 \quad \text{in} \quad D^e \\ \frac{\partial v^e}{\partial n} &= g \quad \text{on} \quad \partial D \end{cases} \qquad \text{(Exterior Neumann Problem).} \tag{1.3}$$

Here D^i is a bounded region in $\mathbb{R}^3$; D^e is the exterior of D^i: $D^e = \mathbb{R}^3 \setminus \overline{D^i}$; n is an exterior normal to D^i; ∂D is the common boundary of D^i and D^e.

According to the method of boundary integral equations, the solutions u^i and v^e of the boundary problems (1.2) and (1.3) can be represented as double-layer and single-layer potentials with densities μ and ν:

$$u^i(\boldsymbol{x}) = \int_{\partial D} \frac{\partial G(\boldsymbol{x}, \boldsymbol{x}')}{\partial n_{\boldsymbol{x}'}} \cdot \mu(\boldsymbol{x}') dS(\boldsymbol{x}') \tag{1.4}$$

$$v^e(\boldsymbol{x}) = \int_{\partial D} G(\boldsymbol{x}, \boldsymbol{x}') \cdot \nu(\boldsymbol{x}') dS(\boldsymbol{x}') \tag{1.5}$$

where $G(\boldsymbol{x}, \boldsymbol{x}')$ is the Green's function of Laplace operator

$$G(\boldsymbol{x}, \boldsymbol{x}') = \frac{1}{4\pi|\boldsymbol{x} - \boldsymbol{x}'|},$$

and where the functions μ and ν are solutions to the following boundary integral equations on ∂D:

$$-\frac{\mu(\boldsymbol{x})}{2} + \int_{\partial D} \frac{\partial G(\boldsymbol{x}, \boldsymbol{x}')}{\partial n_{\boldsymbol{x}'}} \cdot \mu(\boldsymbol{x}') dS(\boldsymbol{x}') = f(\boldsymbol{x}) \quad \text{for } \boldsymbol{x} \in \partial D \tag{1.6}$$

$$-\frac{\nu(\boldsymbol{x})}{2} + \int_{\partial D} \frac{\partial G(\boldsymbol{x}, \boldsymbol{x}')}{\partial n_{\boldsymbol{x}}} \cdot \nu(\boldsymbol{x}') dS(\boldsymbol{x}') = g(\boldsymbol{x}) \quad \text{for } \boldsymbol{x} \in \partial D. \tag{1.7}$$

We note that the density functions μ and ν are connected with solutions of conjugate

problems:

$$\mu = u^e|_{\partial D} - f \tag{1.8}$$

$$\nu = (\frac{\partial v^i}{\partial n})|_{\partial D}, \tag{1.9}$$

where u^e and v^i are solutions of the conjugate problems

$$\begin{aligned} \Delta u^e = 0 \quad &\text{in } D^e, \quad \frac{\partial u^e}{\partial n} = \frac{\partial u^i}{\partial n} \quad \text{on } \partial D \\ \Delta v^i = 0 \quad &\text{in } D^i, \qquad v^i = v^e \qquad \text{on } \partial D. \end{aligned}$$

A proof of (1.8) and (1.9) can be found in [32].

The regularity properties (smoothness or lack thereof) of the solutions μ and ν determines to a significant extent the order of accuracy of a numerical solver for equations (1.2) and (1.3)—since the accuracies delivered by quadrature rules themselves depend on the integrand regularities. As is known, however, when the boundary ∂D has conical points, the integrands are not smooth around those points. For example, as shown in [32], the density function $\nu(\boldsymbol{x})$ in (1.7) tends to infinity at the conical point.

In what follows we develop a method for solution of PDE problems including a conical boundary point on the basis of equation (1.7). We point out that the Laplace equation with the Neumann boundary conditions can be solved by means of alternate integral equations, whose solution does not tend to infinity at the conical point. Indeed, the solution of the "direct" integral equation (see e.g., [9, 10]) equals the solution v^e of the Neumann problem and is thus bounded. In many circumstances, however, use of singular solutions and related quantities is unavoidable. The simplest example of this involves the evaluation of the normal derivative of the solution v^i of the interior Dirichlet problem which, according to equation (1.9) tends to infinity at the conical point—since so does ν. The present approach thus allows one to evaluate this meaningful physical quantity; clearly, solution of the alternate equation followed by differentiation would give rise to very poor results. An additional example results from consideration of the Maxwell equations, which include an equivalent of $\frac{\partial v^i}{\partial n}$ as a component of the unknown surface current along an edge. Thus, in addition to accurately producing the singular behavior of derivatives of solutions of the Laplace equation, the method in this thesis can be related to the problem of solving a PDE Maxwell system

around a conical point.

For simplicity, in this thesis we only consider a three dimensional body with one conical point, in a neighborhood of which the surface coincides with the boundary of a straight cone of arbitrary (smooth) cross section, as depicted in Figure 2.12. Generalization to a curved cone boundary surface should result as an extension of the method developed in this work.

1.2.1 Decomposition of the density function $\nu(\boldsymbol{x})$

In equation (2.5) we define the coordinates $(r_{\boldsymbol{x}}, \theta_{\boldsymbol{x}})$ on the integration surface ∂D near the conical point O: with an appropriate interpretation, implicit in (2.5), $r_{\boldsymbol{x}}$ denotes the distance from the conical point O and $\theta_{\boldsymbol{x}}$ is the azimuthal angle. These coordinates are depicted in Figure 2.12.

According to [32], we have an asymptotic expansion for $\nu(\boldsymbol{x})$ near the conical point:

$$\nu(\boldsymbol{x}) = \sum_i \frac{c_i a_i(\theta_{\boldsymbol{x}})}{r_{\boldsymbol{x}}^{q_i}} \hat{\omega}_{\mathcal{P}^1}(\boldsymbol{x}) + b(\boldsymbol{x}), \tag{1.10}$$

where

$$q_i > 0, \tag{1.11}$$

and where the function $b(\boldsymbol{x})$ is bounded throughout ∂D. (The definition for the terms in equation (1.11) is in equation (3.1))

Using the decomposition in equation (1.10), the integral in equation (1.7) becomes

$$\begin{aligned} &-\frac{\nu(\boldsymbol{x})}{2} + \int_{\partial D} \frac{\partial G(\boldsymbol{x}, \boldsymbol{x}')}{\partial n_{\boldsymbol{x}}} \cdot \nu(\boldsymbol{x}') dS(\boldsymbol{x}') \\ &= \sum_i \left(-\frac{c_i a_i(\theta_{\boldsymbol{x}})}{2 r_{\boldsymbol{x}}^{q_i}} \hat{\omega}_{\mathcal{P}^1}(\boldsymbol{x}) + \int_{\partial D} \frac{\partial G(\boldsymbol{x}, \boldsymbol{x}')}{\partial n_{\boldsymbol{x}}} \cdot \frac{c_i a_i(\theta_{\boldsymbol{x}'})}{r_{\boldsymbol{x}'}^{q_i}} \hat{\omega}_{\mathcal{P}^1}(\boldsymbol{x}') dS(\boldsymbol{x}') \right) \\ &\quad + \left(-\frac{b(\boldsymbol{x})}{2} + \int_{\partial D} \frac{\partial G(\boldsymbol{x}, \boldsymbol{x}')}{\partial n_{\boldsymbol{x}}} \cdot b(\boldsymbol{x}') dS(\boldsymbol{x}') \right). \end{aligned} \tag{1.12}$$

In the following chapters we develop a number of procedures for accurate evaluation of the right hand side of equation (1.12); note that this requires, in particular, evaluation of a *bounded difference of infinite quantities*; see Section 1.3.2 below for a simple example in these regards.

1.3 A new approach to the conical singularity problem: Preliminary examples

To demonstrate, in simple settings, some of the main issues that arise as we address the main problem considered in this thesis, in this section we present two elementary introductory examples. The purpose of this section is thus to provide an indication of the nature of the algorithms developed in the following chapters.

1.3.1 Example: Numerical integration with a singular integrand

Let's first consider an elementary integration problem:

$$\int_0^1 \frac{1}{\sqrt{x}} dx \tag{1.13}$$

This is a finite integral with infinite integrand near $x = 0$. The integrand, $f(x) = \frac{1}{\sqrt{x}}$ is shown in Figure (1.1) Left. A direct application of a quadrature rule such as the trapezoidal rule results in slow convergence as shown in the second column of Table 1.1. In order to address this difficulty we follow [9]: we use a change of variables $x = x(t)$, depicted in the middle portion of Figure 1.1, to obtain a new integrand $f(x(t))x'(t) = \frac{1}{\sqrt{x(t)}} \cdot x'(t)$, depicted in Figure 1.1 Right. One important feature of $x(t)$ is that $x(t) = t^n$ with $n > 2$ for t close 0. As a result of this property of $x(t)$, the integrand becomes

$$nt^{n-1} \cdot \frac{1}{t^{\frac{n}{2}}}$$

near $t = 0$. This new integrand is a smooth function, for n large enough this function vanishes as $t \to 0$ together with several of its derivatives. The function $x(t)$ increases smoothly to 1, and stays constant in an interval where t is close to 1. So $x'(t) = 0$ near $t = 1$ as well. Overall, the new integrand is smooth and vanishes near the two end points of the interval $t \in [0, 1]$ as depicted in Figure 1.1 Right. Using the change of variables $x = x(t)$, the integral (1.13) becomes

$$\int_0^1 \frac{1}{x(t)^{\frac{1}{2}}} x'(t) dt. \tag{1.14}$$

N	error without COV	error with COV
20	0.3016	0.0092
40	0.2184	-0.0014
80	0.1570	-6.3545e-6
160	0.1123	7.4472e-10
320	0.0801	2.4425e-15

Table 1.1: Error arising from the trapezoidal quadrature rule applied to the function $\frac{1}{\sqrt{x}}$ with and without the change of variables (COV) $x = x(t)$, and using N function values/quadrature points.

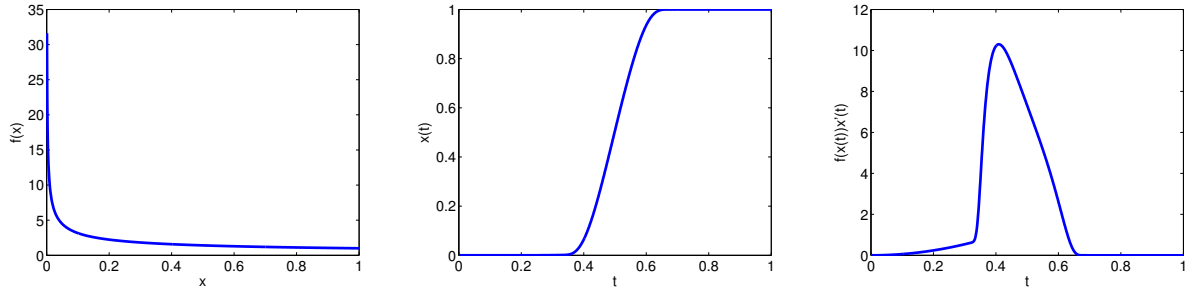

Figure 1.1: Left: Function $\frac{1}{\sqrt{x}}$. Middle: Change of variable function $x = x(t)$. Right: The integrand $\frac{1}{x(t)^{\frac{1}{2}}}x'(t)$ obtained after the change of variable $x(t)$

The trapezoidal rule provides excellent convergence for this new integral, as shown in the third column of Table 1.1. Similar changes of variable will be used in our algorithms to tackle problems of integration of unbounded functions *with finite integrals*.

Remark 1.3.1. *Changes of variables designed to produce smooth and periodic integrands play major roles in the algorithms developed in this thesis. Indeed, we transform all singular integrands into integrands that are smooth and periodic, for which the trapezoidal quadrature rule is highly (spectrally) accurate.*

1.3.2 Example: Resolution of a singular limit

Our next example brings up an issue that lies at the heart of the issues considered in this thesis.

We consider the problems of evaluating the limit

$$\lim_{y \to 0^+} F_s(y) \tag{1.15}$$

as well as values of $F_s(y)$ for very small $y > 0$, where F_s is given by

$$F_s(y) = y^{-s} - \int_0^1 \frac{xy^s}{(y+x^2)^{\frac{3}{2}}} dx, \tag{1.16}$$

where the exponent s is determined by the requirement that the limit (1.15) must be finite. In the present case all three problems, the evaluation of s, the limit, and the function values for small y can be solved easily through closed form integration; for the corresponding nonlinear eigenvalue problems considered in Section 3.1.3, in contrast, no exact integration can be performed, eigenfunctions are involved, and nonlinear equations must be solved—so that the simple closed-form manipulations presented in what follows need to be substituted by a sequence of numerical procedures. With a view to the analysis in Section 3.1.3, below we show that, even in the context of the simple example under consideration, use of numerical quadrature rule would not give rise to accurate determination of the exponent s, the limit (1.15) or values of $F_s(y)$ for small values of y.

Remark 1.3.2. *In the context of our integral equation problem on surfaces containing conical singularities, the need to evaluate integral quantities "very small values" of a parameter y arises from the graded meshes used near the conical points: some of the sampling points we use can be as close to the conical point as 10^{-8} or even 10^{-10} times the size of the surface diameter.*

We thus proceed with our highly idealized example: integrating with respect to x we obtain

$$F_s(y) = y^{-s} - y^{s-\frac{1}{2}} + y^s(y+1)^{-\frac{1}{2}} \tag{1.17}$$

from which it is a simple matter to check that the condition

$$-s = s - \frac{1}{2},$$

or $s = \frac{1}{4}$, is necessary and sufficient for the limit (1.15) to be finite.

Having determined the exponent $s = \frac{1}{4}$ we now seek to evaluate $F_s(y)$ for small values of y. Certainly, in the present case we can use equation (1.17) to perform an analytical evaluation. As discussed above, in the cases considered in this thesis the integrals cannot be computed analytically; for illustrative purposes we thus undertake the task of evaluating

$F_s(y)$ without recourse to the closed form expression of the integral

$$\int_0^1 \frac{xy^{\frac{1}{4}}}{(y+x^2)^{\frac{3}{2}}}dx. \tag{1.18}$$

The integral (1.18) tends to ∞ as $y \to 0+$, and, thus, a numerical evaluation of this quantity by means of a standard quadrature rule would produce inaccurate results. Further, the subtraction of two nearly infinite quantities as in equation (1.16) would give rise to significant cancellation errors, and, thus, additional accuracy loss.

An alternative approach we use can be demonstrated in the present example: taking into account the fact that

$$y^{-\frac{1}{4}} = \int_0^\infty \frac{xy^{\frac{1}{4}}}{(y+x^2)^{\frac{3}{2}}}dx,$$

and that, as a result,

$$y^{-\frac{1}{4}} - \int_0^1 \frac{xy^{\frac{1}{4}}}{(y+x^2)^{\frac{3}{2}}}dx = \int_1^\infty \frac{xy^{\frac{1}{4}}}{(y+x^2)^{\frac{3}{2}}}dx, \tag{1.19}$$

we can evaluate $F_{1/4}(y)$ for small y by means of an expansion of the integrand:

$$\frac{xy^{\frac{1}{4}}}{(y+x^2)^{\frac{3}{2}}} = \frac{y^{\frac{1}{4}}}{x^2}\cdot\frac{1}{(1+\frac{y}{x^2})^{\frac{3}{2}}} = \frac{y^{\frac{1}{4}}}{x^2}\cdot(1 - \frac{1}{1!}\frac{3}{2}(\frac{y}{x^2}) + \frac{1}{2!}\frac{3}{2}\frac{5}{2}(\frac{y}{x^2})^2 - \cdots). \tag{1.20}$$

In all we obtain

$$F_{1/4}(y) = \int_1^\infty \frac{xy^{\frac{1}{4}}}{(y+x^2)^{\frac{3}{2}}}dx = y^{\frac{1}{4}} - \frac{1}{1!}\frac{3}{2}\frac{y^{1+\frac{1}{4}}}{3} + \frac{1}{2!}\frac{3}{2}\frac{5}{2}\frac{y^{2+\frac{1}{4}}}{5} - \cdots \tag{1.21}$$

The right hand side series in equation (1.21) converges very fast for the small values of y we consider. Thus, instead of approximating an integral whose value is close to ∞, and then subtracting two nearly infinite quantities, the procedure described above evaluates the quantity (1.16) by means of the series (1.21), with high accuracy and at very low computational cost.

1.4 Outline of chapters

This thesis is organized as follows.

In Chapter 2 we describe our parametrization of the boundary surface ∂D. In order to discretize our integral equations with a high order of accuracy, we first make the integrand smooth and periodic on a parameter space by partitioning the integration problem by means of certain smooth and periodic functions.

In Chapter 3, we present novel methods to compute singular pairs $(a_i(\theta_{\boldsymbol{x}}), q_i)$, which are determined by the left hand side of the integral equation, and, thus, by the geometry of the conical surface. With $(a_i(\theta_{\boldsymbol{x}}), q_i)$ computed, we develop methods to evaluate accurately the quantities

$$-\frac{a_i(\theta_{\boldsymbol{x}})}{2r_{\boldsymbol{x}}^{q_i}} + \int_{\partial D} \frac{\partial G(\boldsymbol{x}, \boldsymbol{x}')}{\partial n_{\boldsymbol{x}}} \cdot \frac{a_i(\theta')}{r_{\boldsymbol{x}'}^{q_i}} dS(\boldsymbol{x}'). \tag{1.22}$$

This is a challenging issue since, as discussed in Section 1.3.2, as the target point $\boldsymbol{x}$ approaches the conical point the overall integrand becomes more and more singular, in such a way that, regularizations similar to that considered in Section 1.3.1 do not suffice to produce acceptable accuracies. (As noted in Section 1.3.1, use of changes of variables give rise to useful regularization of infinite integrands, as long as the integrands admit a finite integral, of course. In the present case the integrals are finite, but tend to infinity as $\boldsymbol{x}$ approaches the conical point—so that a change-of-variable regularization scheme becomes less and less useful, and ultimately completely losses all accuracy as $\boldsymbol{x}$ approaches the conical point.) Using ideas demonstrated in Section 1.3.2, a methodology to address these difficulties is presented in Section 3.2.

In Chapter 4, we describe our discretization scheme for the integrals on surface ∂D through isolation of the integral kernel singularity, and application of the trapezoidal rule to every part of the integral. We shall see the discretization indeed exhibits high order of accuracy in any cases.

In Chapter 5, the discretization schemes introduced in previous chapters are used to produce a full discrete formulation for the boundary integral equation (1.7) using c_i and $b(\boldsymbol{x})$ as unknowns (see equation (1.12)). In this formulation, we utilize the singular pairs $(a_i(\theta_{\boldsymbol{x}}), q_i)$ computed previously, and the unknown $b(\boldsymbol{x})$ is determined for all points on a mesh on the surface ∂D.

In Chapter 6, we present a variety of test cases that demonstrate the properties of the algorithms developed in previous chapters. In particular we study the convergence of our

method as discretization meshes are refined, and we show that the overall methodology can produce both (singular) bounded and unbounded unknowns with a high degree of accuracy.

In Chapter 7, we give a summary of the work we perform and possible future improvements and extensions.

Chapter 2

Boundary Parameterization and the Fixed Partition of Unity

We seek to solve numerically the boundary integral equation (1.7) on the surface ∂D. In this thesis, the surface ∂D is assumed to be the boundary of a three dimensional body D with a conical point O; throughout this work we assume that in a neighborhood of the conical point O the surface ∂D coincides with the boundary of a straight cone defined by a given cross sectional curve, see Figure 2.12, and that, with exception of the conical singularity, ∂D is a smooth surface.

Our goal is to solve a discretized version of equation (1.7) by means of an iterative linear-algebra solver; the main difficulty to achieve this goal lies in producing an accurate algorithm for evaluation of the operator on the left hand side of equation (1.7), and the associated integral

$$\int_{\partial D} \frac{\partial G(\boldsymbol{x}, \boldsymbol{x}')}{\partial n_{\boldsymbol{x}}} \cdot \nu(\boldsymbol{x}') dS(\boldsymbol{x}'), \tag{2.1}$$

for given points $\boldsymbol{x} \in \partial D$. (As mentioned in Section 1.3.2, for $\boldsymbol{x}$ close to the conical point O the complete operator on the left hand side of equation (1.7) must be evaluated as a unit, and not as a difference of two large quantities.)

To evaluate these operators, we use an adequate representation of the boundary surface ∂D in terms of local charts together with a Partition of Unity, as indicated in Sections 2.1 and 2.2 below. Our algorithm for the actual evaluation of the integral (2.1) is discussed in Chapters 3 and 4. The iterative solution of the discretized operator and numerical examples demonstrating the performance of the overall solver are then presented in Chapters 5 and 6, respectively.

2.1 Overlapping patches $\mathcal{P}^k$

Since the surface ∂D generally cannot be represented by a single parametrization, in order to evaluate the integral in equation (2.1) we follow the approach [6], which is based on use of local coordinate parametrizations and Partitions of Unity (POU).

According to the POU method, we describe the boundary surface ∂D using several overlapping coordinates patches $\mathcal{P}^k, k = 1, \ldots, n$. In particular, to describe a surface with a conical point, such as that shown in Figure 2.1, we use two patches: one patch, which we call $\mathcal{P}^1$ and displayed in blue in Figure 2.2, contains the region near the conical point O; the second patch, which contains the complement of the first patch $\mathcal{P}^1$ and overlaps with $\mathcal{P}^1$, is called $\mathcal{P}^2$ and shown in red in Figure 2.3. Note the existence of a significant region of overlap between these two patches.

The coordinates patches $\mathcal{P}^k$, $(k = 1, 2)$ are assumed to satisfy the following conditions:

1. Each patch $\mathcal{P}^k$ is an open set within ∂D, and the union $\mathcal{P}^1 \cup \mathcal{P}^2$ covers all of ∂D.

2. Each patch $\mathcal{P}^k$ is the image of a coordinate open set $\mathcal{H}^k$, contained in a plane. The coordinate set $\mathcal{H}^k$ is mapped to patch $\mathcal{P}^k$ via a parametrization

$$\boldsymbol{x}^k = \boldsymbol{x}^k(u^k, v^k) \quad \text{defined for } (u^k, v^k) \in \mathcal{H}^k, k = 1, 2. \tag{2.2}$$

   A curve $\mathcal{O}^1 \in \mathcal{H}^1$ is mapped to the conical point O through the $k = 1$ parametrization defined in equation (2.2).

3. The parametrization in equation (2.2) is smoothly invertible, and the vector product

$$V^k(u^k, v^k) = \frac{\partial \boldsymbol{x}^k}{\partial u^k} \times \frac{\partial \boldsymbol{x}^k}{\partial v^k}$$

   is bounded away from zero in $(\mathcal{H}^1 \setminus \mathcal{O}^1) \cup \mathcal{H}^2$. We assume V^k is an outward normal, so that the outward unit normal on $\mathcal{P}^k$ is given by

$$n^k = \frac{V^k}{|V^k|}.$$

We use the open sets $\mathcal{H}^k$ and its coordinates (u^k, v^k) to evaluate the integral operator on the left hand side of equation (1.7). In Appendix A, we describe the explicit parametrization

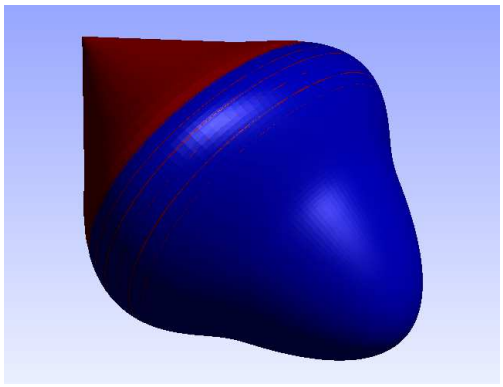

Figure 2.1: The surface ∂D with one conical point

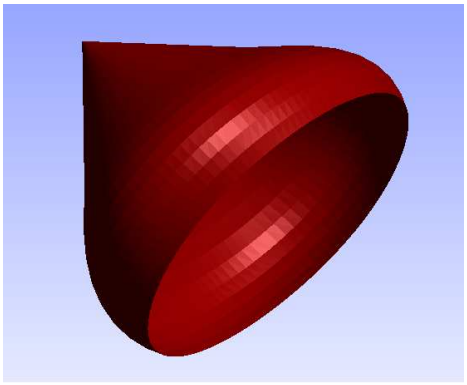

Figure 2.2: Patch $\mathcal{P}^1$ covers the area near the conical point

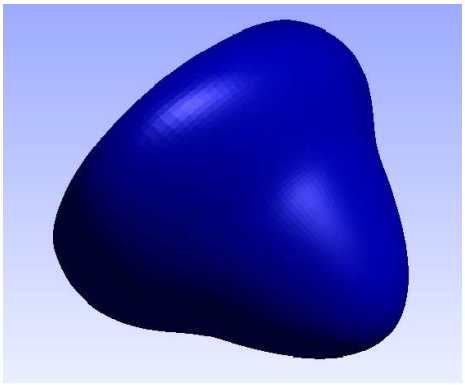

Figure 2.3: Patch $\mathcal{P}^2$ covers the area opposite to the conical point

and patches we use for the numerical examples in this thesis. The corresponding coordinate domains are $\mathcal{H}^k = [0,1] \times [0,1], (k = 1, 2)$.

2.2 Fixed POU function

According to the POU method, the overlapping patches $\mathcal{P}^k$ are used to decompose the integral on surface ∂D into the sum of two integrals over $\mathcal{P}^k$, $k = 1, 2$. To achieve this decomposition, we use a set of partition of unity functions $\{\omega^k(\boldsymbol{x}); k = 1, 2\}$ subordinated to these overlapping patches $\mathcal{P}^k$, $k = 1, 2$.

Specifically, we use the set of functions $\{\omega^k(\boldsymbol{x}); k = 1, 2\}$, such that

1. $\omega^k(\boldsymbol{x})$ is defined, smooth, and nonnegative on ∂D;

2. $\omega^k(\boldsymbol{x})$ vanishes outside $\mathcal{P}^k$;

3.
$$\sum_{k=1}^{2} \omega^k = 1 \quad \text{throughout } \partial D. \tag{2.3}$$

This pair of smooth functions will be referred to as the "fixed" partition of unity, in contrast with certain "floating" partitions of unity that are introduced in Chapter 4.

Using patch parametrizations $\boldsymbol{x}^k(u^k, v^k)$ and POU functions $\omega^k(\boldsymbol{x})$ as discussed above, the integral in equation (2.1) can be decomposed as

$$\begin{aligned}
&\int_{\partial D} \frac{\partial G(\boldsymbol{x}, \boldsymbol{x}')}{\partial n_{\boldsymbol{x}}} \nu(\boldsymbol{x}') dS(\boldsymbol{x}') \\
= &\sum_{k'=1}^{2} \int_{\mathcal{P}^{k'}} \frac{\partial G(\boldsymbol{x}, \boldsymbol{x}')}{\partial n_{\boldsymbol{x}}} \nu(\boldsymbol{x}') \omega^{k'}(\boldsymbol{x}') dS(\boldsymbol{x}') \\
= &\sum_{k'=1}^{2} \int_{\mathcal{H}^{k'}} \frac{\partial G(\boldsymbol{x}, \boldsymbol{x}^{k'}(u^{k'}_{\boldsymbol{x}'}, v^{k'}_{\boldsymbol{x}'}))}{\partial n_{\boldsymbol{x}}} \nu(\boldsymbol{x}^{k'}(u^{k'}_{\boldsymbol{x}'}, v^{k'}_{\boldsymbol{x}'})) \\
&\cdot J_{k'}(u^{k'}_{\boldsymbol{x}'}, v^{k'}_{\boldsymbol{x}'}) \omega^{k'}(\boldsymbol{x}^{k'}(u^{k'}_{\boldsymbol{x}'}, v^{k'}_{\boldsymbol{x}'})) du^{k'}_{\boldsymbol{x}'} dv^{k'}_{\boldsymbol{x}'}.
\end{aligned} \tag{2.4}$$

Here, $J_{k'}(u^{k'}_{\boldsymbol{x}'}, v^{k'}_{\boldsymbol{x}'})$ is the Jacobian of the parametrization $(u^{k'}_{\boldsymbol{x}'}, v^{k'}_{\boldsymbol{x}'})$ for the patch $\mathcal{P}^{k'}$.

Clearly, on the non-overlapping regions of a patch $\mathcal{P}^k$, ω^k must be equal to 1; further, the fixed POU function $\omega^k(\boldsymbol{x})$ should vanish smoothly towards the boundaries of the k-th patch. To construct such smoothly vanishing POU functions, we use as a building block

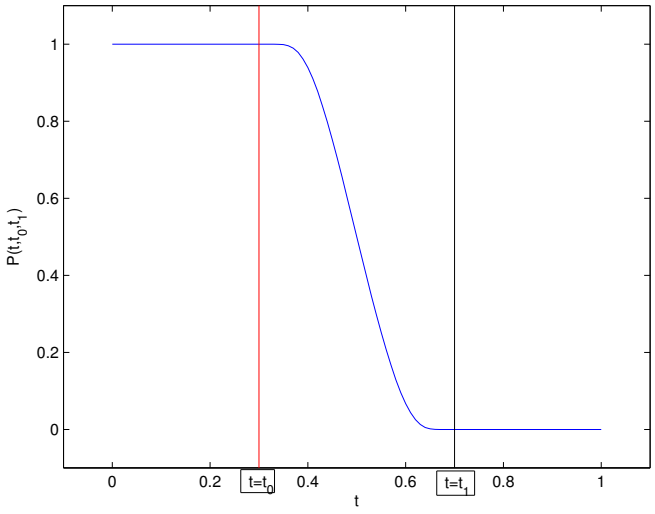

Figure 2.4: Auxiliary function $P(t, t_0, t_1)$

the function $P(t, t_0, t_1)$ depicted in Figure 2.4. The analytic form of function $P(t, t_0, t_1)$ is described in Appendix A. In particular we note from Figure 2.4 that $P(t < t_0, t_0, t_1) = 1; P(t > t_1, t_0, t_1) = 0$, and $P(t, t_0, t_1)$ decays smoothly from 1 to 0 as t goes from t_0 to t_1.

In Figures 2.5 and 2.6, we show, in color code, the values of the fixed POU function $\omega^1(\boldsymbol{x})$ on the patch $\mathcal{P}^1$ and the domain $\mathcal{H}^1$, respectively; the values $\omega^1(\boldsymbol{x}^1(u^1, v^1))$ as a function of the coordinates (u^1, v^1) are shown in Figure 2.7. In Figures 2.8 and 2.9, in turn, we display the function $\omega^2(\boldsymbol{x}^2(u^2, v^2))$ as a function of the parameters (u^2, v^2). These figures show the fixed POU functions as well as the manner in which each one of the two dimensional coordinate domains $\mathcal{H}^k$ is mapped onto the patch $\mathcal{P}^k$ in three dimensional space. (The analytic forms of the fixed POU functions and the coordinates mappings $\boldsymbol{x}^k(u^k, v^k)$ are further discussed in Section 4.1 and described in Appendix A.)

The main feature of these fixed POU functions is that $\omega^k(\boldsymbol{x}) = 1$ in the center of the patches, and $\omega^k(\boldsymbol{x})$ smoothly decays to 0 towards the boundary of the patch $\mathcal{P}^k$, where the patches overlap. On patch $\mathcal{P}^1$, $\omega^1(\boldsymbol{x}) = 1$ for $\boldsymbol{x}$ near the conical point O, and smoothly decays to 0 as the distance to the conical point O increases. Clearly, the region $\{\boldsymbol{x}; \omega^1(\boldsymbol{x}) < 1\}$ on patch $\mathcal{P}^1$ must overlap with patch $\mathcal{P}^2$.

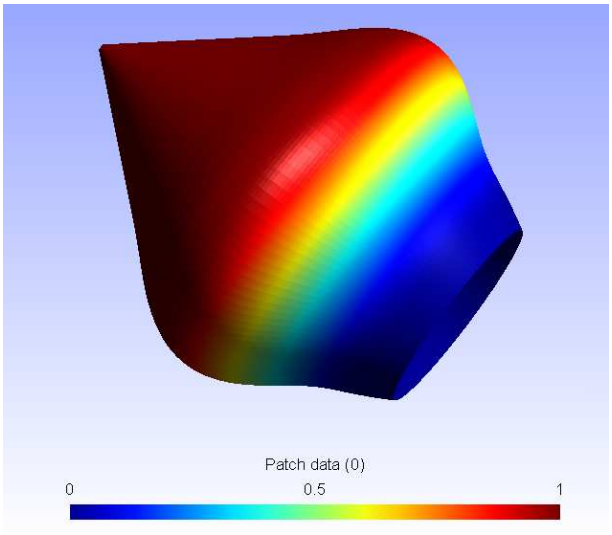

Figure 2.5: Values of the Fixed POU function $\omega^1(\boldsymbol{x})$ on its support set ($\subseteq \mathcal{P}^1$); in color code.

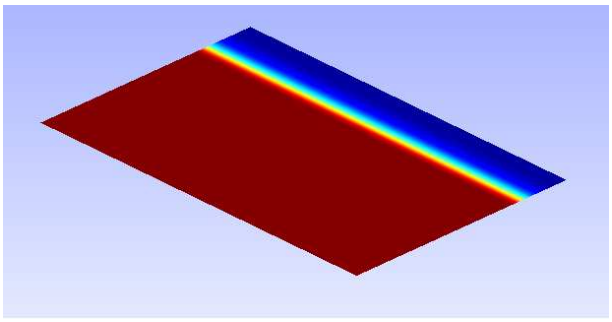

Figure 2.6: Values of the Fixed POU function $\omega^1(\boldsymbol{x^1}(u^1, v^1)$ on its domain $\mathcal{H}^1$; in color code.

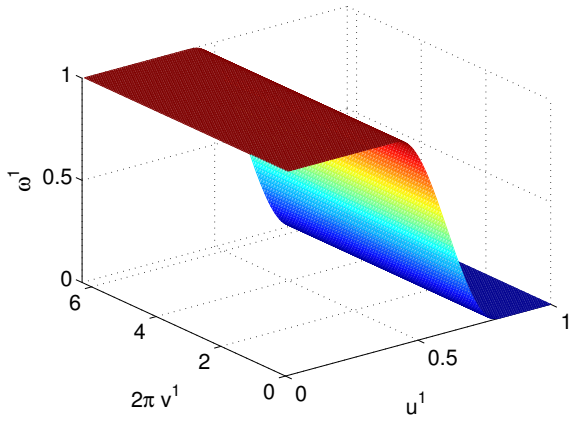

Figure 2.7: Graph of the Fixed POU function $\omega^1(\boldsymbol{x^1}(u^1, v^1))$ on its domain $\mathcal{H}^1$.

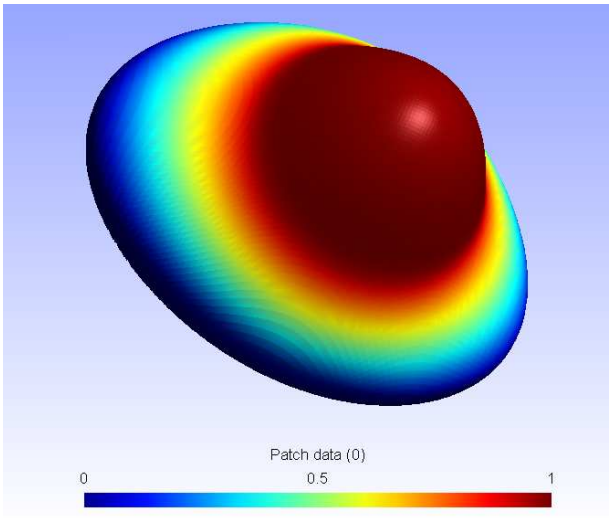

Figure 2.8: Color-coded values of the Fixed POU function $\omega^2(\boldsymbol{x})$ on its support set on patch $\mathcal{P}^2$

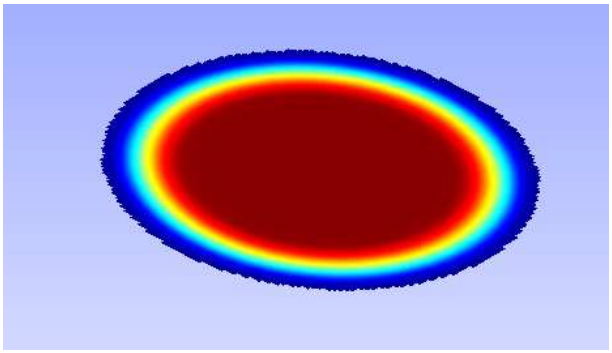

Figure 2.9: Color-coded values of the Fixed POU function $\omega^2(\boldsymbol{x}^2(u^2, v^2))$ on its support set in domain $\mathcal{H}^2$.

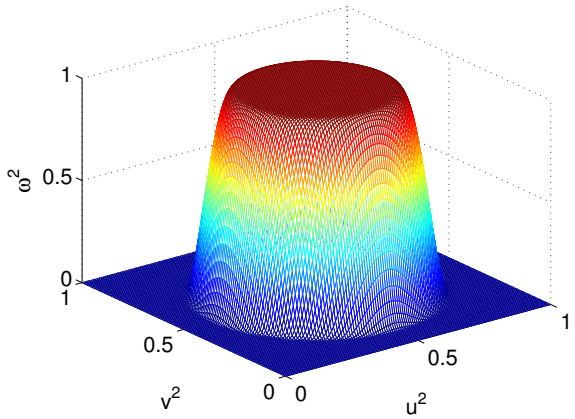

Figure 2.10: Graph of the Fixed POU function $\omega^2(\boldsymbol{x}^2(u^2, v^2))$ on its support set in domain $\mathcal{H}^2$.

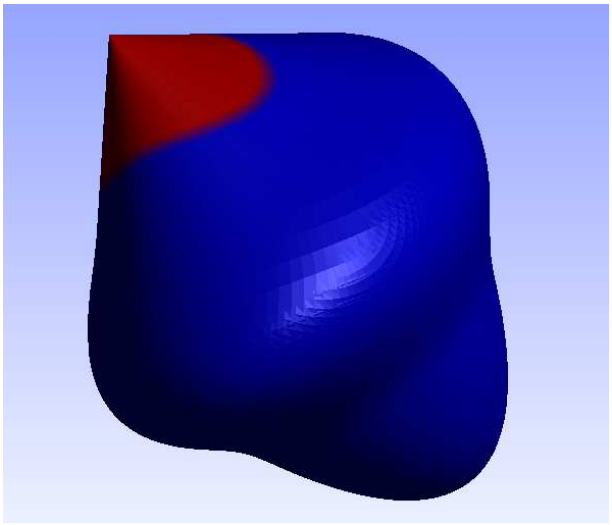

Figure 2.11: The straight-cone region S_σ (in red) near the conical point on the surface ∂D.

2.3 The parameterization for the region S_σ near the conical point

As mentioned above, in this thesis, we assume the surface ∂D coincides with the boundary of an infinite straight cone near the conical point O. More precisely, we assume there is a number $\sigma > 0$ such that the region S_σ of all points on ∂D whose distance to the conical point is less than or equal to σ which coincides with the boundary of a straight cone with a smooth cross section; see Figure 2.11 for a depiction in which S_σ is a portion of an elliptic cone. Note that the region S_σ is generally bounded by a non-planar curve: the boundary line lies on a plane only when S_σ is a section of a circular cone.

To represent points $\boldsymbol{x}$ in S_σ we use the spherical coordinates $(r_{\boldsymbol{x}}, \theta_{\boldsymbol{x}}, \phi_{\boldsymbol{x}})$ with azimuthal plane parallel to the $x-y$ plane and with origin at the conical point O:

$$\begin{cases} x_{\boldsymbol{x}} &= r_{\boldsymbol{x}} \sin\phi_{\boldsymbol{x}}(\theta_{\boldsymbol{x}}) \cos\theta_{\boldsymbol{x}} \\ y_{\boldsymbol{x}} &= r_{\boldsymbol{x}} \sin\phi_{\boldsymbol{x}}(\theta_{\boldsymbol{x}}) \sin\theta_{\boldsymbol{x}} \\ z_{\boldsymbol{x}} &= r_{\boldsymbol{x}} \cos\phi_{\boldsymbol{x}}(\theta_{\boldsymbol{x}}); \end{cases} \tag{2.5}$$

Figure 2.5 displays a point $\boldsymbol{x}$ on a straight cone surface with spherical coordinates $(r_{\boldsymbol{x}}, \theta_{\boldsymbol{x}}, \phi_{\boldsymbol{x}})$. We assume the description of the straight cone surface is given by a relation between the polar and azimuthal angles, $\phi_{\boldsymbol{x}}$ and $\theta_{\boldsymbol{x}}$ respectively: the points on the straight cone surface

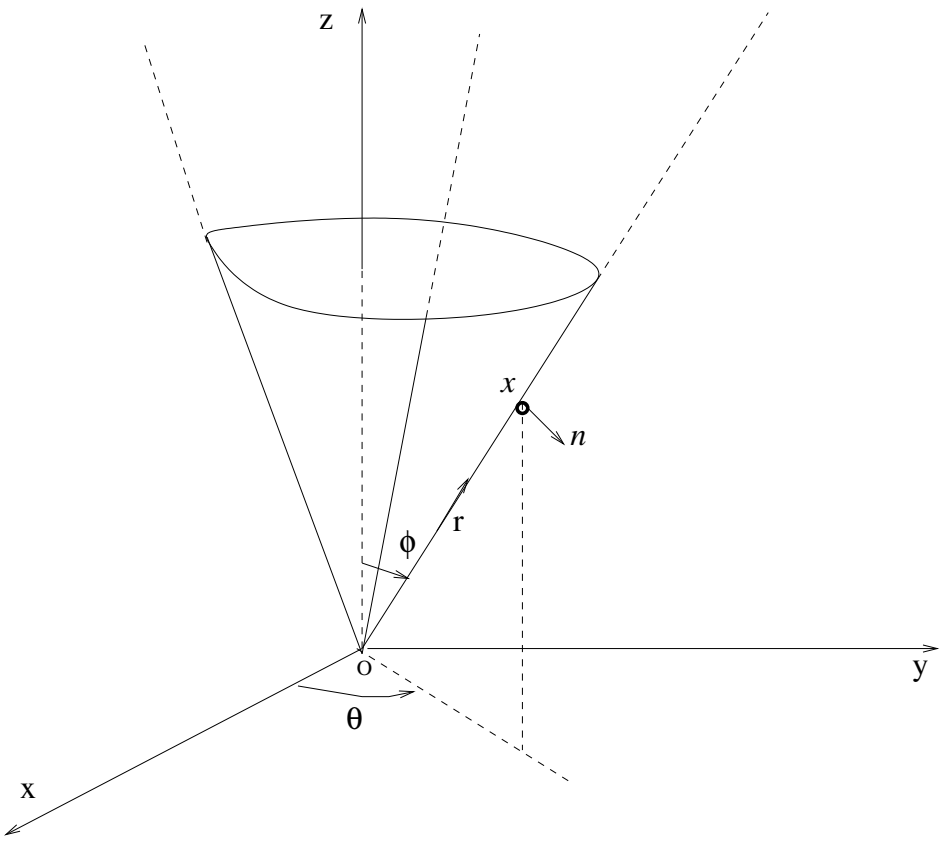

Figure 2.12: The parameters $r, \theta, \phi_{\boldsymbol{x}}$ near the conical point O.

are given by $(r_{\boldsymbol{x}}, \theta_{\boldsymbol{x}}, \phi_{\boldsymbol{x}}(\theta_{\boldsymbol{x}}))$:

$$S_\sigma = \{(r_{\boldsymbol{x}}, \theta_{\boldsymbol{x}}, \phi_{\boldsymbol{x}}(\theta_{\boldsymbol{x}})); 0 < r_{\boldsymbol{x}} < \sigma\},$$

for a certain smooth function $\phi_{\boldsymbol{x}}$. As an example, in Appendix A, we present the function $\phi_{\boldsymbol{x}}(\theta_{\boldsymbol{x}})$ for the surface of a straight elliptic cone.

Remark 2.3.1. *In this thesis we often use the notation* $\boldsymbol{x}(r_{\boldsymbol{x}}, \theta_{\boldsymbol{x}}, \phi_{\boldsymbol{x}}(\theta_{\boldsymbol{x}}))$ *for a point in the region* S_σ*. The coordinates* $(r_{\boldsymbol{x}}, \theta_{\boldsymbol{x}})$ *are most useful in our discussion of the computation of singular terms in Chapter 3.*

Remark 2.3.2. *Throughout this thesis we assume (as we may) that the parameter* σ *is small enough so that* S_σ *does not overlap with patch* $\mathcal{P}^2$*. Consequently, the fixed POU function* $\omega^1(\boldsymbol{x})$ *equals* 1 *for* $\boldsymbol{x} \in S_\sigma$*.*

Chapter 3

On Singular Exponents, Singular Coefficients and Their Evaluation

In Reference [32], it is shown that the density function $\nu(\boldsymbol{x})$ in equation (1.7) can be expressed in the form

$$\nu(\boldsymbol{x}) = \hat{\omega}_{\mathcal{P}^1}(\boldsymbol{x}) \sum_i \frac{c_i a_i(\theta_{\boldsymbol{x}})}{r_{\boldsymbol{x}}^{q_i}} + b(\boldsymbol{x}) \tag{3.1}$$

with

$$q_i > 0, \tag{3.2}$$

where $|b(\boldsymbol{x})| \lesssim r^p$ as $r \to 0$ for some $p > 0$. We call q_i the "singular exponent", a_i the "singular coefficient", and $(q_i, a_i(\theta_{\boldsymbol{x}}))$ the "singular pair". Here $r_{\boldsymbol{x}}$ and $\theta_{\boldsymbol{x}}$ are the spherical coordinates of the point $\boldsymbol{x}$ as described in Section 2.3, and, denoting by $(u_{\boldsymbol{x}}^1, v_{\boldsymbol{x}}^1)$ the coordinates of $\boldsymbol{x}$ in the domain $\mathcal{H}^1$ we have set

$$\hat{\omega}_{\mathcal{P}^1}(\boldsymbol{x}) = \begin{cases} 0 & \boldsymbol{x} \in \partial D \setminus \mathcal{P}^1 \\ \omega^1(u_{\boldsymbol{x}}^1, v_{\boldsymbol{x}}^1) & \boldsymbol{x} \in \mathcal{P}^1, \end{cases} \tag{3.3}$$

where $\omega^1(u_{\boldsymbol{x}}^1, v_{\boldsymbol{x}}^1)$ is the fixed POU function of patch $\mathcal{P}^1$. Note that, according to the definition of fixed POU functions in Section 2.2, the function $\hat{\omega}_{\mathcal{P}^1}(\boldsymbol{x})$ vanishes outside the patch $\mathcal{P}^1$.

Using the decomposition (3.1), the integral equation (1.7) becomes

$$\begin{aligned}
&-\frac{\nu(\boldsymbol{x})}{2}+\int_{\partial D}\frac{\partial G(\boldsymbol{x},\boldsymbol{x}')}{\partial n_{\boldsymbol{x}}}\cdot\nu(\boldsymbol{x}')dS(\boldsymbol{x}')\\
&=\sum_i\left(-\frac{1}{2}\frac{c_i a_i(\theta_{\boldsymbol{x}})}{r_{\boldsymbol{x}}^{q_i}}\hat{\omega}_{\mathcal{P}^1}(\boldsymbol{x})+\int_{\mathcal{P}^1}\frac{\partial G(\boldsymbol{x},\boldsymbol{x}')}{\partial n_{\boldsymbol{x}}}\frac{c_i a_i(\theta_{\boldsymbol{x}'})}{r_{\boldsymbol{x}'}^{q_i}}\hat{\omega}_{\mathcal{P}^1}(\boldsymbol{x}')dS(\boldsymbol{x}')\right)\\
&\quad+\left(-\frac{b(\boldsymbol{x})}{2}+\int_{\partial D}\frac{\partial G(\boldsymbol{x},\boldsymbol{x}')}{\partial n_{\boldsymbol{x}}}\cdot b(\boldsymbol{x}')dS(\boldsymbol{x}')\right)\\
&=g(\boldsymbol{x}).
\end{aligned}\tag{3.4}$$

In equation (3.4), the integrand $\frac{c_i a_i(\theta_{\boldsymbol{x}})}{r_{\boldsymbol{x}}^{q_i}}\hat{\omega}_{\mathcal{P}^1}(\boldsymbol{x})$ is only integrated on patch $\mathcal{P}^1$ since the windowing function $\hat{\omega}_{\mathcal{P}^1}(\boldsymbol{x})$ vanishes outside $\mathcal{P}^1$.

The rest of this Chapter is organized as follows: In Section 3.1, we describe a numerical method for the evaluation of singular exponents q_i and coefficients $a_i(\theta_{\boldsymbol{x}})$ for a given straight cone boundary surface of arbitrary cross section. As we will see, the determination of the singular pair $(q_i, a_i(\theta_{\boldsymbol{x}}))$ is independent of the explicit form of the right hand side $g(x)$ in the integral equation (3.4).

In Section 3.2, in turn, we describe a method for the evaluation of

$$-\frac{1}{2}\frac{a_i(\theta_{\boldsymbol{x}})}{r_{\boldsymbol{x}}^{q_i}}\hat{\omega}_{\mathcal{P}^1}(\boldsymbol{x})+\int_{S_\sigma}\frac{\partial G(\boldsymbol{x},\boldsymbol{x}')}{\partial n_{\boldsymbol{x}}}\frac{a_i(\theta_{\boldsymbol{x}'})}{r_{\boldsymbol{x}'}^{q_i}}\hat{\omega}_{\mathcal{P}^1}(\boldsymbol{x}')dS(\boldsymbol{x}')\tag{3.5}$$

in cases for which $\boldsymbol{x}$ is either close to or coincides with the conical point O. (Note that the integration domain in equation (3.5) is region S_σ, which is contained in but is different from patch $\mathcal{P}^1$.) In Chapter 4, we describe a method for numerical evaluation of the integral in the complementary region $\mathcal{P}^1 \setminus S_\sigma$.

Both our method for evaluation of singular pairs presented in Section 3.1 and the procedure described in Section 3.2 to evaluate the sum in equation 3.5 are essential elements of our overall algorithm. The former element allows us to isolate the most singular terms in our integral equation formulation. The latter element, on the other hand, which is closely related to the simplified example presented in Section 1.3.2, provides a means to produce bounded quantities that result as differences of quantities that tend to ∞ as $\boldsymbol{x}$ tends to the conical point O.

3.1 Computation of the singular pair $(q_i, a_i(\theta_{\boldsymbol{x}}))$

The evaluation of singular pairs proceeds through a reduction to the case of an infinite straight cone, as shown in the following three subsections.

3.1.1 Preliminary calculations

The right hand side of the integral equation (3.4) is a given function $g(\boldsymbol{x})$ which in this thesis is assumed to be bounded and continuous: this function coincides with the boundary condition in equation (1.3). The left hand side of the integral equation (3.4), on the other hand, may be expressed as the sum of a quantity involving singular terms

$$\sum_i \left(-\frac{c_i a_i(\theta_{\boldsymbol{x}})}{2 r_{\boldsymbol{x}}^{q_i}} \hat{\omega}_{\mathcal{P}^1}(\boldsymbol{x}) + \int_{\mathcal{P}^1} \frac{\partial G(\boldsymbol{x}, \boldsymbol{x}')}{\partial n_{\boldsymbol{x}}} \cdot \frac{c_i a_i(\theta_{\boldsymbol{x}'})}{r_{\boldsymbol{x}'}^{q_i}} \hat{\omega}_{\mathcal{P}^1}(\boldsymbol{x}') dS(\boldsymbol{x}') \right) \tag{3.6}$$

and a quantity involving (more) regular terms

$$-\frac{b(\boldsymbol{x})}{2} + \int_{\partial D} \frac{\partial G(\boldsymbol{x}, \boldsymbol{x}')}{\partial n_{\boldsymbol{x}}} \cdot b(\boldsymbol{x}') dS(\boldsymbol{x}'). \tag{3.7}$$

As $\boldsymbol{x}$ tends to the conical point O, both terms in equation (3.7) have finite values. Therefore, in order for the left hand side in equation (3.4) to remain bounded as $\boldsymbol{x}$ tends to the conical point (as they should, since the right hand side $g(\boldsymbol{x})$ does), the singular pairs $(q_i, a_i(\theta_{\boldsymbol{x}}))$ should satisfy the following condition:

$$\lim_{\boldsymbol{x} \to O} \sum_i \left(-\frac{c_i a_i(\theta_{\boldsymbol{x}})}{2 r_{\boldsymbol{x}}^{q_i}} \hat{\omega}_{\mathcal{P}^1}(\boldsymbol{x}) + \int_{\mathcal{P}^1} \frac{\partial G(\boldsymbol{x}, \boldsymbol{x}')}{\partial n_{\boldsymbol{x}}} \cdot \frac{c_i a_i(\theta_{\boldsymbol{x}'})}{r_{\boldsymbol{x}'}^{q_i}} \hat{\omega}_{\mathcal{P}^1}(\boldsymbol{x}') dS(\boldsymbol{x}') \right) < \infty. \tag{3.8}$$

Considering the terms under the summation symbol in equation (3.6), we note that, since the coordinate $r_{\boldsymbol{x}}$ tends to 0 as the point $\boldsymbol{x}$ tends to the conical point O, we have

$$-\frac{1}{2} \frac{c_i a_i(\theta_{\boldsymbol{x}})}{r_{\boldsymbol{x}}^{q_i}} \hat{\omega}_{\mathcal{P}^1}(\boldsymbol{x}) \sim \frac{1}{r_{\boldsymbol{x}}^{q_i}} \to \infty \quad \text{as } \boldsymbol{x} \to O.$$

As shown in Section 3.1.4, we have the following asymptotic formula for the integral containing the singular integrand term,

$$\int_{\mathcal{P}^1} \frac{\partial G(\boldsymbol{x}, \boldsymbol{x}')}{\partial n_{\boldsymbol{x}}} \cdot \frac{c_i a_i(\theta_{\boldsymbol{x}'})}{r_{\boldsymbol{x}'}^{q_i}} \hat{\omega}_{\mathcal{P}^1}(\boldsymbol{x}') dS(\boldsymbol{x}') \sim \frac{1}{r_{\boldsymbol{x}}^{q_i}} \quad \text{as } \boldsymbol{x} \to O. \tag{3.9}$$

It follows that, assuming, as we may, that the exponents q_i are pairwise different,

$$\int_{\mathcal{P}^1} \frac{\partial G(\boldsymbol{x},\boldsymbol{x}')}{\partial n_{\boldsymbol{x}}} \cdot \frac{c_i a_i(\theta_{\boldsymbol{x}'})}{r_{\boldsymbol{x}'}^{q_i}} \hat{\omega}_{\mathcal{P}^1}(\boldsymbol{x}') dS(\boldsymbol{x}') \quad \text{and} \quad \frac{c_i a_i(\theta_{\boldsymbol{x}})}{r_{\boldsymbol{x}}^{q_i}} \hat{\omega}_{\mathcal{P}^1}(\boldsymbol{x})$$

are the only terms in equation (3.4) that tend to ∞ like $\frac{1}{r_{\boldsymbol{x}}^{q_i}}$ as $\boldsymbol{x}$ tends to O. Consequently, the condition in equation (3.8) becomes: for each i, singular pair $(q_i, a_i(\theta_{\boldsymbol{x}}))$ should satisfy the condition

$$\lim_{\boldsymbol{x}\to O} \left(-\frac{a_i(\theta_{\boldsymbol{x}})}{2r_{\boldsymbol{x}}^{q_i}} \hat{\omega}_{\mathcal{P}^1}(\boldsymbol{x}) + \int_{\mathcal{P}^1} \frac{\partial G(\boldsymbol{x},\boldsymbol{x}')}{\partial n_{\boldsymbol{x}}} \cdot \frac{a_i(\theta_{\boldsymbol{x}'})}{r_{\boldsymbol{x}'}^{q_i}} \hat{\omega}_{\mathcal{P}^1}(\boldsymbol{x}') dS(\boldsymbol{x}') \right) < \infty. \tag{3.10}$$

Notice the common factor c_i (cf. equation (3.8)) has been removed at this stage.

Re-expressing the boundary integral in equation (3.10) as a sum of two integrals, one over the region S_σ and the other one over its complement $\mathcal{P}^1 \setminus S_\sigma$, the condition (3.10) becomes

$$\lim_{\boldsymbol{x}\to O} \left(-\frac{a_i(\theta_{\boldsymbol{x}})}{2r_{\boldsymbol{x}}^{q_i}} + \int_{S_\sigma} \frac{\partial G(\boldsymbol{x},\boldsymbol{x}')}{\partial n_{\boldsymbol{x}}} \cdot \frac{a_i(\theta_{\boldsymbol{x}'})}{r_{\boldsymbol{x}'}^{q_i}} dS(\boldsymbol{x}') \right) < \infty \tag{3.11}$$

since, for $\boldsymbol{x} \in S_\sigma$, $\hat{\omega}_{\mathcal{P}^1}(\boldsymbol{x}) = 1$ and since the integral

$$\int_{\mathcal{P}^1 \setminus S_\sigma} \frac{\partial G(\boldsymbol{x},\boldsymbol{x}')}{\partial n_{\boldsymbol{x}}} \cdot \frac{a_i(\theta_{\boldsymbol{x}'})}{r_{\boldsymbol{x}'}^{q_i}} \hat{\omega}_{\mathcal{P}^1}(\boldsymbol{x}') dS(\boldsymbol{x}') \tag{3.12}$$

is a smooth function for $\boldsymbol{x} \in S_\sigma$.

In order to evaluate singular pairs $(q_i, a_i(\theta_{\boldsymbol{x}}))$ on the basis of the condition (3.11), we use the coordinates $(r_{\boldsymbol{x}}, \theta_{\boldsymbol{x}})$ described in Section 2.3 as integration variables; condition (3.11) then reads

$$\begin{aligned} \lim_{\boldsymbol{x}\to O} \Bigg(& -\frac{a_i(\theta_{\boldsymbol{x}})}{2r_{\boldsymbol{x}}^{q_i}} + \\ & \int_0^\sigma \int_0^{2\pi} \frac{\partial G(\boldsymbol{x},\boldsymbol{x}')}{\partial n_{\boldsymbol{x}}}(r_{\boldsymbol{x}}, r_{\boldsymbol{x}'}, \theta_{\boldsymbol{x}}, \theta_{\boldsymbol{x}'}) \cdot \frac{a_i(\theta_{\boldsymbol{x}'})}{r_{\boldsymbol{x}'}^{q_i}} J_{r,\theta}(r_{\boldsymbol{x}'}, \theta_{\boldsymbol{x}'}) d\theta_{\boldsymbol{x}'} dr_{\boldsymbol{x}'} \Bigg) < \infty \end{aligned} \tag{3.13}$$

where

$$J_{r,\theta}(r_{\boldsymbol{x}}, \theta_{\boldsymbol{x}}) = r_{\boldsymbol{x}} \sqrt{(\frac{d\phi_{\boldsymbol{x}}}{d\theta_{\boldsymbol{x}}})^2 + \sin^2 \phi_{\boldsymbol{x}}} \tag{3.14}$$

is the Jacobian of the transformation, and where for any two points $\boldsymbol{x}(r_{\boldsymbol{x}}, \theta_{\boldsymbol{x}})$ and $\boldsymbol{x}'(r_{\boldsymbol{x}'}, \theta_{\boldsymbol{x}'})$

in the region S_σ, the integration kernel is given by

$$\begin{aligned}&\frac{\partial G(\boldsymbol{x},\boldsymbol{x}')}{\partial n_{\boldsymbol{x}}}(r_{\boldsymbol{x}},r_{\boldsymbol{x}'},\theta_{\boldsymbol{x}},\theta_{\boldsymbol{x}'})\\ =&\frac{1}{4\pi}\frac{r_{\boldsymbol{x}'}[\cos\phi_{\boldsymbol{x}'}\sin^2\phi_{\boldsymbol{x}}-\sin\phi_{\boldsymbol{x}'}\sin(\theta_{\boldsymbol{x}}-\theta_{\boldsymbol{x}'})\frac{d\phi_{\boldsymbol{x}}}{d\theta_{\boldsymbol{x}}}-\sin\phi_{\boldsymbol{x}'}\sin\phi_{\boldsymbol{x}}\cos\phi_{\boldsymbol{x}}\cos(\theta_{\boldsymbol{x}}-\theta_{\boldsymbol{x}'})]}{[r_{\boldsymbol{x}}^2+r_{\boldsymbol{x}'}^2-2r_{\boldsymbol{x}}r_{\boldsymbol{x}'}(\cos\phi_{\boldsymbol{x}}\cos\phi_{\boldsymbol{x}'}+\sin\phi_{\boldsymbol{x}}\sin\phi_{\boldsymbol{x}'}\cos(\theta_{\boldsymbol{x}}-\theta_{\boldsymbol{x}'}))]^{\frac{3}{2}}}.\end{aligned} \tag{3.15}$$

3.1.2 Reduction to the infinite straight-cone case

To proceed with the evaluation of singular pairs, we re-express the $r_{\boldsymbol{x}'}$-integral in equation (3.13) in the form

$$\int_0^\sigma \cdot dr_{\boldsymbol{x}'} = (\int_0^\infty - \int_\sigma^\infty)\cdot dr_{\boldsymbol{x}'} \tag{3.16}$$

and we use the explicit forms (3.14) and (3.15) of the functions

$$\frac{\partial G(\boldsymbol{x},\boldsymbol{x}')}{\partial n_{\boldsymbol{x}}}(r_{\boldsymbol{x}},r_{\boldsymbol{x}'},\theta_{\boldsymbol{x}},\theta_{\boldsymbol{x}'}) \quad \text{and} \quad J_{r,\theta}(r_{\boldsymbol{x}},\theta_{\boldsymbol{x}})$$

for the integral between σ and ∞. Integrating first with respect to $\theta_{\boldsymbol{x}'}$ and then with respect to $r_{\boldsymbol{x}'}$ we obtain

$$\begin{aligned}&\int_\sigma^\infty\int_0^{2\pi}\frac{\partial G(\boldsymbol{x},\boldsymbol{x}')}{\partial n_{\boldsymbol{x}}}(r_{\boldsymbol{x}},r_{\boldsymbol{x}'},\theta_{\boldsymbol{x}},\theta_{\boldsymbol{x}'})\cdot\frac{c_i a_i(\theta_{\boldsymbol{x}'})}{r_{\boldsymbol{x}'}^{q_i}}J_{r,\theta}(r_{\boldsymbol{x}'},\theta_{\boldsymbol{x}'})d\theta_{\boldsymbol{x}'}dr_{\boldsymbol{x}'}\\ =&\int_0^{2\pi}\frac{\sqrt{(\frac{d\phi_{\boldsymbol{x}'}}{d\theta_{\boldsymbol{x}'}})^2+\sin^2\phi_{\boldsymbol{x}'}}}{\sqrt{(\frac{d\phi_{\boldsymbol{x}}}{d\theta_{\boldsymbol{x}}})^2+\sin^2\phi_{\boldsymbol{x}}}}c_i a_i(\theta_{\boldsymbol{x}'})\cdot\\ &(\cos\phi_{\boldsymbol{x}'}\sin^2\phi_{\boldsymbol{x}}-\sin\phi_{\boldsymbol{x}'}\sin(\theta_{\boldsymbol{x}}-\theta_{\boldsymbol{x}'})\frac{d\phi_{\boldsymbol{x}}}{d\theta_{\boldsymbol{x}}}-\sin\phi_{\boldsymbol{x}'}\sin\phi_{\boldsymbol{x}}\cos\phi_{\boldsymbol{x}}\cos(\theta_{\boldsymbol{x}}-\theta_{\boldsymbol{x}'}))\cdot\\ &\int_\sigma^\infty\frac{r_{\boldsymbol{x}'}^{2-q_i}}{[r_{\boldsymbol{x}}^2+r_{\boldsymbol{x}'}^2-2rr_{\boldsymbol{x}'}(\cos\phi_{\boldsymbol{x}}\cos\phi_{\boldsymbol{x}'}+\sin\phi_{\boldsymbol{x}}\sin\phi_{\boldsymbol{x}'}\cos(\theta_{\boldsymbol{x}}-\theta_{\boldsymbol{x}'}))]^{\frac{3}{2}}}dr_{\boldsymbol{x}'}d\theta_{\boldsymbol{x}'}.\end{aligned} \tag{3.17}$$

For the explicit integration w.r.t. $r_{\boldsymbol{x}'}$ in equation (3.17), we apply the change of variable

$x = \frac{r_{\boldsymbol{x}'}}{r_{\boldsymbol{x}}}$, and we obtain

$$\begin{aligned}
&\int_\sigma^\infty \frac{r_{\boldsymbol{x}'}^{2-q_i}}{[r_{\boldsymbol{x}}^2 + r_{\boldsymbol{x}'}^2 - 2rr_{\boldsymbol{x}'}(\cos\phi_{\boldsymbol{x}}\cos\phi_{\boldsymbol{x}'} + \sin\phi_{\boldsymbol{x}}\sin\phi_{\boldsymbol{x}'}\cos(\theta_{\boldsymbol{x}} - \theta_{\boldsymbol{x}'}))]^{\frac{3}{2}}} dr_{\boldsymbol{x}'} \\
=&\frac{1}{r_{\boldsymbol{x}}^{q_i}} \int_{\frac{\sigma}{r_{\boldsymbol{x}}}}^\infty \frac{x^{2-q_i}}{[x^2 + 1 - 2x(\cos\phi_{\boldsymbol{x}}\cos\phi_{\boldsymbol{x}'} + \sin\phi_{\boldsymbol{x}}\sin\phi_{\boldsymbol{x}'}\cos(\theta_{\boldsymbol{x}} - \theta_{\boldsymbol{x}'}))]^{\frac{3}{2}}} dx \\
=&\frac{1}{q \cdot \sigma^{q_i}} + \mathcal{O}(r_{\boldsymbol{x}}).
\end{aligned} \tag{3.18}$$

The last equality results from the large x Laurent expansion

$$\frac{1}{[x^2 + 1 - 2x(\cos\phi_{\boldsymbol{x}}\cos\phi_{\boldsymbol{x}'} + \sin\phi_{\boldsymbol{x}}\sin\phi_{\boldsymbol{x}'}\cos(\theta_{\boldsymbol{x}} - \theta_{\boldsymbol{x}'}))]^{\frac{3}{2}}} = \frac{1}{x^3}(1 + \mathcal{O}(\frac{1}{x})). \tag{3.19}$$

The expansion in equation (3.19) is applicable to equation (3.18) for $\boldsymbol{x}$ close to O, so that $r_{\boldsymbol{x}}$ is small and $\frac{\sigma}{r_{\boldsymbol{x}}}$ is large.

Equations (3.18) and (3.19) show that the absolute value of the integral with respect to $r_{\boldsymbol{x}'}$ in equation (3.17) is bounded by a finite constant that is independent of $\theta_{\boldsymbol{x}}$ and $\theta_{\boldsymbol{x}'}$ (recall that $\phi_{\boldsymbol{x}}$ and $\phi_{\boldsymbol{x}'}$ are functions of $\theta_{\boldsymbol{x}}$ and $\theta_{\boldsymbol{x}'}$, respectively, cf. equation (2.5)). Since all $\theta_{\boldsymbol{x}}$ and $\theta_{\boldsymbol{x}'}$ dependent terms are also finite in the integral in equation (3.17), the full integral in equation (3.17) is uniformly bounded as $\boldsymbol{x}$ tends to the conical point O:

$$\lim_{\boldsymbol{x}\to O} \int_\sigma^\infty \int_0^{2\pi} \frac{\partial G(\boldsymbol{x}, \boldsymbol{x}')}{\partial n_{\boldsymbol{x}}}(r_{\boldsymbol{x}}, r_{\boldsymbol{x}'}, \theta_{\boldsymbol{x}}, \theta_{\boldsymbol{x}'}) \cdot \frac{a_i(\theta_{\boldsymbol{x}'})}{r_{\boldsymbol{x}'}^{q_i}} J_{r,\theta}(r_{\boldsymbol{x}'}, \theta_{\boldsymbol{x}'}) d\theta_{\boldsymbol{x}'} dr_{\boldsymbol{x}'} < \infty. \tag{3.20}$$

Combining equations (3.13) and (3.20) we obtain

$$\begin{aligned}
\lim_{\boldsymbol{x}\to O} \Bigg(&-\frac{a_i(\theta_{\boldsymbol{x}})}{2r_{\boldsymbol{x}}^{q_i}} + \\
&\int_0^\infty \int_0^{2\pi} \frac{\partial G(\boldsymbol{x}, \boldsymbol{x}')}{\partial n_{\boldsymbol{x}}}(r_{\boldsymbol{x}}, r_{\boldsymbol{x}'}, \theta_{\boldsymbol{x}}, \theta_{\boldsymbol{x}'}) \cdot \frac{a_i(\theta_{\boldsymbol{x}'})}{r_{\boldsymbol{x}'}^{q_i}} J_{r,\theta}(r_{\boldsymbol{x}'}, \theta_{\boldsymbol{x}'}) d\theta_{\boldsymbol{x}'} dr_{\boldsymbol{x}'} \Bigg) < \infty,
\end{aligned} \tag{3.21}$$

or equivalently,

$$\begin{aligned}
\lim_{\boldsymbol{x}\to O} \frac{1}{r_{\boldsymbol{x}}^{q_i}} \Bigg(&-\frac{a_i(\theta_{\boldsymbol{x}})}{2} + \\
&\int_0^\infty \int_0^{2\pi} \frac{\partial G(\boldsymbol{x}, \boldsymbol{x}')}{\partial n_{\boldsymbol{x}}}(r_{\boldsymbol{x}}, r_{\boldsymbol{x}'}, \theta_{\boldsymbol{x}}, \theta_{\boldsymbol{x}'}) \cdot a_i(\theta_{\boldsymbol{x}'}) \frac{r_{\boldsymbol{x}}^{q_i}}{r_{\boldsymbol{x}'}^{q_i}} J_{r,\theta}(r_{\boldsymbol{x}'}, \theta_{\boldsymbol{x}'}) d\theta_{\boldsymbol{x}'} dr_{\boldsymbol{x}'} \Bigg) < \infty.
\end{aligned} \tag{3.22}$$

As shown in the following section, this condition determines the singular pair $(q_i, a_i(\theta))$.

3.1.3 Evaluation of the singular pair

The expression in equation (3.22) equals the product of $\frac{1}{r_{\boldsymbol{x}}^{q_i}}$ with the quantity

$$
\begin{aligned}
&-\frac{a_i(\theta_{\boldsymbol{x}})}{2}+\int_0^{\infty}\int_0^{2\pi}\frac{\partial G(\boldsymbol{x},\boldsymbol{x}')}{\partial n_{\boldsymbol{x}}}(r_{\boldsymbol{x}},r_{\boldsymbol{x}'},\theta_{\boldsymbol{x}},\theta_{\boldsymbol{x}'})\cdot a_i(\theta_{\boldsymbol{x}'})\frac{r_{\boldsymbol{x}}^{q_i}}{r_{\boldsymbol{x}'}^{q_i}}J_{r,\theta}(r_{\boldsymbol{x}'},\theta_{\boldsymbol{x}'})d\theta_{\boldsymbol{x}'}dr_{\boldsymbol{x}'}\\
&=\Bigg(-\frac{a_i(\theta_{\boldsymbol{x}})}{2}+\int_0^{2\pi}\int_0^{\infty}\frac{\sqrt{(\frac{d\phi_{\boldsymbol{x}'}}{d\theta_{\boldsymbol{x}'}})^2+\sin^2\phi_{\boldsymbol{x}'}}}{\sqrt{(\frac{d\phi_{\boldsymbol{x}}}{d\theta_{\boldsymbol{x}}})^2+\sin^2\phi_{\boldsymbol{x}}}}a_i(\theta_{\boldsymbol{x}'})\\
&\frac{x^{2-q_i}(\cos\phi_{\boldsymbol{x}'}\sin^2\phi_{\boldsymbol{x}}-\sin\phi_{\boldsymbol{x}'}\sin(\theta_{\boldsymbol{x}}-\theta_{\boldsymbol{x}'})\frac{d\phi_{\boldsymbol{x}}}{d\theta_{\boldsymbol{x}}}-\sin\phi_{\boldsymbol{x}'}\sin\phi_{\boldsymbol{x}}\cos\phi_{\boldsymbol{x}}\cos(\theta_{\boldsymbol{x}}-\theta_{\boldsymbol{x}'}))}{[x^2+1-2x(\cos\phi_{\boldsymbol{x}}\cos\phi_{\boldsymbol{x}'}+\sin\phi_{\boldsymbol{x}}\sin\phi_{\boldsymbol{x}'}\cos(\theta_{\boldsymbol{x}}-\theta_{\boldsymbol{x}'}))]^{\frac{3}{2}}}\\
&dxd\theta_{\boldsymbol{x}'})\,,
\end{aligned}
\tag{3.23}
$$

where, once again, we have used the explicit forms (3.14) and (3.15) and the change of variables $x=\frac{r_{\boldsymbol{x}}}{r_{\boldsymbol{x}'}}$. Clearly, the quantity in equation (3.23) is independent of $r_{\boldsymbol{x}}$. Thus, for its product with term $\frac{1}{r_{\boldsymbol{x}}^{q_i}}$ in equation (3.22) to remain finite in the limit as $\boldsymbol{x}\to O$ ($r_{\boldsymbol{x}}\to 0$), it is necessary that the expressions in equation (3.23) equal 0:

$$
-\frac{a_i(\theta_{\boldsymbol{x}})}{2}+\int_0^{\infty}\int_0^{2\pi}\frac{\partial G(\boldsymbol{x},\boldsymbol{x}')}{\partial n_{\boldsymbol{x}}}(r_{\boldsymbol{x}},r_{\boldsymbol{x}'},\theta_{\boldsymbol{x}},\theta_{\boldsymbol{x}'})\cdot a_i(\theta_{\boldsymbol{x}'})\frac{r_{\boldsymbol{x}}^{q_i}}{r_{\boldsymbol{x}'}^{q_i}}J_{r,\theta}(r_{\boldsymbol{x}'},\theta_{\boldsymbol{x}'})d\theta_{\boldsymbol{x}'}dr_{\boldsymbol{x}'}=0. \tag{3.24}
$$

Using the notation

$$
K_q(c)=\int_0^{\infty}\frac{x^{2-q}}{(x^2+1-2xc)^{\frac{3}{2}}}dx, \tag{3.25}
$$

this condition can be expressed as the following equation for the singular pairs $(q_i,a_i(\theta_{\boldsymbol{x}}))$:

$$
\begin{aligned}
&\Bigg(-\frac{a_i(\theta_{\boldsymbol{x}})}{2}+\\
&\int_0^{2\pi}\frac{\sqrt{(\frac{d\phi_{\boldsymbol{x}'}}{d\theta_{\boldsymbol{x}'}})^2+\sin^2\phi_{\boldsymbol{x}'}}}{\sqrt{(\frac{d\phi_{\boldsymbol{x}}}{d\theta_{\boldsymbol{x}}})^2+\sin^2\phi_{\boldsymbol{x}}}}a_i(\theta_{\boldsymbol{x}'})K_{q_i}(\cos\phi_{\boldsymbol{x}}\cos\phi_{\boldsymbol{x}'}+\sin\phi_{\boldsymbol{x}}\sin\phi_{\boldsymbol{x}'}\cos(\theta_{\boldsymbol{x}}-\theta_{\boldsymbol{x}'}))\\
&(\cos\phi_{\boldsymbol{x}'}\sin^2\phi_{\boldsymbol{x}}-\sin\phi_{\boldsymbol{x}'}\sin(\theta_{\boldsymbol{x}}-\theta_{\boldsymbol{x}'})\frac{d\phi_{\boldsymbol{x}}}{d\theta_{\boldsymbol{x}}}-\sin\phi_{\boldsymbol{x}'}\sin\phi_{\boldsymbol{x}}\cos\phi_{\boldsymbol{x}}\cos(\theta_{\boldsymbol{x}}-\theta_{\boldsymbol{x}'}))d\theta_{\boldsymbol{x}'}\Bigg)\\
&=0.
\end{aligned}
\tag{3.26}
$$

Remark 3.1.1. *The function $K_q(c)$ in equation (3.25) can be computed analytically and expressed in terms of special functions. This can be performed easily with a software such as*

Mathematica.

Equation (3.26) determines the singular pairs $(q_i, a_i(\theta_{\boldsymbol{x}}))$. The exponents q_i are those quantities for which equation (3.26) admits nonzero homogeneous solutions $a_i(\theta_{\boldsymbol{x}})$. In order to solve this "nonlinear eigenvalue problem" numerically we discretize equation (3.26) using the trapezoidal rule, and thus obtain the following finite dimensional homogeneous linear system for the approximation of each exponent q_i and discretization $\{a_i^j, j = 1, \ldots, N_{sp}\}$ of $a_i(\theta_{\boldsymbol{x}})$:

$$\begin{aligned}
&\frac{1}{2}a_i^j + \frac{1}{4\pi}\sum_{j'=1}^{N_{sp}} \Big(K_{q_i}(\cos\phi(\theta_j)\cos\phi(\theta_{j'}) + \sin\phi(\theta_j)\sin\phi(\theta_{j'})\cos(\theta_j - \theta_{j'}))\cdot \\
&\qquad [\cos\phi(\theta_{j'})\sin^2\phi(\theta_j) + \sin\phi(\theta_{j'})\sin(\theta_{j'} - \theta_j)\frac{d\phi}{d\theta}(\theta_j) \\
&\qquad\quad - \sin\phi(\theta_{j'})\sin\phi(\theta_j)\cos\phi(\theta_j)\cos(\theta_{j'} - \theta_j)]\cdot \\
&\qquad \frac{\sqrt{(\frac{d\phi}{d\theta_{\boldsymbol{x}'}}(\theta_{j'}))^2 + \sin^2\phi(\theta_{j'})}}{\sqrt{(\frac{d\phi}{d\theta}(\theta_j))^2 + \sin^2\phi(\theta_j)}} a_i^{j'}\Big) = 0 \qquad \text{for} j = 1 \ldots N_{sp}.
\end{aligned} \tag{3.27}$$

Here N_{sp} is the number of integration points we use to discretize equation (3.26), and a_i^j is the numerical approximation of the value $a_i(\theta_j)$. The numerical values of the quantities q_i are determined as those for which the matrix associated with equation (3.27) admits 0 as an eigenvalue, and the values $\{a_i^j\}$ are the corresponding eigenvectors.

Analytical forms for the singular pairs $(q_i, a_i(\theta_{\boldsymbol{x}}))$ of cones with circular cross sections are given in Reference [32]; using these analytical forms in Chapter 6 we demonstrate the accuracy of the approximations $(q_i, \{a_i^j, j = 1, \ldots, N_{sp}\})$ resulting from equation (3.27). Of course, the procedure described above is valid for conical points of arbitrary cross section.

Remark 3.1.2. *Using the quantities $\{a_i^j, j = 1, \ldots, N_{sp}\}$, we can use an interpolation algorithm to obtain approximations to the function $a_i(\theta_{\boldsymbol{x}})$ for arbitrary angles $\theta_{\boldsymbol{x}}$. (Note that given the periodic nature of function $a_i(\theta_{\boldsymbol{x}})$, a high order of accuracy for the interpolation can be achieved by means of Fourier series and FFTs). Thus an approximation to the singular term $\frac{a_i(\theta_{\boldsymbol{x}})}{r_{\boldsymbol{x}}^{q_i}}$ can be obtained for any given point $\boldsymbol{x} \in \partial D$.*

3.1.4 Asymptotic behavior of the integral in equation (3.9)

In Section 3.1.1 we used the asymptotic behavior (3.9) of the integral

$$\int_{\mathcal{P}^1} \frac{\partial G(\boldsymbol{x},\boldsymbol{x}')}{\partial n_{\boldsymbol{x}}} \cdot \frac{c_i a_i(\theta_{\boldsymbol{x}'})}{r_{\boldsymbol{x}'}^{q_i}} \hat{\omega}_{\mathcal{P}^1}(\boldsymbol{x}') dS(\boldsymbol{x}') \sim \frac{1}{r_{\boldsymbol{x}}^{q_i}} \quad \text{as } \boldsymbol{x} \to O;$$

here we provide a proof of this relation.

Considering the split $\mathcal{P}^1 = (\mathcal{P}^1 \setminus S_\sigma) \cup S_\sigma$ as in equations (3.11) and (3.12), focusing first on the integral on S_σ, and recalling equation (3.16), we obtain

$$\begin{aligned}
&\int_{S_\sigma} \frac{\partial G(\boldsymbol{x},\boldsymbol{x}')}{\partial n_{\boldsymbol{x}}} \cdot \frac{c_i a_i(\theta_{\boldsymbol{x}'})}{r_{\boldsymbol{x}'}^{q_i}} dS(\boldsymbol{x}') \\
=&\Big(\int_0^\infty - \int_\sigma^\infty\Big) \int_0^{2\pi} \frac{\partial G(\boldsymbol{x},\boldsymbol{x}')}{\partial n_{\boldsymbol{x}}}(r_{\boldsymbol{x}}, r_{\boldsymbol{x}'}, \theta_{\boldsymbol{x}}, \theta_{\boldsymbol{x}'}) \cdot \frac{c_i a_i(\theta_{\boldsymbol{x}'})}{r_{\boldsymbol{x}'}^{q_i}} J_{r,\theta}(r_{\boldsymbol{x}'}, \theta_{\boldsymbol{x}'}) d\theta_{\boldsymbol{x}'} dr_{\boldsymbol{x}'} \\
=&\frac{1}{r_{\boldsymbol{x}}^{q_i}} \int_0^\infty \int_0^{2\pi} \frac{\partial G(\boldsymbol{x},\boldsymbol{x}')}{\partial n_{\boldsymbol{x}}}(r_{\boldsymbol{x}}, r_{\boldsymbol{x}'}, \theta_{\boldsymbol{x}}, \theta_{\boldsymbol{x}'}) \cdot c_i a_i(\theta_{\boldsymbol{x}'}) \frac{r_{\boldsymbol{x}}^{q_i}}{r_{\boldsymbol{x}'}^{q_i}} J_{r,\theta}(r_{\boldsymbol{x}'}, \theta_{\boldsymbol{x}'}) d\theta_{\boldsymbol{x}'} dr_{\boldsymbol{x}'} \\
&- \int_\sigma^\infty \int_0^{2\pi} \frac{\partial G(\boldsymbol{x},\boldsymbol{x}')}{\partial n_{\boldsymbol{x}}}(r_{\boldsymbol{x}}, r_{\boldsymbol{x}'}, \theta_{\boldsymbol{x}}, \theta_{\boldsymbol{x}'}) \cdot \frac{c_i a_i(\theta_{\boldsymbol{x}'})}{r_{\boldsymbol{x}'}^{q_i}} J_{r,\theta}(r_{\boldsymbol{x}'}, \theta_{\boldsymbol{x}'}) d\theta_{\boldsymbol{x}'} dr_{\boldsymbol{x}'}.
\end{aligned} \tag{3.28}$$

Recalling equations (3.20) and (3.26), we note that

$$\int_\sigma^\infty \int_0^{2\pi} \frac{\partial G(\boldsymbol{x},\boldsymbol{x}')}{\partial n_{\boldsymbol{x}}}(r_{\boldsymbol{x}}, r_{\boldsymbol{x}'}, \theta_{\boldsymbol{x}}, \theta_{\boldsymbol{x}'}) \cdot \frac{c_i a_i(\theta_{\boldsymbol{x}'})}{r_{\boldsymbol{x}'}^{q_i}} J_{r,\theta}(r_{\boldsymbol{x}'}, \theta_{\boldsymbol{x}'}) d\theta_{\boldsymbol{x}'} dr_{\boldsymbol{x}'}$$

is uniformly bounded, and that

$$\frac{1}{r_{\boldsymbol{x}}^{q_i}} \int_0^\infty \int_0^{2\pi} \frac{\partial G(\boldsymbol{x},\boldsymbol{x}')}{\partial n_{\boldsymbol{x}}}(r_{\boldsymbol{x}}, r_{\boldsymbol{x}'}, \theta_{\boldsymbol{x}}, \theta_{\boldsymbol{x}'}) \cdot c_i a_i(\theta_{\boldsymbol{x}'}) \frac{r_{\boldsymbol{x}}^{q_i}}{r_{\boldsymbol{x}'}^{q_i}} J_{r,\theta}(r_{\boldsymbol{x}'}, \theta_{\boldsymbol{x}'}) d\theta_{\boldsymbol{x}'} dr_{\boldsymbol{x}'} = \frac{c_i a_i(\theta_{\boldsymbol{x}})}{2 r_{\boldsymbol{x}}^{q_i}}.$$

As a result we obtain

$$\begin{aligned}
&\int_{S_\sigma} \frac{\partial G(\boldsymbol{x},\boldsymbol{x}')}{\partial n_{\boldsymbol{x}}} \cdot \frac{c_i a_i(\theta_{\boldsymbol{x}'})}{r_{\boldsymbol{x}'}^{q_i}} dS(\boldsymbol{x}') \\
=&\frac{c_i a_i(\theta_{\boldsymbol{x}})}{2 r_{\boldsymbol{x}}^{q_i}} - \int_\sigma^\infty \int_0^{2\pi} \frac{\partial G(\boldsymbol{x},\boldsymbol{x}')}{\partial n_{\boldsymbol{x}}}(r_{\boldsymbol{x}}, r_{\boldsymbol{x}'}, \theta_{\boldsymbol{x}}, \theta_{\boldsymbol{x}'}) \cdot \frac{c_i a_i(\theta_{\boldsymbol{x}'})}{r_{\boldsymbol{x}'}^{q_i}} J_{r,\theta}(r_{\boldsymbol{x}'}, \theta_{\boldsymbol{x}'}) d\theta_{\boldsymbol{x}'} dr_{\boldsymbol{x}'} \\
\sim&\frac{c_i a_i(\theta_{\boldsymbol{x}})}{2 r_{\boldsymbol{x}}^{q_i}} \sim \frac{1}{r_{\boldsymbol{x}}^{q_i}} \quad \text{as } \boldsymbol{x} \to O.
\end{aligned} \tag{3.29}$$

Since the integral

$$\int_{\mathcal{P}^1\setminus S_\sigma} \frac{\partial G(\boldsymbol{x},\boldsymbol{x}')}{\partial n_{\boldsymbol{x}}} \cdot \frac{c_i a_i(\theta_{\boldsymbol{x}'})}{r_{\boldsymbol{x}'}^{q_i}} \hat{\omega}_{\mathcal{P}^1}(\boldsymbol{x}') dS(\boldsymbol{x}')$$

is a smooth function when $\boldsymbol{x} \in S_\sigma$, the relation used in equation (3.9), namely

$$\int_{\mathcal{P}^1} \frac{\partial G(\boldsymbol{x},\boldsymbol{x}')}{\partial n_{\boldsymbol{x}}} \cdot \frac{c_i a_i(\theta_{\boldsymbol{x}'})}{r_{\boldsymbol{x}'}^{q_i}} \hat{\omega}_{\mathcal{P}^1}(\boldsymbol{x}') dS(\boldsymbol{x}') \sim \frac{1}{r_{\boldsymbol{x}}^{q_i}} \quad \text{as } \boldsymbol{x} \to O, \tag{3.30}$$

follows directly.

3.2 Evaluation of $-\frac{a_i(\theta_{\boldsymbol{x}})}{2r_{\boldsymbol{x}}^{q_i}} + \int_{S_\sigma} \frac{\partial G(\boldsymbol{x},\boldsymbol{x}')}{\partial n_{\boldsymbol{x}}} \cdot \frac{a_i(\theta_{\boldsymbol{x}'})}{r_{\boldsymbol{x}'}^{q_i}} dS(\boldsymbol{x}')$ for $\boldsymbol{x}$ close to the conical point O

To complete our formulation for the integral equation (3.4), we need to provide approximate numerical methods for the evaluation of all the terms of the left hand side operator. In Section 3.1, we computed the singular pair $(q_i, a_i(\theta_{\boldsymbol{x}}))$, and we showed that the integral $\int_{S_\sigma} \frac{\partial G(\boldsymbol{x},\boldsymbol{x}')}{\partial n_{\boldsymbol{x}}} \cdot \frac{a_i(\theta_{\boldsymbol{x}'})}{r_{\boldsymbol{x}'}^{q_i}} dS(\boldsymbol{x}')$ tends to ∞ as $\boldsymbol{x}$ tends to the conical point O. Clearly, therefore, a straightforward quadrature rule would not evaluate this integral accurately, and, further the difference of the two associated infinite quantities, which should remain bounded, would give rise to significant cancellation errors and numerical instability.

Based on the fact that the sum

$$-\frac{a_i(\theta_{\boldsymbol{x}})}{2} + \int_{S_\sigma} \frac{\partial G(\boldsymbol{x},\boldsymbol{x}')}{\partial n_{\boldsymbol{x}}} \cdot \frac{a_i(\theta_{\boldsymbol{x}'})}{r_{\boldsymbol{x}'}^{q_i}} dS(\boldsymbol{x}') \tag{3.31}$$

remains bounded (a condition which we used to determine the singular pairs $(q_i, a_i(\theta_{\boldsymbol{x}}))$), in this section, we provide an indirect method for evaluation of this sum for $\boldsymbol{x}$ either close to or at the conical point O. In Chapter 4, in turn, we describe methods for evaluation of all the other terms on the left hand side of the integral equation (3.4), including the integral with the singular term integrands in region $\mathcal{P}^1 \setminus S_\sigma$,

$$\int_{\mathcal{P}^1\setminus S_\sigma} \frac{\partial G(\boldsymbol{x},\boldsymbol{x}')}{\partial n_{\boldsymbol{x}}} \cdot \frac{a_i(\theta_{\boldsymbol{x}'})}{r_{\boldsymbol{x}'}^{q_i}} \hat{\omega}_{\mathcal{P}^1}(\boldsymbol{x}') dS(\boldsymbol{x}'). \tag{3.32}$$

Remark 3.2.1. *The sum in equation* (3.31) *does not include the (constant) coefficient* c_i *of the singular term, which depends on the right hand side* $g(x)$ *of the integral equation* (3.4),

and is an unknown that needs to be solved for as part of the full discrete formulation. Note that, in particular, the evaluation procedure described in this section does not depend in any way on the right hand side $g(x)$.

To evaluate (3.31) we first express the surface integral in equation (3.31) in terms of the spherical coordinates $(r_{\boldsymbol{x}'}, \theta_{\boldsymbol{x}'})$:

$$-\frac{a_i(\theta_{\boldsymbol{x}})}{2r_{\boldsymbol{x}}^{q_i}} + \int_0^{\sigma}\int_0^{2\pi} \frac{\partial G(\boldsymbol{x},\boldsymbol{x}')}{\partial n_{\boldsymbol{x}}}(r_{\boldsymbol{x}}, r_{\boldsymbol{x}'}, \theta_{\boldsymbol{x}}, \theta_{\boldsymbol{x}'}) \cdot \frac{a_i(\theta_{\boldsymbol{x}'})}{r_{\boldsymbol{x}'}^{q_i}} J_{r,\theta}(r_{\boldsymbol{x}'}, \theta_{\boldsymbol{x}'}) d\theta_{\boldsymbol{x}'} dr_{\boldsymbol{x}'}. \tag{3.33}$$

Then we re-express the $r_{\boldsymbol{x}'}$-integral in the form

$$\int_0^{\sigma} \cdot dr_{\boldsymbol{x}'} = \int_0^{\infty} \cdot dr_{\boldsymbol{x}'} - \int_{\sigma}^{\infty} \cdot dr_{\boldsymbol{x}'},$$

so that equation (3.33) becomes

$$\begin{aligned}
&-\frac{a_i(\theta_{\boldsymbol{x}})}{2r_{\boldsymbol{x}}^{q_i}} + \int_0^{\sigma}\int_0^{2\pi} \frac{\partial G(\boldsymbol{x},\boldsymbol{x}')}{\partial n_{\boldsymbol{x}}}(r_{\boldsymbol{x}}, r_{\boldsymbol{x}'}, \theta_{\boldsymbol{x}}, \theta_{\boldsymbol{x}'}) \cdot \frac{a_i(\theta_{\boldsymbol{x}'})}{r_{\boldsymbol{x}'}^{q_i}} J_{r,\theta}(r_{\boldsymbol{x}'}, \theta_{\boldsymbol{x}'}) d\theta_{\boldsymbol{x}'} dr_{\boldsymbol{x}'} \\
&= -\frac{a_i(\theta_{\boldsymbol{x}})}{2r_{\boldsymbol{x}}^{q_i}} + \Big(\int_0^{\infty} - \int_{\sigma}^{\infty}\Big) \int_0^{2\pi} \frac{\partial G(\boldsymbol{x},\boldsymbol{x}')}{\partial n_{\boldsymbol{x}}}(r_{\boldsymbol{x}}, r_{\boldsymbol{x}'}, \theta_{\boldsymbol{x}}, \theta_{\boldsymbol{x}'}) \cdot \frac{a_i(\theta_{\boldsymbol{x}'})}{r_{\boldsymbol{x}'}^{q_i}} J_{r,\theta}(r_{\boldsymbol{x}'}, \theta_{\boldsymbol{x}'}) d\theta_{\boldsymbol{x}'} dr_{\boldsymbol{x}'}.
\end{aligned} \tag{3.34}$$

Taking into account equation (3.24) (which we used in Section 3.1 to compute the singular pairs) and the explicit forms (3.14) of the Jacobian $J_{r,\theta}(r_{\boldsymbol{x}}, \theta_{\boldsymbol{x}})$ and (3.15) of the integration kernel $\frac{\partial G(\boldsymbol{x},\boldsymbol{x}')}{\partial n_{\boldsymbol{x}}}(r_{\boldsymbol{x}}, r_{\boldsymbol{x}'}, \theta_{\boldsymbol{x}}, \theta_{\boldsymbol{x}'})$, equation (3.34) becomes

$$\begin{aligned}
&-\frac{a_i(\theta_{\boldsymbol{x}})}{2r_{\boldsymbol{x}}^{q_i}} + \int_0^{\sigma}\int_0^{2\pi} \frac{\partial G(\boldsymbol{x},\boldsymbol{x}')}{\partial n_{\boldsymbol{x}}}(r_{\boldsymbol{x}}, r_{\boldsymbol{x}'}, \theta_{\boldsymbol{x}}, \theta_{\boldsymbol{x}'}) \cdot \frac{a_i(\theta_{\boldsymbol{x}'})}{r_{\boldsymbol{x}'}^{q_i}} J_{r,\theta}(r_{\boldsymbol{x}'}, \theta_{\boldsymbol{x}'}) d\theta_{\boldsymbol{x}'} dr_{\boldsymbol{x}'} \\
&= \frac{1}{r_{\boldsymbol{x}}^{q_i}} \int_0^{2\pi} \Big(-\int_{\frac{\sigma}{r_{\boldsymbol{x}}}}^{\infty}\Big) \frac{\sqrt{(\frac{d\phi_{\boldsymbol{x}'}}{d\theta_{\boldsymbol{x}'}})^2 + \sin^2\phi_{\boldsymbol{x}'}}}{\sqrt{(\frac{d\phi_{\boldsymbol{x}}}{d\theta_{\boldsymbol{x}}})^2 + \sin^2\phi_{\boldsymbol{x}}}} a_i(\theta_{\boldsymbol{x}'}) \\
&\frac{x^{2-q_i}(\cos\phi_{\boldsymbol{x}'}\sin^2\phi_{\boldsymbol{x}} - \sin\phi_{\boldsymbol{x}'}\sin(\theta_{\boldsymbol{x}} - \theta_{\boldsymbol{x}'})\frac{d\phi_{\boldsymbol{x}}}{d\theta_{\boldsymbol{x}}} - \sin\phi_{\boldsymbol{x}'}\sin\phi_{\boldsymbol{x}}\cos\phi_{\boldsymbol{x}}\cos(\theta_{\boldsymbol{x}} - \theta_{\boldsymbol{x}'}))}{[x^2 + 1 - 2x[\cos\phi_{\boldsymbol{x}}\cos\phi_{\boldsymbol{x}'} + \sin\phi_{\boldsymbol{x}}\sin\phi_{\boldsymbol{x}'}\cos(\theta_{\boldsymbol{x}} - \theta_{\boldsymbol{x}'})]]^{\frac{3}{2}}} \\
&dx d\theta_{\boldsymbol{x}'},
\end{aligned} \tag{3.35}$$

where once again we used the change of variable $x = \frac{r_{\boldsymbol{x}'}}{r_{\boldsymbol{x}}}$.

In view of the smoothness and periodicity with respect to $\theta_{\boldsymbol{x}'}$ of the integrand in equa-

tion (3.35), our algorithms use the trapezoidal rule to produce highly accurate approximations of the corresponding $\theta_{\boldsymbol{x}'}$-integral. To obtain the x-integral in a half-line, in turn, we do not resort to classical quadrature rules but, instead, we use term-wise integration of the large-x Laurent series

$$\begin{aligned}&[x^2+1-2x(\cos\phi_{\boldsymbol{x}}\cos\phi_{\boldsymbol{x}'}+\sin\phi_{\boldsymbol{x}}\sin\phi_{\boldsymbol{x}'}\cos(\theta_{\boldsymbol{x}}-\theta_{\boldsymbol{x}'}))]^{-\frac{3}{2}}\\ &\qquad\qquad=\frac{1}{x^3}(1+\frac{T_1(\theta_{\boldsymbol{x}},\theta_{\boldsymbol{x}'})}{x}+\frac{T_2(\theta_{\boldsymbol{x}},\theta_{\boldsymbol{x}'})}{x^2}+\ldots+\mathcal{O}(\frac{1}{x^n}))\end{aligned} \tag{3.36}$$

mentioned in equation (3.19).

The expansion in equation (3.36) provides us with a numerical evaluation algorithm for the x-integral:

$$\begin{aligned}&\frac{1}{r_{\boldsymbol{x}}^{q_i}}\int_{\frac{\sigma}{r_{\boldsymbol{x}}}}^{\infty}\frac{x^{2-q_i}}{[x^2+1-2x[\cos\phi_{\boldsymbol{x}}\cos\phi_{\boldsymbol{x}'}+\sin\phi_{\boldsymbol{x}}\sin\phi_{\boldsymbol{x}'}\cos(\theta_{\boldsymbol{x}}-\theta_{\boldsymbol{x}'})]]^{\frac{3}{2}}}dx\\ \simeq\;&\frac{1}{q_i\cdot\sigma^{q_i}}-\frac{T_1(\theta_{\boldsymbol{x}},\theta_{\boldsymbol{x}'})}{(q_i+1)\cdot\sigma^{q_i}}\frac{r_{\boldsymbol{x}}}{\sigma}+\frac{T_2(\theta_{\boldsymbol{x}},\theta_{\boldsymbol{x}'})}{(q_i+1)(q_i+2)\cdot\sigma^{q_i}}\frac{r_{\boldsymbol{x}}^2}{\sigma^2}+\ldots\\ &+\frac{T_{N_E}(\theta_{\boldsymbol{x}},\theta_{\boldsymbol{x}'})}{(q_i+1)(q_i+2)\cdots(q_i+N_E)\cdot\sigma^{q_i}}(\frac{r_{\boldsymbol{x}}}{\sigma})^{N_E}.\end{aligned} \tag{3.37}$$

Here N_E is the number of terms we use in the Laurent expansion in equation (3.36); this expression is valid for values $\frac{r_{\boldsymbol{x}}}{\sigma}$ smaller than 1.

Collecting results we obtain a complete algorithm for the numerical evaluation of the sum in equation (3.31):

$$\begin{aligned}&-\frac{a_i(\theta_{\boldsymbol{x}})}{2r_{\boldsymbol{x}}^{q_i}}+\int_0^{\sigma}\int_0^{2\pi}\frac{\partial G(\boldsymbol{x},\boldsymbol{x}')}{\partial n_{\boldsymbol{x}}}(r_{\boldsymbol{x}},r_{\boldsymbol{x}'},\theta_{\boldsymbol{x}},\theta_{\boldsymbol{x}'})\cdot\frac{a_i(\theta_{\boldsymbol{x}'})}{r_{\boldsymbol{x}'}^{q_i}}J_{r,\theta}(r_{\boldsymbol{x}'},\theta_{\boldsymbol{x}'})d\theta_{\boldsymbol{x}'}dr_{\boldsymbol{x}'}\\ \simeq&\sum_{j'}\frac{\sqrt{(\frac{d\phi}{d\theta})^2(\theta_{j'})+\sin^2\phi(\theta_{j'})}}{\sqrt{(\frac{d\phi_{\boldsymbol{x}}}{d\theta_{\boldsymbol{x}}})^2+\sin^2\phi_{\boldsymbol{x}}}}a_i(\theta_{j'})\cdot\\ &(\cos\phi(\theta_{j'})\sin^2\phi_{\boldsymbol{x}}-\sin\phi(\theta_{j'})\sin(\theta_{\boldsymbol{x}}-\theta_{j'})\frac{d\phi_{\boldsymbol{x}}}{d\theta_{\boldsymbol{x}}}-\sin\phi(\theta_{j'})\sin\phi_{\boldsymbol{x}}\cos\phi_{\boldsymbol{x}}\cos(\theta_{\boldsymbol{x}}-\theta_{j'}))\cdot\\ &\left(\frac{1}{q_i\cdot\sigma^{q_i}}-\frac{T_1(\theta_{\boldsymbol{x}},\theta_{j'})}{(q_i+1)\cdot\sigma^{q_i}}\frac{r_{\boldsymbol{x}}}{\sigma}+\frac{T_2(\theta_{\boldsymbol{x}},\theta_{j'})}{(q_i+1)(q_i+2)\cdot\sigma^{q_i}}\frac{r_{\boldsymbol{x}}^2}{\sigma^2}+\cdots\right.\\ &\left.+\frac{T_{N_E}(\theta_{\boldsymbol{x}},\theta_{j'})}{(q_i+1)(q_i+2)\cdots(q_i+N_E)\cdot\sigma^{q_i}}(\frac{r_{\boldsymbol{x}}}{\sigma})^{N_E}\right)\Delta\theta'.\end{aligned} \tag{3.38}$$

Here, $\{\theta_{j'}\}$ are all the points on an equi-spaced mesh in the interval $[0, 2\pi)$, and $\Delta\theta'$ is the step size of this mesh.

Remark 3.2.2. *The accuracy of the algorithm embodied in equation* (3.38) *depends on several parameters: the number of points in the* $\{\theta_{j'}\}$ *discretization, the number* N_E *of terms in the Laurent expansion, and the value* $\frac{r_{\boldsymbol{x}}}{\sigma}$ *which, certainly, must be smaller than* 1*. In order to obtain a high order of accuracy from the algorithm in equation* (3.38)*, its use is restricted to the range* $r_{\boldsymbol{x}} \leq \frac{\sigma}{10}$ *(including* $r_{\boldsymbol{x}} = 0$*!), or equivalently, to the region* $\boldsymbol{x} \in S_{\frac{\sigma}{10}}$*: the set of all* $\boldsymbol{x}$ *in* ∂D *whose distance to the conical point* O *is less than or equal to* $\frac{\sigma}{10}$ *(see Section 2.3). For* $r_{\boldsymbol{x}} > \frac{\sigma}{10}$ *our algorithm evaluates the quantity* (3.31)*, together with other portions of our integral operator, by means of the quadrature rules described in the following chapter.*

Chapter 4

Discrete integral operator: trapezoidal rule, polar coordinates and graded meshes

In Chapter 3, we described our methods for the numerical evaluation of singular pairs $(q_i, a_i(\theta_{\boldsymbol{x}}))$, as well as the numerical evaluation of the sum in equation (3.5) for small values of $r_{\boldsymbol{x}}$. In order to obtain the full numerical solution for equation (3.4), we need methods for the discretization of all the terms on the left hand side of that equation. In this Chapter we describe the discretization scheme for the surface integral

$$\int_{\partial D} \frac{\partial G(\boldsymbol{x}, \boldsymbol{x}')}{\partial n_{\boldsymbol{x}}} \cdot b(\boldsymbol{x}') dS(\boldsymbol{x}'), \tag{4.1}$$

with any given target point $\boldsymbol{x}$ on the surface ∂D. Using the same scheme, we evaluate the integral

$$\int_{\mathcal{P}^1} \frac{\partial G(\boldsymbol{x}, \boldsymbol{x}')}{\partial n_{\boldsymbol{x}}} \frac{a_i(\theta_{\boldsymbol{x}'})}{r_{\boldsymbol{x}'}^{q_i}} \hat{\omega}_{\mathcal{P}^1}(\boldsymbol{x}') dS(\boldsymbol{x}') \tag{4.2}$$

when $\boldsymbol{x}$ is neither close to nor at the conical point O, and the integrals

$$\int_{\mathcal{P}^1 \setminus S_\sigma} \frac{\partial G(\boldsymbol{x}, \boldsymbol{x}')}{\partial n_{\boldsymbol{x}}} \frac{a_i(\theta_{\boldsymbol{x}'})}{r_{\boldsymbol{x}'}^{q_i}} \hat{\omega}_{\mathcal{P}^1}(\boldsymbol{x}') dS(\boldsymbol{x}') \tag{4.3}$$

for $r_{\boldsymbol{x}} > \frac{\sigma}{10}$ that, as mentioned in remark 3.2.2, is not evaluated by means of the Laurent-expansion based algorithm.

As a basis to all of our numerical methods in this Chapter, we recall the surface parametrization and fixed POU decomposition described in equation (2.4), which we use to evaluate the integral in equation (4.1). That is, we decompose and transform the integral on ∂D to

integrals in the following coordinate domains,

$$\begin{aligned}
&\int_{\partial D} \frac{\partial G(\boldsymbol{x},\boldsymbol{x}')}{\partial n_{\boldsymbol{x}}} b(\boldsymbol{x}')dS(\boldsymbol{x}') \\
= \;& \sum_{k'=1}^{2} \int_{\mathcal{H}^{k'}} \frac{\partial G(\boldsymbol{x},\boldsymbol{x}^{k'}(u^{k'}_{\boldsymbol{x}'},v^{k'}_{\boldsymbol{x}'}))}{\partial n_{\boldsymbol{x}}} b(\boldsymbol{x}^{k'}(u^{k'}_{\boldsymbol{x}'},v^{k'}_{\boldsymbol{x}'})) \\
& \cdot J_{k'}(u^{k'}_{\boldsymbol{x}'},v^{k'}_{\boldsymbol{x}'})\omega^{k'}(\boldsymbol{x}^{k'}(u^{k'}_{\boldsymbol{x}'},v^{k'}_{\boldsymbol{x}'}))du^{k'}_{\boldsymbol{x}'}dv^{k'}_{\boldsymbol{x}'},
\end{aligned} \tag{4.4}$$

and, our numerical scheme discretizes the integrand in the Cartesian coordinate domain $\mathcal{H}^{k'}$ and produces approximate values of the integral by means of a quadrature described in the following sections.

One of the issues we need to address to produce an integration algorithm exhibiting a high order of accuracy is the singular nature of the integration kernel in equations (4.1) and (4.2):

$$\frac{\partial G(\boldsymbol{x},\boldsymbol{x}')}{\partial n_{\boldsymbol{x}}} = \frac{(\boldsymbol{x}-\boldsymbol{x}')\cdot n_{\boldsymbol{x}}}{4\pi|\boldsymbol{x}-\boldsymbol{x}'|^3}. \tag{4.5}$$

The denominator of this kernel vanishes with a higher power of $|\boldsymbol{x}-\boldsymbol{x}'|$ than the numerator does, and the kernel is thus singular at $\boldsymbol{x}=\boldsymbol{x}'$.

In Sections 4.1 and 4.2 we present our integration scheme, which follows [6], for the surface integral in equation (4.1). We start our description in Section 4.1, where we consider the case in which $\boldsymbol{x}$ is far from the integration domain. In this section we also describe a change of variables in the domain $(u^1,v^1)\in\mathcal{H}^1$ to make the integrand more smoothly periodic, so that our discrete integration scheme produces high-order of accuracy. In Section 4.2, in turn, we describe a scheme to accurately discretize the integral in the region containing the kernel singularity point $\boldsymbol{x}'=\boldsymbol{x}$.

In Section 4.3, we consider the smoothness of the integrand in equation (4.1) in the case that target point $\boldsymbol{x}$ and $\boldsymbol{x}'$ are both close to the conical point, and we discuss the impact of smoothness and the use of graded meshes on accuracy. In Section 4.4, then, using the singular pair approximations $(q_i,\{a_i^j, j=1,\ldots,N_{sp}\})$ obtained in Section 3.2 and the discretization schemes discussed in Sections 4.1 and 4.2, we describe our numerical evaluation procedure for the integrals in equations (4.2) and (4.3), and we thus complete our discrete method for evaluation of the operator (3.4).

4.1 Smooth integrands and trapezoidal rule

Remark 4.1.1. *In what follows we use the letter k to denote the index of the patch containing the target point $\boldsymbol{x}$: the coordinates of a point $\boldsymbol{x}$ in domain $\mathcal{H}^k$ are denoted by $(u^k_{\boldsymbol{x}}, v^k_{\boldsymbol{x}})$. Thus, a target point in the discretization is given by $\boldsymbol{x} = \boldsymbol{x}^k(u^k_{\boldsymbol{x}}, v^k_{\boldsymbol{x}})$.*

Similarly, we use letter k' to denote the index of the patch containing the integration point $\boldsymbol{x}'$: the coordinates of a discretization point $\boldsymbol{x}' \in \mathcal{P}^{k'}$ are denoted by $(u^{k'}_{\boldsymbol{x}'}, v^{k'}_{\boldsymbol{x}'})$. Thus, $\boldsymbol{x}' = \boldsymbol{x}^{k'}(u^{k'}_{\boldsymbol{x}}, v^{k'}_{\boldsymbol{x}})$.

Starting in this section, we present our various integration schemes in order of increasing complexity. Thus, in this section we describe the discretization scheme for a portion of the integral in equation (4.1), namely, the integral over a patch that does not contain the target point $\boldsymbol{x}$ (that is $k \neq k'$); other cases are treated in subsequent sections. In the present case, the product of the kernel and the partition of unity function is smooth; in terms of the coordinate domains, in this section we consider evaluation of the integrals in (4.4) in domains $\mathcal{H}^{k'}$ for which $\boldsymbol{x} \notin \mathcal{P}^{k'}$.

As mentioned in remark 1.3.1, the trapezoidal rule exhibits a high (spectral) order of accuracy for integration of a smoothly periodic integrand over a Cartesian coordinate domain $\mathcal{H}^{k'}$. In the remainder of this section we introduce a change of variables that give rise to smooth and periodic integrands, and we set up the spectrally accurate trapezoidal rule for the case $\boldsymbol{x} \notin \mathcal{P}^{k'}$ under consideration.

$k' = 1$: Polynomial change of variables. We introduce coordinates for the patch $\mathcal{P}^1$ for which the integrand for $\mathcal{P}^1$-integral is smooth and periodic, in spite of the singularity of the function $b(\boldsymbol{x}')$ ($b(\boldsymbol{x}')$ is bounded but some of its low-order derivatives are not; see Figure 6.8). (The discussion of the coordinates (u^1, v^1) is qualitative. For the analytical forms of them, see Appendix A.)

In terms of the Cartesian coordinate $z_{\boldsymbol{x}}$ and the angular coordinate

$$v^1 = \frac{\theta_{\boldsymbol{x}}}{2\pi},$$

the parametrization (2.5) of a straight cone becomes

$$\begin{cases} x_{\boldsymbol{x}} &= z_{\boldsymbol{x}} F_x(2\pi v^1) C(z_{\boldsymbol{x}}) \\ y_{\boldsymbol{x}} &= z_{\boldsymbol{x}} F_y(2\pi v^1) C(z_{\boldsymbol{x}}) \\ z_{\boldsymbol{x}} &= z_{\boldsymbol{x}}, \end{cases} \tag{4.6}$$

where $F_x(2\pi v^1)$ and $F_y(2\pi v^1)$ are two functions of v^1, whose explicit forms depend on the shape of the cone surface. The function $C(z_{\boldsymbol{x}})$ describes the (possibly) non-vanishing curvature of the region $\mathcal{P}^1 \setminus S_\sigma$ in the $z_{\boldsymbol{x}}$ direction; in particular, $C(z_{\boldsymbol{x}}) = 1$ in the straight-cone region S_σ.

The Jacobian of the transformation (4.6) is

$$J_1(z_{\boldsymbol{x}}, v^1) = z_{\boldsymbol{x}} \cdot F(v^1),$$

for some function $F(v^1)$. Clearly, as $z_{\boldsymbol{x}} \to 0$, the Jacobian $J_1(z_{\boldsymbol{x}}, v^1) \sim z_{\boldsymbol{x}}$ vanishes to first-order on the boundary $z_{\boldsymbol{x}} = 0$. In order to increase the vanishing-degree of the Jacobian, and consequently the order of smooth periodicity of the integrands, we follow the idea described in Section 1.3 and we introduce a change of variables of polynomial type:

$$\frac{z_{\boldsymbol{x}}}{h} = (u^1)^{n(u^1)}, \tag{4.7}$$

where h is the height of the straight cone and $n(u^1)$ is defined by

$$n(u^1) = (n_u - 1) \cdot P(u^1, u_0^1, u_1^1) + 1. \tag{4.8}$$

Here $P(u^1, u_0^1, u_1^1)$ is the function described in equation (A.1) with the two parameters $u_0^1 < u_1^1$ chosen within $[0, 1]$. Note that the function $n(u^1)$ equals n_u for $u^1 < u_0^1$, it equals 1 for $u^1 > u_1^1$, and it transitions from n_u to 1 as u^1 varies between u_0^1 and u_1^1.

Remark 4.1.2. *In all of our numerical examples we have chosen parameters in such a way that $n(u^1) = n_u$ throughout the region S_σ.*

Using the coordinates arising from the change of variables (4.7), we can let the coordinate domain $\mathcal{H}^1$ equal to $(u^1, v^1) \in [0, 1] \times [0, 1]$. In these variables the Jacobian $J_1(u^1, v^1)$ vanishes with order $(u^1)^{2n_u - 1}$ as $u^1 \to 0$. Thus, a large positive value n_u makes the full integrand

vanish to high order on the boundary $u^1 = 0$. We set $u^1 = \frac{z_{\boldsymbol{x}}}{h}$ when $u^1 > u_1^1$ in order to map the equi-spaced mesh points in the domain $\mathcal{H}^1$ to most of the patch $\mathcal{P}^1$ in a relatively uniform fashion.

In the v^1 direction, in turn, the boundaries $v^1 = 0$ and $v^1 = 1$ correspond to the same line on the surface ∂D, and, therefore, the integrand (4.4) in the domain $\mathcal{H}^1$ is periodic in the v^1 direction as well. Thus, in terms of the independent variables (u_1, v_1) the integrand is smoothly periodic in the integration domain $\mathcal{H}^1$. However, since the integrand does not vanish on the boundaries $v^1 = 0$ and $v^1 = 1$, a careful treatment is necessary to preserve this periodicity in the polar-integration described in Section 4.2.

$k' = 2$**: Smooth patch.** For $k' = 2$, we choose coordinates (u^2, v^2) in such a manner (see Appendix A for their analytic forms) that all four boundaries $u^2 = 0, 1$ and $v^2 = 0, 1$ of the integration domain $\mathcal{H}^2 = [0, 1] \times [0, 1]$ are where the fixed POU function $\omega^2(\boldsymbol{x}(u^2, v^2))$ vanishes to high order in domain $\mathcal{H}^2$, as depicted in Figure 2.10. As a result, the full integrand also vanishes to high order towards these boundaries. This feature makes the integrand smoothly periodic in the domain $\mathcal{H}^2$.

Trapezoidal integration. Having parametrized our domains in such a way that (for the case $\boldsymbol{x} \notin \mathcal{P}^{k'}$ considered in this section) all integrands are smoothly periodic, we use the trapezoidal rule for the discrete integration of the integral in equation (4.1) on an equi-spaced mesh. Specifically, we use a Cartesian set of nodes $(u_m^{k'}, v_l^{k'})$ within each coordinate domain $\mathcal{H}^{k'}$ given by

$$(u_m^{k'}, v_l^{k'}) \in \{(m\Delta u^{k'}, l\Delta v^{k'}); \quad m = 1 \dots N_u^{k'}, \quad l = 1 \dots N_v^{k'}\}.$$

Here, $\Delta u^{k'}$ and $\Delta v^{k'}$ are the step sizes of the discretizations in $u^{k'}$ and $v^{k'}$ directions, and $N_u^{k'}$ and $N_v^{k'}$ are the total numbers of mesh points in $u^{k'}$ and $v^{k'}$ directions, respectively.

All the integrands in the domains $\mathcal{H}^{k'}$ in equation (4.4) can be evaluated analytically on any mesh point $(u_{m'}^{k'}, v_{l'}^{k'})$, except for the unknown regular part $b(\boldsymbol{x}'(u_{\boldsymbol{x}'}^{k'}, v_{\boldsymbol{x}'}^{k'}))$—for which we seek to obtain approximate values $b_{m',l'}^{k'}$ through solution of a finite-dimensional linear algebra problem.

The trapezoidal rule we use for the numerical evaluation of the integral using nodal values

$b^{k'}_{m',l'}$ can thus be described as follows: for a given target point $\boldsymbol{x}$ not within patch $\mathcal{P}^{k'}$,

$$\begin{aligned}
&\int_{\mathcal{H}^{k'}} \frac{\partial G(\boldsymbol{x}, \boldsymbol{x}^{k'}(u^{k'}_{\boldsymbol{x}'}, v^{k'}_{\boldsymbol{x}'}))}{\partial n_{\boldsymbol{x}}} b(\boldsymbol{x}^{k'}(u^{k'}_{\boldsymbol{x}'}, v^{k'}_{\boldsymbol{x}'})) J_k(u^{k'}_{\boldsymbol{x}'}, v^{k'}_{\boldsymbol{x}'}) \omega^k(\boldsymbol{x}^{k'}(u^{k'}_{\boldsymbol{x}'}, v^{k'}_{\boldsymbol{x}'})) du^{k'}_{\boldsymbol{x}'} dv^{k'}_{\boldsymbol{x}'} \\
\simeq \quad &\sum_{l'} \sum_{m'} \frac{\partial G(\boldsymbol{x}, \boldsymbol{x}^{k'}(u^{k'}_{m'}, v^{k'}_{l'}))}{\partial n_{\boldsymbol{x}}} b^{k'}_{m',l'} J_k(u^{k'}_{m'}, v^{k'}_{l'}) \omega^k(\boldsymbol{x}^{k'}(u^{k'}_{m'}, v^{k'}_{l'})) \Delta u^{k'} \Delta v^{k'}. \qquad (4.9)
\end{aligned}$$

4.2 Kernel singularity and polar coordinates

In this section, we describe a discretization scheme for the integral in equation (4.1) in the case that the target point $\boldsymbol{x}$ is within the integration patch $\mathcal{H}^{k'}$. In this case, the integration kernel $\frac{\partial G(\boldsymbol{x},\boldsymbol{x}')}{\partial n_{\boldsymbol{x}}}$ is singular at the point $\boldsymbol{x}' = \boldsymbol{x} \in \mathcal{P}^{k'}$—a difficulty that does not exist in the case discussed in Section 4.1.

Remark 4.2.1. *For the sake of simplicity, whenever the target and integration domains are clear from the context, the coordinates $(u^k_{\boldsymbol{x}}, v^k_{\boldsymbol{x}}) \in \mathcal{H}^k$ of a target point $\boldsymbol{x} = \boldsymbol{x}^k(u^k_{\boldsymbol{x}}, v^k_{\boldsymbol{x}}) \in \mathcal{P}^k$ will be denoted by (u, v). Analogously, the coordinates $(u^{k'}_{\boldsymbol{x}'}, v^{k'}_{\boldsymbol{x}'}) \in \mathcal{H}^{k'}$ of an integration point $\boldsymbol{x}' = \boldsymbol{x}^{k'}(u^{k'}_{\boldsymbol{x}'}, v^{k'}_{\boldsymbol{x}'}) \in \mathcal{P}^{k'}$ will be denoted by $(u', v') \in \mathcal{H}^{k'}$ instead of $(u^{k'}_{\boldsymbol{x}'}, v^{k'}_{\boldsymbol{x}'})$.*

4.2.1 Floating partition of unity

In order to reduce the region (and therefore the cost) required for resolution of the kernel singularity, we use an infinitely smooth, finitely supported, windowing function $\eta_{\boldsymbol{x}}(\boldsymbol{x}')$, with adequately small support, to split our integration problem as follows:

$$\int \ldots dS(\boldsymbol{x}') = \int \ldots (1 - \eta_{\boldsymbol{x}}(\boldsymbol{x}')) dS(\boldsymbol{x}') + \int \ldots \eta_{\boldsymbol{x}}(\boldsymbol{x}') dS(\boldsymbol{x}'). \qquad (4.10)$$

The function $\eta_{\boldsymbol{x}}(\boldsymbol{x}')$ is equal to 1 when $\boldsymbol{x}'$ and $\boldsymbol{x}$ are close on the surface ∂D, and smoothly decays to 0 as the distance between $\boldsymbol{x}'$ and $\boldsymbol{x}$ increases. In what follows, we describe the definition of $\eta_{\boldsymbol{x}}(\boldsymbol{x}')$ in the coordinate domains $\mathcal{H}^k$ in general cases, and the modified definition of $\eta_{\boldsymbol{x}}(\boldsymbol{x}')$ regarding the v^1 dimension in domain $\mathcal{H}^1$.

$\eta_{\boldsymbol{x}}(\boldsymbol{x}')$ in the domain $\mathcal{H}^2$. In the coordinate domain $\mathcal{H}^2$, $\eta_{\boldsymbol{x}}(\boldsymbol{x}')$ is defined as follows

$$\eta_{\boldsymbol{x}}(\boldsymbol{x}') \quad \begin{cases} \text{equals 1} & \text{for} \quad |(u,v)-(u',v')| < \gamma_0 \\ \text{smoothly decays from 1 to 0} & \text{for} \quad \gamma_0 \le |(u,v)-(u',v')| < \gamma_1 \\ \text{equals 0} & \text{for} \quad \gamma_1 \le |(u,v)-(u',v')|, \end{cases} \tag{4.11}$$

where $|\cdot|$ denotes the length of a vector in the two-dimensional space (u^k, v^k). The function $\eta_{\boldsymbol{x}}(\boldsymbol{x}')$ can be expressed simply in terms of the function $P(t, t_0, t_1)$ introduced in Section 2.2. Like the global partition of unity introduced in Chapter 2, the pair $(\eta_{\boldsymbol{x}}(\boldsymbol{x}'), 1-\eta_{\boldsymbol{x}}(\boldsymbol{x}'))$ is also a POU. One such POU needs to be constructed for each target point $\boldsymbol{x}$: the collection of all such partitions of unity is referred to as the "floating" POU. Figure 4.1 depicts the function $\eta_{\boldsymbol{x}}(\boldsymbol{x}')$ on the surface ∂D; Figures 4.2 and 4.3, in turn, depict $\eta_{\boldsymbol{x}}(\boldsymbol{x}')$ on the coordinate domain $\mathcal{H}^1$. For these figures, we used the values $\gamma_0 = 0.04$ and $\gamma_1 = 0.2$, which are used in all computations in this thesis.

We point out that function $\eta_{\boldsymbol{x}}(\boldsymbol{x}')$ is periodic in the domain $\mathcal{H}^k$, except when its support set reaches the boundary of $\mathcal{H}^k$. However, the integrands overall are still periodic as long as other parts of the integrand vanish on these boundaries. In $u^1_{\boldsymbol{x}'}$ dimension, the fixed POU function $\omega^1(\boldsymbol{x}^1(u^1_{\boldsymbol{x}'}, v^1_{\boldsymbol{x}'}))$ vanishes on the boundary line $u^1_{\boldsymbol{x}'} = 1$, and the Jacobian $J_1(u^1_{\boldsymbol{x}'}, v^1_{\boldsymbol{x}'})$ vanishes on the boundary line $u^1_{\boldsymbol{x}'} = 0$; while in domain $\mathcal{H}^2$, the POU function $\omega^2(\boldsymbol{x}^2(u^2_{\boldsymbol{x}'}, v^2_{\boldsymbol{x}'}))$ vanishes on all boundary lines $u^2_{\boldsymbol{x}'} = 0, 1$ and $v^2_{\boldsymbol{x}'} = 0, 1$. In all these cases, even if the boundary lines are within distance γ_1 to the point $(u^{k'}_{\boldsymbol{x}'}, v^{k'}_{\boldsymbol{x}'})$, the full integrand still vanishes on them, and is periodic.

$\eta_{\boldsymbol{x}}(\boldsymbol{x}')$ in the domain $\mathcal{H}^1$. For the domain $\mathcal{H}^1$ the definition of the floating POU function $\eta_{\boldsymbol{x}}(\boldsymbol{x}')$ needs to be modified slightly from the one given previously in equation (4.11). Indeed, the integrand

$$\frac{\partial G(\boldsymbol{x}(u^1_{\boldsymbol{x}}, v^1_{\boldsymbol{x}}), \boldsymbol{x}^1(u^1_{\boldsymbol{x}'}, v^1_{\boldsymbol{x}'}))}{\partial n_{\boldsymbol{x}}} b(\boldsymbol{x}^1(u^1_{\boldsymbol{x}'}, v^1_{\boldsymbol{x}'})) J_1(u^1_{\boldsymbol{x}'}, v^1_{\boldsymbol{x}'}) \omega^1(\boldsymbol{x}^1(u^1_{\boldsymbol{x}'}, v^1_{\boldsymbol{x}'})) \tag{4.12}$$

is periodic in the v^1 direction—since $v^1 = 0$ and $v^1 = 1$ correspond to the same line on ∂D. This periodicity, however, would not be inherited by the floating POU if we used the definition (4.11). Specifically, when the distance between the point $\boldsymbol{x}^1(u^1_{\boldsymbol{x}}, v^1_{\boldsymbol{x}})$ and the

boundary $v^1_{\boldsymbol{x}'} = 0$ is smaller than γ_1, the function $\eta_{\boldsymbol{x}}(\boldsymbol{x}^1(u^1_{\boldsymbol{x}'}, v^1_{\boldsymbol{x}'}))$ is not equal to 0 on the portion of the boundary line $v^1_{\boldsymbol{x}'} = 0$ with distance to the point $(u^1_{\boldsymbol{x}}, v^1_{\boldsymbol{x}})$ smaller than γ_1. On the boundary line $v^1_{\boldsymbol{x}'} = 1$, which on the other side of the domain, $\eta_{\boldsymbol{x}}(\boldsymbol{x}^1(u^1_{\boldsymbol{x}'}, v^1_{\boldsymbol{x}'}))$ is equal to 0 as long as γ_1 is chosen smaller than the distance between point $(u^1_{\boldsymbol{x}}, v^1_{\boldsymbol{x}})$ and line $v^1_{\boldsymbol{x}'} = 1$. Thus, the function $\eta_{\boldsymbol{x}}(\boldsymbol{x}^1(u^1_{\boldsymbol{x}'}, v^1_{\boldsymbol{x}'}))$ and in turn, the whole integrand in equation (4.12) is not periodic across the boundary lines $v^1_{\boldsymbol{x}'} = 0$ and $v^1_{\boldsymbol{x}'} = 1$. This issue also arises for the case in which the distance between point $(u^1_{\boldsymbol{x}}, v^1_{\boldsymbol{x}})$ and the boundary line $v^1_{\boldsymbol{x}'} = 1$ is smaller than γ_1.

In order to keep the integrand periodic after being multiplied by functions $\eta_{\boldsymbol{x}}(\boldsymbol{x}')$ and $1 - \eta_{\boldsymbol{x}}(\boldsymbol{x}')$, we need to modify the floating POU function $\eta_{\boldsymbol{x}}(\boldsymbol{x}')$ in domain $\mathcal{H}^1$. These floating POU functions should extend periodically across the boundary lines $v^1_{\boldsymbol{x}'} = 0$ and $v^1_{\boldsymbol{x}'} = 1$, and the support set of $\eta_{\boldsymbol{x}}(\boldsymbol{x}')$ should cross these two boundaries. In detail, when $v^1_{\boldsymbol{x}'} < \gamma_1$, as the distance between the point $(u^1_{\boldsymbol{x}}, v^1_{\boldsymbol{x}})$ and $v^1_{\boldsymbol{x}'} = 0$ is smaller than γ_1, the floating POU function should be given by

$$\eta^M_{\boldsymbol{x}}(\boldsymbol{x}') = \max(\eta_{\boldsymbol{x}}(\boldsymbol{x}'), \eta_{\boldsymbol{x}}(\boldsymbol{x}^1(u^1_{\boldsymbol{x}'}, v^1_{\boldsymbol{x}'} - 1)))$$

where, $\eta_{\boldsymbol{x}}(\boldsymbol{x}')$ is defined in (4.11) and $\boldsymbol{x}^1(u^1_{\boldsymbol{x}'}, v^1_{\boldsymbol{x}'}-1)$ is the point on patch $\mathcal{P}^1$ with coordinates $(u^1_{\boldsymbol{x}'}, v^1_{\boldsymbol{x}'}-1)$. This modified floating POU function $\eta^M_{\boldsymbol{x}}(\boldsymbol{x}')$ carves a disc-shaped region around $\boldsymbol{x}$ on the coordinates domain across the boundary lines $v^1_{\boldsymbol{x}'} = 0$ and $v^1_{\boldsymbol{x}'} = 1$—as displayed in Figure 4.4 on the surface ∂D, and displayed in Figures 4.5 and 4.6 on the coordinate domain $\mathcal{H}^1$. Since the modified floating POU function $\eta^M_{\boldsymbol{x}}(\boldsymbol{x}')$ is periodic in the coordinate domain, the full integrands of both parts of the integral in equation (4.10) are periodic.

The product of the function $(1-\eta_{\boldsymbol{x}}(\boldsymbol{x}'))$ and the integrand in equation (4.1) (which tends to infinity at $\boldsymbol{x}' = \boldsymbol{x}$, see Figure 4.7) is a smooth function of $\boldsymbol{x}'$. For this nonsingular and periodic integrand (displayed in Figure 4.8) the trapezoidal rule on an equi-spaced mesh $(u^{k'}_{m'}, v^{k'}_{l'})$ yields spectral accuracy; we thus have the highly accurate approximation

$$\begin{aligned}
&\int_{\mathcal{H}^{k'}} \frac{\partial G(\boldsymbol{x}, \boldsymbol{x}^{k'}(u^{k'}_{\boldsymbol{x}'}, v^{k'}_{\boldsymbol{x}'}))}{\partial n_{\boldsymbol{x}}} b(\boldsymbol{x}^{k'}(u^{k'}_{\boldsymbol{x}'}, v^{k'}_{\boldsymbol{x}'})) J_k(u^{k'}_{\boldsymbol{x}'}, v^{k'}_{\boldsymbol{x}'}) \omega^k(\boldsymbol{x}^{k'}(u^{k'}_{\boldsymbol{x}'}, v^{k'}_{\boldsymbol{x}'})) \cdot \\
&(1 - \eta_{\boldsymbol{x}}(\boldsymbol{x}^{k'}(u^{k'}_{\boldsymbol{x}'}, v^{k'}_{\boldsymbol{x}'}))) du^{k'}_{\boldsymbol{x}'} dv^{k'}_{\boldsymbol{x}'} \\
\simeq\ & \sum_{l'} \sum_{m'} \frac{\partial G(\boldsymbol{x}, \boldsymbol{x}^{k'}(u^{k'}_{m'}, v^{k'}_{l'}))}{\partial n_{\boldsymbol{x}}} b^{k'}_{m',l'} J_k(u^{k'}_{m'}, v^{k'}_{l'}) \omega^k(\boldsymbol{x}^{k'}(u^{k'}_{m'}, v^{k'}_{l'})) \\
&(1 - \eta_{\boldsymbol{x}}(\boldsymbol{x}^{k'}(u^{k'}_{m'}, v^{k'}_{l'}))) \Delta u^{k'} \Delta v^{k'}.
\end{aligned} \tag{4.13}$$

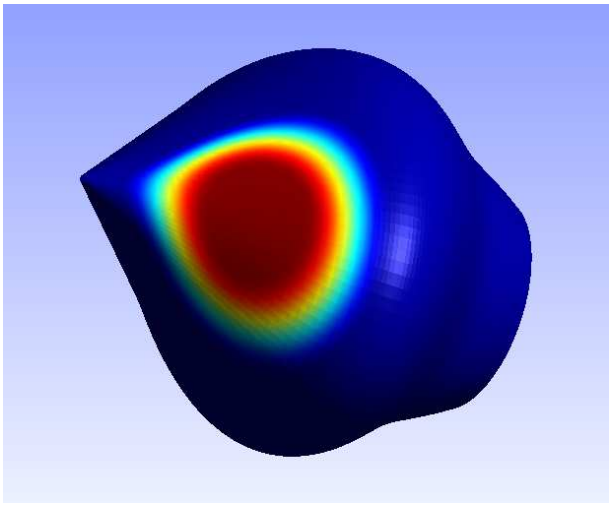

Figure 4.1: Support of a floating POU function not crossing the boundary $v^1 = 0$ (displayed on the patch $\mathcal{P}^1$).

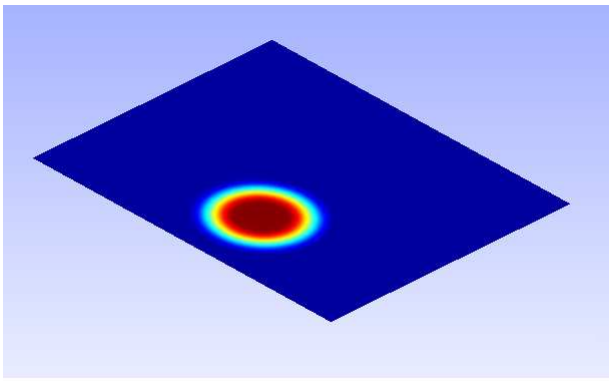

Figure 4.2: Support of a floating POU function not crossing the boundary $v^1 = 0$ (displayed in $\mathcal{H}^1$).

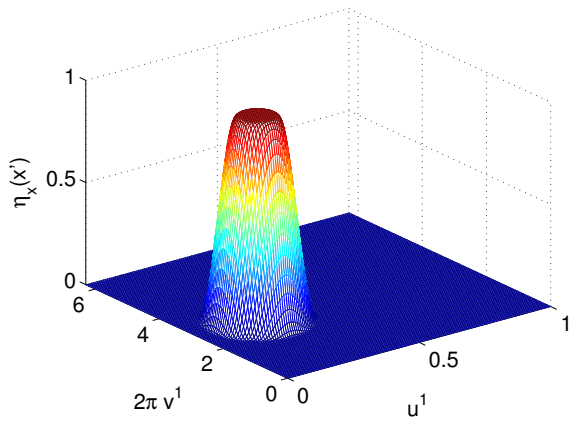

Figure 4.3: Graph of a floating POU function whose support does not cross the boundary $v^1 = 0$.

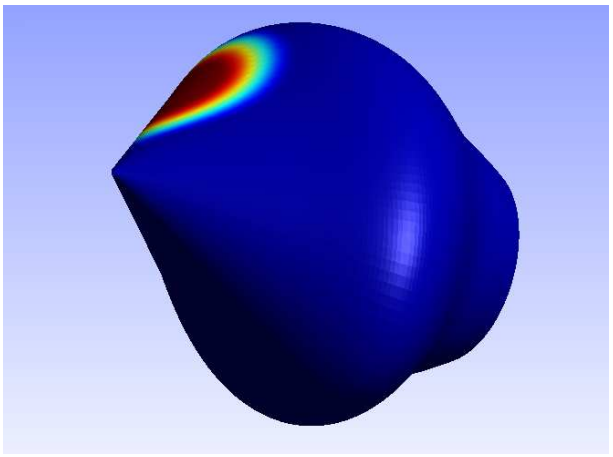

Figure 4.4: Support of a floating POU function crossing the boundary $v^1 = 0$ (displayed in $\mathcal{P}^1$).

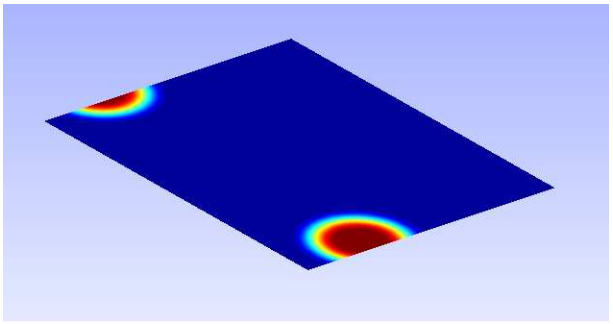

Figure 4.5: Support of a floating POU function crossing the boundary $v^1 = 0$ (displayed in $\mathcal{H}^1$).

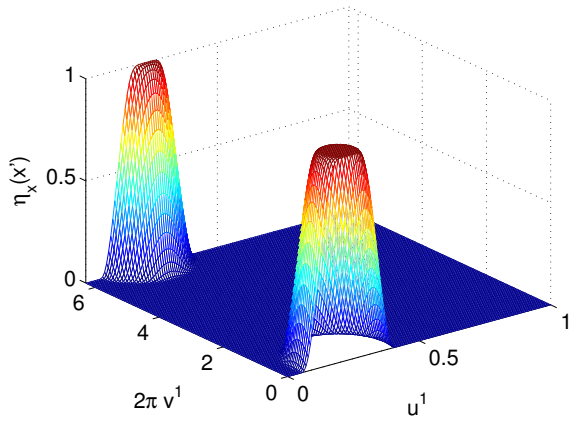

Figure 4.6: Graph of a floating POU function whose support crosses the boundary $v^1 = 0$.

The integral containing the factor $\eta_{\boldsymbol{x}}(\boldsymbol{x}')$, on the other hand, remains singular, but its support is confined to a small region in parameter space. As explained in what follows, to obtain these integrals with high-order accuracy we use, for each target point $\boldsymbol{x}$, a polar coordinate change of variables—a procedure which fully regularizes the kernel singularity. In detail, on each patch $\mathcal{H}^{k'}$, we need to integrate numerically the product of a smooth function

$$f_{k'}(u',v') = b(\boldsymbol{x}^{k'}(u',v'))J_{k'}(\boldsymbol{x}^{k'}(u',v'))\omega^{k'}(\boldsymbol{x}^{k'}(u',v'))\eta_{\boldsymbol{x}}(\boldsymbol{x}^{k'}(u',v'))$$

and the singular kernel

$$\frac{\partial G(\boldsymbol{x},\boldsymbol{x}^{k'}(u',v'))}{\partial n_{\boldsymbol{x}}} = \frac{\mathbf{R}\cdot n_{\boldsymbol{x}}}{|\mathbf{R}|^3}$$

where, for an arbitrary evaluation point $\boldsymbol{x}\in\partial D$, we have set $\mathbf{R} = \boldsymbol{x} - \boldsymbol{x}^{k'}(u',v')$.

Polar integration in domain $\mathcal{H}^2$. In domain $\mathcal{H}^2$, to resolve the singularity, which occurs at $(u',v') = (u,v) \in \mathcal{H}^2$, we use a system of polar coordinates centered at the coordinates (u,v) of the target point:

$$u' = u + \rho\cos\xi$$
$$v' = v + \rho\sin\xi.$$

In this system of coordinates the relevant integrals are given by

$$I(u,v) = \frac{1}{2}\int_0^{2\pi} L(u,v,\xi)d\xi, \quad \text{where} \tag{4.14}$$

$$L(u,v,\xi) = \int_{-\gamma_1}^{\gamma_1} f_2^*(\rho,\xi)\frac{|\rho|}{|\mathbf{R}|}\frac{\mathbf{R}\cdot n_{\boldsymbol{x}}}{|\mathbf{R}|^2}d\rho. \tag{4.15}$$

Here we have used the notations

$$\mathbf{R} = \mathbf{R}(\rho,\xi) = \boldsymbol{x}(u,v) - \boldsymbol{x}^*(\rho,\xi),$$
$$\boldsymbol{x}^*(\rho,\xi) = \boldsymbol{x}(u+\rho\cos\xi, v+\rho\sin\xi), \quad \text{and}$$
$$f_2^*(\rho,\xi) = f_2(u+\rho\cos\xi, v+\rho\sin\xi).$$

It is easy to check that the integrands in (4.14) and (4.15) are smooth functions of the

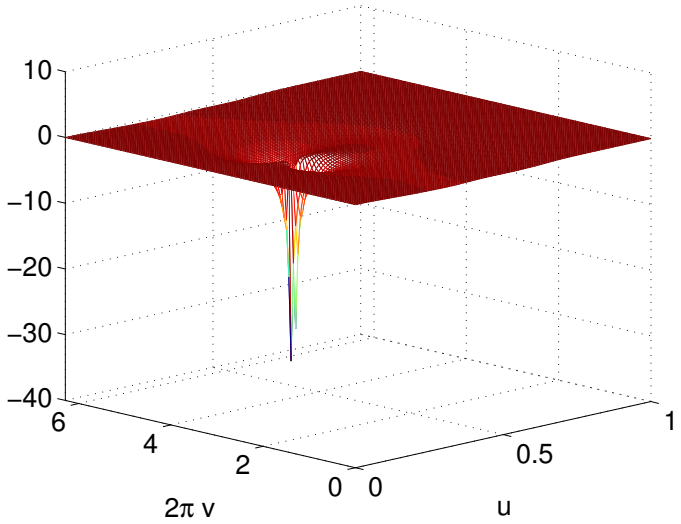

Figure 4.7: Integrand in which a density function of the form $\frac{1}{r^{0.28}}$ is assumed, and without using the floating POU factor.

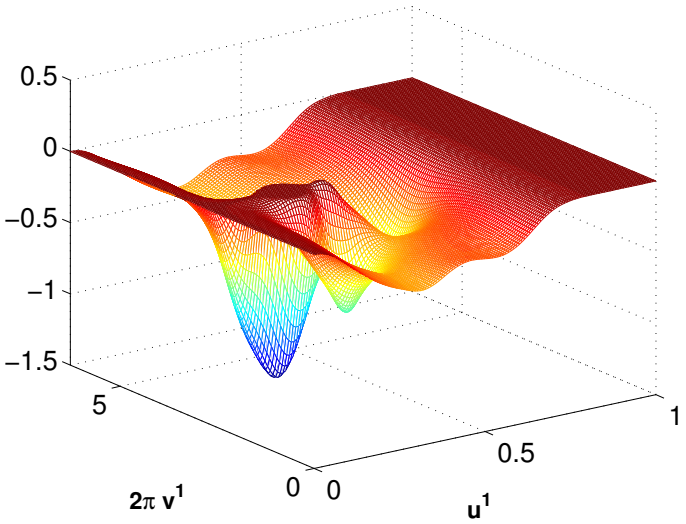

Figure 4.8: Integrand including a density function $\frac{1}{r^{0.28}}$ using the $1 - \eta_{\boldsymbol{x}}$ floating POU factor.

respective integration variables [6], and we have the limiting values

$$A = \lim_{\rho \to 0} \frac{|\rho|}{|\mathbf{R}|} = |\boldsymbol{x}_u(u,v)\cos\xi + \boldsymbol{x}_v(u,v)\sin\xi|^{-1} \tag{4.16}$$

$$\lim_{\rho \to 0} \frac{\mathbf{R}\cdot n_{\boldsymbol{x}}}{|\mathbf{R}|^2} = -\frac{1}{2}\kappa_n(u,v,\xi) = -\frac{A^2}{2}(\frac{d^2\boldsymbol{x}^*(\rho,\xi)}{d\rho^2}\cdot n_{\boldsymbol{x}}), \tag{4.17}$$

where $\kappa_n(u,v,\xi)$ is the curvature of the surface at the point $\boldsymbol{x}(u,v)$ in the direction

$$\boldsymbol{x}_u(u,v)\cos\xi + \boldsymbol{x}_v(u,v)\sin\xi.$$

Since the integrand in equation (4.15) is a smooth function of ρ, and in view of the factor $\eta_{\boldsymbol{x}}(\boldsymbol{x}')$, the corresponding integrand vanishes at the ends of the integration interval together with all of its derivatives, the integrand is smoothly periodic. Thus, we can and do use the trapezoidal rule to produce the radial quadratures with high order accuracy.

The trapezoidal rule also provides an appropriate high order integrator for the angular integration of equation (4.14), since the corresponding integrands are, once again, smooth periodic functions of ξ: we evaluate the angular integral by taking the sum of the integrands at a set of equi-spaced points $\xi_t (t = 1\dots)$ times the step-size of mesh ξ_t, $t = 1, \dots, N_t$. By symmetry, the range of the angular integration can be reduced from 2π to π. When we do this polar coordinates change of variables, the corresponding radial quadrature points do not lie on the Cartesian grid associated with the given coordinate patch. Thus, use of an appropriate interpolation strategy [6] is necessary for evaluation of the necessary function values at the radial integration points ρ_s, $s = -N_s, \dots, N_s$ for each angle $\xi = \xi_t$.

Polar integration in domain $\mathcal{H}^1$. Since the support set of the floating POU function in domain $\mathcal{H}^1$ is modified, in order to keep the periodicity of the integrand, the integration interval in equation (4.15) w.r.t. ρ should also be modified correspondingly. For example, for a point $(u,v) \in \mathcal{H}^1$ with $v < \gamma^1$ and at point (u,v), a radial line $\xi = \xi_t$ intersecting with the boundary line $v^1 = 0$, as we integrate on this radial line $\xi = \xi_t$ (integrate w.r.t. ρ), when proceeding to a point on line $v^1 = 0$ with coordinates $(u^1_{\boldsymbol{x}'}, 0)$, the integration should continue over to the point $(u^1_{\boldsymbol{x}'}, 1)$ on line $v^1 = 1$, and keep the same angle ξ_t, until reaching the boundary of the floating POU function support set.

4.2.2 Efficient interpolation scheme

To obtain accurately interpolated values of the integrand f_k^* at points lying on the lines

$$u' = u + \rho\cos\xi_t, \quad v' = v + \rho\sin\xi_t, \quad \xi_t = t\pi/n, \quad t = 0, \ldots, n-1,$$

from the corresponding values at the Cartesian nodes, we interpolate the products

$$b(u', v') \cdot \omega^1(\boldsymbol{x}^1(u', v')) \cdot J_1(u', v'). \tag{4.18}$$

$$b(u', v') \cdot \omega^2(\boldsymbol{x}^2(u', v')) \tag{4.19}$$

in the domains $\mathcal{H}^1$ and $\mathcal{H}^2$, respectively. Since, as explained in Section 4.1, the functions (4.18) and (4.19) are smoothly periodic, the interpolation scheme we describe in what follows exhibits a high order of accuracy.

The functions (4.18) and (4.19) to be interpolated are given by their values at the nodes

$$(u_{m'}^{k'}, v_{l'}^{k'}); \quad \text{where } u_{m'}^{k'} = m'\Delta u^{k'}, v_{l'}^{k'} = l'\Delta v^{k'}, m' = 0, \ldots, N_u^{k'}, l' = 0, \ldots, N_v^{k'}.$$

Thus, to evaluate an integral along the line

$$u^{k'} = u + \rho\cos\xi_t, \quad v^{k'} = v + \rho\sin\xi_t \quad \text{for } \xi_t \in [\pi/4, 3\pi/4],$$

we utilize a trapezoidal rule with discretization step

$$(\Delta\rho)_{\xi_t} = \frac{\Delta v^{k'}}{\sin\xi_t} \quad \text{on} \quad \xi = \xi_t,$$

in such a way that the radial discretization points are situated on the straight coordinate lines $v^{k'} = v_{l'}^{k'} = l'\Delta v^{k'}$; see [6].

Since for each fixed value $v^{k'} = v_{l'}^{k'} = l'\Delta v^{k'}$ the function is known at the equi-distant points $u^{k'} = u_{m'}^{k'} = m'\Delta u^{k'}$, a one-dimensional interpolation in the u direction suffices to provide all the required values. To speed up calculations while maintaining high order accuracy, we use the following interpolation and approximation algorithm:

1. Obtain the Fourier coefficients of the given function for each one of the lines $v^{k'} = v_{l'}^{k'} = l'\Delta v^{k'}$ by means of the fast Fourier transform.

2. Evaluate the resulting Fourier series on a much finer equi-spaced grid. These evaluations can be obtained efficiently by FFT.

3. On each interval of the refined grid construct an interpolating polynomial of degree 3 such that its values and the values coincide with those of the trigonometric polynomial at the endpoints of the interval.

As a result of this procedure, we obtain polynomial splines that closely approximate the interpolating Fourier series. We have explained the radial integrations on lines determined by angles ξ_t in the interval $[\pi/4, 3\pi/4]$. Integration over the lines corresponding to the complementary set of angles $\xi_t \in [0, \pi/4] \bigcap [\pi/4, 3\pi/4]$ can be performed similarly, in which case interpolations along the lines $u^{k'} = u^{k'}_{m'} = m'\Delta u^{k'}$ should be used; full details of the overall strategy can be found in Reference [6].

4.3 Hölder density singularity and graded meshes

In this section we show that smooth integrands indeed result, as asserted previously, from the use of polynomial-type change of variables (4.7) of appropriately chosen degrees. We establish this in the two cases arising from our use of floating POU (see Section 4.2): first for the integral away from target point (integrand containing the $(1-\eta)$ factor), and then for the integral around the target point (integrand containing the η factor).

Trapezoidal rule integration: integration away from the target point. In the case $\boldsymbol{x}$ is on the patch $\mathcal{P}^1$ we use the trapezoidal rule to evaluate the integral

$$\int_{\mathcal{H}^1} \frac{\partial G(\boldsymbol{x}, \boldsymbol{x}^1(u^1_{\boldsymbol{x}'}, v^1_{\boldsymbol{x}'}))}{\partial n_{\boldsymbol{x}}} b(\boldsymbol{x}^1(u^1_{\boldsymbol{x}'}, v^1_{\boldsymbol{x}'})) J_1(u^1_{\boldsymbol{x}'}, v^1_{\boldsymbol{x}'}) \omega^1(\boldsymbol{x}^1(u^1_{\boldsymbol{x}'}, v^1_{\boldsymbol{x}'})) \cdot (1 - \eta_{\boldsymbol{x}}(\boldsymbol{x}^1(u^1_{\boldsymbol{x}'}, v^1_{\boldsymbol{x}'}))) du^1_{\boldsymbol{x}'} dv^1_{\boldsymbol{x}'}. \tag{4.20}$$

As long as the target point $\boldsymbol{x}$ is not close to the conical point O, it is easy to check that the integrand in equation (4.20) vanishes smoothly as $u^1_{\boldsymbol{x}'} \to 0$—since the Jacobian $J_1(u^1_{\boldsymbol{x}'}, v^1_{\boldsymbol{x}'}) \sim {u^1_{\boldsymbol{x}'}}^{2n_u - 1} \to 0$ as $u^1_{\boldsymbol{x}'} \to 0$ and all other terms in the integrand are bounded functions.

As $\boldsymbol{x}$ approaches the conical point O, the integration kernel

$$\frac{\partial G(\boldsymbol{x},\boldsymbol{x}')}{\partial n_{\boldsymbol{x}}} = \frac{\mathbf{R}\cdot n_{\boldsymbol{x}}}{4\pi|\mathbf{R}|^3}$$

becomes more and more singular for points $\boldsymbol{x}'$ also close to the conical point, however, and the question arises as to whether the kernel will remain uniformly smooth, and thus make the trapezoidal rule accurate to uniform high-order for points $\boldsymbol{x}$ arbitrarily close to the conical point.

In order to demonstrate the kernel singularity, we note that, on a smooth portion of the surface, the vector

$$\frac{\mathbf{R}}{|\mathbf{R}|} = \frac{\boldsymbol{x}-\boldsymbol{x}'}{|\boldsymbol{x}-\boldsymbol{x}'|}$$

is nearly tangent to ∂D for $\boldsymbol{x}$ close to $\boldsymbol{x}'$, and it becomes orthogonal to the normal vector $n_{\boldsymbol{x}}$ as $\boldsymbol{x}' \to \boldsymbol{x}$. Consequently, the numerator of the integration kernel $\mathbf{R}\cdot n_{\boldsymbol{x}}$ vanishes to second order as $\mathbf{R}\to 0$, since both quantities $\frac{\mathbf{R}}{|\mathbf{R}|}\cdot n_{\boldsymbol{x}}$ and $|\mathbf{R}|$ vanish in the limit $|\mathbf{R}|\to 0$.

When both $\boldsymbol{x}$ and $\boldsymbol{x}'$ are close to the conical point O, however, the near orthogonality between $\frac{\mathbf{R}}{|\mathbf{R}|}$ and the normal $n_{\boldsymbol{x}}$ is lost. For example, when $\boldsymbol{x}\to O$ on a curve on ∂D of all points with a constant $\theta_{\boldsymbol{x}}$ value (see Figure 2.12), and $\boldsymbol{x}'$ is on a curve on ∂D given by a different angle $\theta_{\boldsymbol{x}'}$ ($\theta_{\boldsymbol{x}'}\neq\theta_{\boldsymbol{x}}$), $|\mathbf{R}| = |\boldsymbol{x}-\boldsymbol{x}'|$ can be small while $\frac{\mathbf{R}}{|\mathbf{R}|}$ is not orthogonal to $n_{\boldsymbol{x}}$. Clearly, along these curves the denominator in the kernel $\frac{\partial G(\boldsymbol{x},\boldsymbol{x}')}{\partial n_{\boldsymbol{x}}}$ vanishes cubically (like $|\mathbf{R}|^3$), while the numerator vanishes to first order only. The special geometrical arrangements of $\boldsymbol{x}$ and $\boldsymbol{x}'$ that take place when these points lie in a neighborhood of the conical point O have a significant impact in the character of the integral and differential equations under consideration as well as their solutions. In what follows we show that, in spite of the singularity of the kernel at the conical point O, use of polynomial-type change of variables (4.7) of appropriately chosen degrees does result in smooth integrands.

In order to analyze the singular behavior of the integrand at the conical point it suffices to restrict attention to the integrand in equation (4.20) for the target point $\boldsymbol{x}\in S_\sigma$ and the coordinates $(u^1_{\boldsymbol{x}'}, v^1_{\boldsymbol{x}'}) \in (\boldsymbol{x}^1)^{-1}(S_\sigma) \in \mathcal{H}^1$: points $\boldsymbol{x}$ and $\boldsymbol{x}'$ sufficiently close to the conical point clearly lie within S_σ. With these restrictions, the fixed POU function $\omega^1(\boldsymbol{x}^1(u^1_{\boldsymbol{x}'}, v^1_{\boldsymbol{x}'}))$

is equal to 1, and according to remark 4.1.2, the parametrization (4.6) simplifies to

$$\begin{cases} x_{\boldsymbol{x}} &= h(u^1)^{n_u} F_x(2\pi v^1) \\ y_{\boldsymbol{x}} &= h(u^1)^{n_u} F_y(2\pi v^1) \\ z_{\boldsymbol{x}} &= h(u^1)^{n_u}. \end{cases} \tag{4.21}$$

In terms of the parametrization (4.21), the integrand in equation (4.20) can be expressed in the form

$$W(v^1_{\boldsymbol{x}}, v^1_{\boldsymbol{x}'})(1 - \eta_{\boldsymbol{x}}(\boldsymbol{x}^1(u^1_{\boldsymbol{x}'}, v^1_{\boldsymbol{x}'})))b(\boldsymbol{x}^1(u^1_{\boldsymbol{x}'}, v^1_{\boldsymbol{x}'})) \cdot \frac{(u^1)^{3n_u-1}_{\boldsymbol{x}'}}{[D_1 + D_2 + D_3]^{\frac{3}{2}}}, \tag{4.22}$$

where

$$\begin{aligned} D_1 &= ((u^1_{\boldsymbol{x}})^{n_u} F_x(2\pi v^1_{\boldsymbol{x}}) - (u^1_{\boldsymbol{x}'})^{n_u} F_x(2\pi v^1_{\boldsymbol{x}'}))^2, \\ D_2 &= ((u^1_{\boldsymbol{x}})^{n_u} F_y(2\pi v^1_{\boldsymbol{x}}) - (u^1_{\boldsymbol{x}'})^{n_u} F_y(2\pi v^1_{\boldsymbol{x}'}))^2, \qquad \text{and} \\ D_3 &= ((u^1_{\boldsymbol{x}})^{n_u} - (u^1_{\boldsymbol{x}'})^{n_u})^2, \end{aligned} \tag{4.23}$$

and where $W(v^1_{\boldsymbol{x}}, v^1_{\boldsymbol{x}'})$ equals the product of the $(v^1_{\boldsymbol{x}}, v^1_{\boldsymbol{x}'})$-dependent components of the Jacobian $J_1(u^1_{\boldsymbol{x}'}, v^1_{\boldsymbol{x}'})$, and the integration kernel $\frac{\partial G(\boldsymbol{x}, \boldsymbol{x}^1(u^1_{\boldsymbol{x}'}, v^1_{\boldsymbol{x}'}))}{\partial n_{\boldsymbol{x}}}$. Clearly, in the present context, the function $W(v^1_{\boldsymbol{x}}, v^1_{\boldsymbol{x}'})$ can be expressed in terms of the functions $F_x(2\pi v^1)$ and $F_y(2\pi v^1)$.

In order to evaluate our integral operator, we must use values of the integrand on an equi-spaced mesh in the domain $(u^1_{\boldsymbol{x}'}, v^1_{\boldsymbol{x}'}) \in [0,1] \times [0,1]$. Denoting by h the step size of this mesh in the u^1 direction, the integrand is evaluated at mesh points with integration- and target-point coordinates given by $u^1_{\boldsymbol{x}'} = h, 2h, 3h \ldots$, and $u^1_{\boldsymbol{x}} = h, 2h, 3h \ldots$, respectively. In particular, in the discrete formulation, $u^1_{\boldsymbol{x}}$ and $u^1_{\boldsymbol{x}'}$ can both take the value of the step size h, which tends to 0 as the mesh is refined.

Since $b(\boldsymbol{x}') \sim r^p_{\boldsymbol{x}'}$ for some $p > 0$ as $r_{\boldsymbol{x}'} \to 0$ (see [9]), it follows that $b(\boldsymbol{x}') \sim (u^1_{\boldsymbol{x}'})^{n_u p}$. Using this asymptotic formula, we see that all the components of the integrand in (4.22) depending on $u^1_{\boldsymbol{x}}$ and $u^1_{\boldsymbol{x}'}$ are smooth functions multiplied by the quantity

$$F(u^1_{\boldsymbol{x}}, u^1_{\boldsymbol{x}'}) = \frac{(u^1_{\boldsymbol{x}'})^{3n_u + n_u p - 1}}{[D_1 + D_2 + D_3]^{\frac{3}{2}}}. \tag{4.24}$$

An important situation in which the smoothness of the function $F(u^1_{\boldsymbol{x}}, u^1_{\boldsymbol{x}'})$ must be studied

occurs in the limit

$$\lim_{\boldsymbol{x}\to O}\int_{\partial D}\frac{\partial G(\boldsymbol{x},\boldsymbol{x}')}{\partial n_{\boldsymbol{x}}}b(\boldsymbol{x}')dS(\boldsymbol{x}'),$$

—whose evaluation is necessary in our method to solve the integral equation problem (1.7). When $\boldsymbol{x}\to O$, $u^1_{\boldsymbol{x}}\to 0$, and, thus,

$$F(u^1_{\boldsymbol{x}},u^1_{\boldsymbol{x}'})\sim(u^1_{\boldsymbol{x}'})^{n_u p-1},$$

which vanishes if $n_u p > 1$, and tends to ∞ if $n_u p < 1$. This condition thus provides a constraint on the possible values of n_u that can be used by our algorithm for a given p: we must select n_u so as to guarantee that the condition $n_u p > 1$ is satisfied.

A related but different situation arises when the point $\boldsymbol{x}$ is different from but close to the conical point—a situation that occurs, for example, when $u^1_{\boldsymbol{x}}$ is equal to the step size h of the mesh in the u^1 direction. Figures 4.10 and 4.11 display the integrands, for the (arbitrary but otherwise reasonable, see e.g., Figure 6.8) sample exponent $p = 0.3$, for the change-of-variables exponent $n_u = 1$ (no change of variables) and $n_u = 7$ (high-order change of variables). Specifically, for this example we used an elliptical-conical-point surface, as defined in Chapter 6, and we take $b(\boldsymbol{x}) = r_{\boldsymbol{x}}^{0.3}\sin(\theta_{\boldsymbol{x}})$. As shown in these two figures, the integrand becomes smoother as n_u is increased. Corresponding one-dimensional graphs (integrand as a function of $u_{\boldsymbol{x}'}$ for $u_{\boldsymbol{x}} = 1/128$) are presented in Figure 4.9 for three values of n_u, showing, once again, that higher values of n_u give rise to smoother integrands.

In our context, the added smoothness translates into significantly higher-quality integration: Table 4.1 demonstrates the increase in accuracy that results as the high-order change of variables is used. This table displays the errors arising from use of the trapezoidal quadrature rule (4.9) to produce the integral (4.20), for the two values of n_u chosen, and for the target point $\boldsymbol{x}$ set to equal $\boldsymbol{x}^1(h, v^1 = 0.53)$, where h is the mesh size used, and v^1 is arbitrarily set at 0.53. (The errors were evaluated by comparison with the results obtained by means of fine 256×256 integration meshes for each power n_u.) Clearly, use of the smoothing change of variables has a highly beneficial effect.

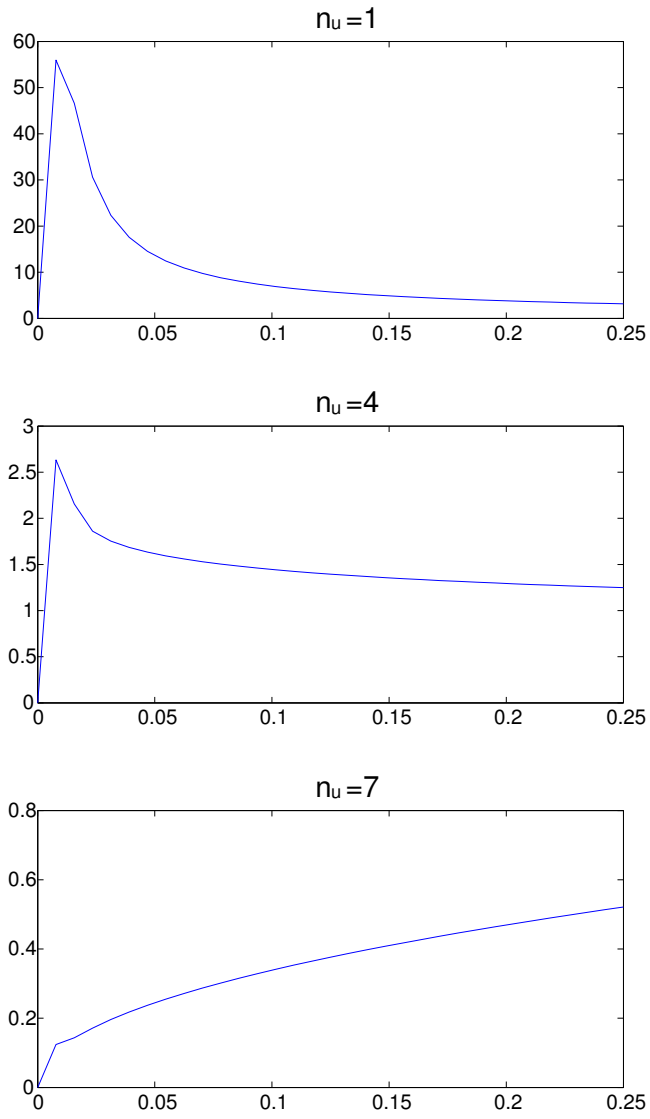

Figure 4.9: Integrand as a function of $u^1_{\boldsymbol{x}'}$ for various values of n_u.

Mesh	Error ($n_u = 1$)	Error ($n_u = 7$)
16×16	1.7×10^{-3}	7×10^{-3}
32×32	1×10^{-3}	1.3×10^{-4}
64×64	7×10^{-4}	8×10^{-5}
128×128	4×10^{-4}	6×10^{-6}
Integrals	$\sim 4 \times 10^{-2}$	

Table 4.1: Errors arising from use of the trapezoidal quadrature for evaluation of the integral (4.20) using two values of the change-of-variables exponent n_u.

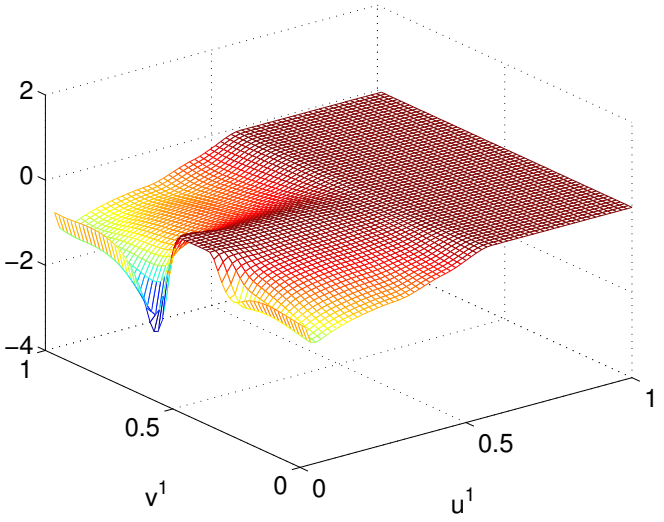

Figure 4.10: For $n_u = 1$ and r close to 0, the integrand containing the $(1 - \eta_{\boldsymbol{x}}(\boldsymbol{x}'))$ factor has a large peak around $r' = 0$ that is not uniformly-integrable as $r \to 0$.

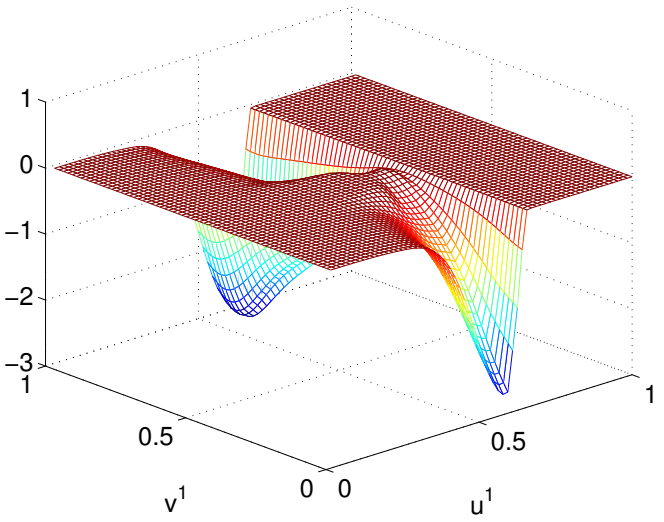

Figure 4.11: Integrand containing the $(1 - \eta_{\boldsymbol{x}}(\boldsymbol{x}'))$ factor and incorporating an $n_u = 7$ change of variables. Clearly this change of variables effectively eliminates the $r' = 0$ peak shown in Figure 4.10.

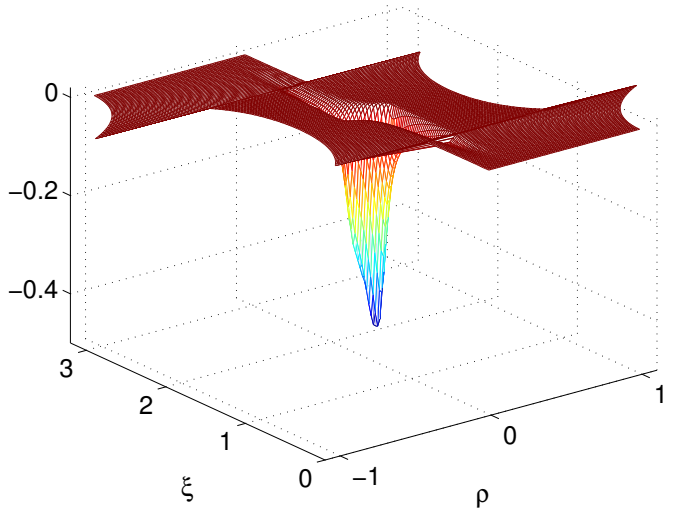

Figure 4.12: For $n_u = 1$ and r close to 0, the integrand containing the $\eta_{\boldsymbol{x}}(\boldsymbol{x}')$ factor has a large peak around $r' = 0$ that is not uniformly-integrable as $r \to 0$.

Polar integration; integration around the target point. We now consider the remaining case to be discussed in this section: evaluation of the integral around the target point, i.e.,

$$\int_{\mathcal{H}^1} \frac{\partial G(\boldsymbol{x}, \boldsymbol{x}^1(u^1_{\boldsymbol{x}'}, v^1_{\boldsymbol{x}'}))}{\partial n_{\boldsymbol{x}}} b(\boldsymbol{x}^1(u^1_{\boldsymbol{x}'}, v^1_{\boldsymbol{x}'})) J_1(u^1_{\boldsymbol{x}'}, v^1_{\boldsymbol{x}'}) \omega^1(\boldsymbol{x}^1(u^1_{\boldsymbol{x}'}, v^1_{\boldsymbol{x}'})) \cdot \eta_{\boldsymbol{x}}(\boldsymbol{x}^1(u^1_{\boldsymbol{x}'}, v^1_{\boldsymbol{x}'})) du^1_{\boldsymbol{x}'} dv^1_{\boldsymbol{x}'}. \tag{4.25}$$

In Figures 4.12 and 4.13 we display the integrands in equation (4.25) as functions of the polar coordinates ρ and ξ, and using the change-of-variable powers $n_u = 1$ and $n_u = 7$, respectively. Once again, we see that the higher-order change of variables gives rise to a smoother integrand: note, in particular, that the significant peak in Figure 4.12 is not even discernible in Figure 4.13, and that only traces of the features prominent in Figure 4.11 have remained in Figure 4.13.

In Table 4.2, in turn, we present the numerical errors arising from the integration scheme described in Section 4.2; once again we use the value obtained from a 256×256 meshes to evaluate the errors resulting from the coarser meshes. Clearly, the integrand resulting from the change of variables $\frac{z^1}{h} = (u^1)^{n(u^1)}$ with $n_u = 7$ gives rise to significant improvements in the integral evaluations; the value $n_u = 7$ is used in all of the numerical examples presented in Chapter 6.

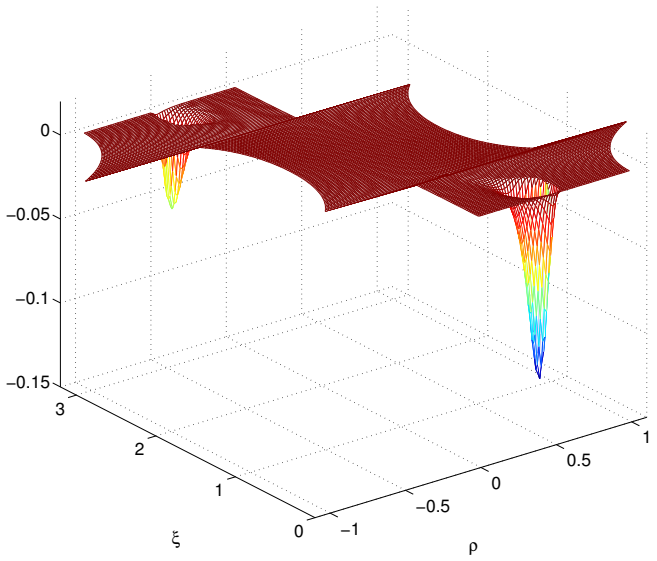

Figure 4.13: Integrand containing the $\eta_{\boldsymbol{x}}(\boldsymbol{x}')$ factor and incorporating an $n_u = 7$ change of variables. Clearly this change of variables effectively eliminates the $r' = 0$ peak shown in Figure 4.12.

Mesh	Error ($n_u = 1$)	Error ($n_u = 7$)
16×16	2.6×10^{-4}	4.3×10^{-4}
32×32	8×10^{-5}	1.7×10^{-5}
64×64	1.7×10^{-5}	1×10^{-7}
128×128	1.6×10^{-6}	5×10^{-9}
Integrals	$\sim 4 \times 10^{-3}$	

Table 4.2: Errors arising from use of the trapezoidal quadrature for evaluation of the integral (4.25) using two values of the change-of-variables exponent n_u.

4.4 Evaluation of $-\frac{a_i(\theta_{\boldsymbol{x}})}{2r_{\boldsymbol{x}}^{q_i}}\hat{\omega}_{\mathcal{P}^1}(\boldsymbol{x}) + \int_{\mathcal{P}^1} \frac{\partial G(\boldsymbol{x},\boldsymbol{x}')}{\partial n_{\boldsymbol{x}}} \frac{a_i(\theta_{\boldsymbol{x}'})}{r_{\boldsymbol{x}'}^{q_i}}\hat{\omega}_{\mathcal{P}^1}(\boldsymbol{x}')dS(\boldsymbol{x}')$

Case $\boldsymbol{x} \in (\partial D) \setminus S_{\frac{\sigma}{10}}$. To numerically evaluate the integral (4.2) in cases in which the target point $\boldsymbol{x} \in (\partial D)\setminus S_{\frac{\sigma}{10}}$ (so that, in particular, $\boldsymbol{x}$ is not close to the conical point), our algorithm uses a combination of the trapezoidal rule described in equations (4.9) and (4.13), with the polar integration procedure described in Section 4.2. Clearly, it is necessary to replace the nodal values $b^{k'}_{m',l'}$ by the approximation to the singular term $\frac{a_i(\theta_{\boldsymbol{x}'})}{r_{\boldsymbol{x}'}^{q_i}}$ at nodes $(u^{k'}_{m'}, v^{k'}_{l'})$, which, according to Remark 3.1.2, can be evaluated without difficulty. Moreover, since we can evaluate numerically the singular term $\frac{a_i(\theta_{\boldsymbol{x}'})}{r_{\boldsymbol{x}'}^{q_i}}$ for any point $\boldsymbol{x}^1(u^1_{\boldsymbol{x}'}, v^1_{\boldsymbol{x}'})$, we can perform the polar integration procedure described in Section 4.2 using such direct evaluations instead of the interpolation scheme described in Section 4.2.2.

We can also evaluate the term $\frac{a_i(\theta_{\boldsymbol{x}})}{2r_{\boldsymbol{x}}^{q_i}}\hat{\omega}_{\mathcal{P}^1}(\boldsymbol{x})$ for a target point $\boldsymbol{x}^1(u^1_{\boldsymbol{x}}, v^1_{\boldsymbol{x}})$ away from the conical point. Thus, combining this quantity with the value of the integral in equation (4.2), we obtain the numerical value of the sum

$$-\frac{a_i(\theta_{\boldsymbol{x}})}{2r_{\boldsymbol{x}}^{q_i}}\hat{\omega}_{\mathcal{P}^1}(\boldsymbol{x}) + \int_{\mathcal{P}^1} \frac{\partial G(\boldsymbol{x},\boldsymbol{x}')}{\partial n_{\boldsymbol{x}}} \frac{a_i(\theta_{\boldsymbol{x}'})}{r_{\boldsymbol{x}'}^{q_i}}\hat{\omega}_{\mathcal{P}^1}(\boldsymbol{x}')dS(\boldsymbol{x}') \tag{4.26}$$

for any target point $\boldsymbol{x}^1(u^1_{\boldsymbol{x}}, v^1_{\boldsymbol{x}})$.

Remark 4.4.1. *It is shown in [32], that all exponents q_i are smaller than 1. Since, further, $J_1(u^1, v^1) \sim (u^1)^{2n_u-1}$, we have that, in the present case $\boldsymbol{x} \in (\partial D) \setminus S_{\frac{\sigma}{10}}$, $J_1(u^1, v^1)\frac{a_i(\theta_{\boldsymbol{x}^1(u^1,v^1)})}{r_{\boldsymbol{x}^1(u^1,v^1)}^{q_i}}$ and several of its derivatives tend to 0 as u^1 tends to 0. Thus the integrand in equation (4.2) is a smooth and periodic function for $\boldsymbol{x} \in (\partial D) \setminus S_{\frac{\sigma}{10}}$.*

Case $\boldsymbol{x} \in S_{\frac{\sigma}{10}}$. For cases in which the target point $\boldsymbol{x} \in S_{\frac{\sigma}{10}}$ the kernel is not singular in the integral (4.3)—since $S_{\frac{\sigma}{10}}$ does not overlap with the integration region $\mathcal{P}^1 \setminus S_\sigma$. Moreover, the integration region $\mathcal{P}^1 \setminus S_\sigma$ is bounded away from the region near $r_{\boldsymbol{x}'} = 0$, where the singular term $\frac{a_i(\theta_{\boldsymbol{x}'})}{r_{\boldsymbol{x}'}^{q_i}}$ tends to ∞. So the integrand in equation (4.3) is smooth. We use Simpson's rule on a very fine mesh in the integration domain $(\boldsymbol{x}^1)^{-1}(\mathcal{P}^1 \setminus S_\sigma)$ for the evaluation of this integral. Adding the integral (4.3) to the sum in equation we already evaluated in Section 3.2, we obtain the sum in equation (4.26) for $\boldsymbol{x} \in S_{\frac{\sigma}{10}}$.

Chapter 5

The discrete linear system and accurate evaluation of disparate singular quantities

After summarizing and combining in Section 5.1 the numerical methods introduced in previous Chapters for the portion of the operator involving the singular terms on the left hand side of equation (3.4), we present, in Section 5.2, the overall linear system for the discrete form of this integral equation, including the all-important conical-point equations. This linear system is suitable for evaluation of a numerical solution by means of an iterative solver such as GMRES.

Since the integral equations under consideration admit solutions that tend to ∞ at the conical point, conditioning issues can give rise to inaccurate evaluation of the the bounded component $b(\boldsymbol{x})$ of the decomposition (3.1). In the last section of this Chapter, Section 5.3, we consider this problem and we present a preconditioning strategy that removes the ill conditioning to some extent, and improves the convergence for the quantity, $b(\boldsymbol{x})$ for points $\boldsymbol{x}$ arbitrarily close to the conical point.

5.1 The overall discrete operator

According to the descriptions in the previous chapters, in order to construct the discrete version of the operator on the left hand side of equation (3.4), that is, the operator

$$\begin{aligned}\sum_i \left(-\frac{1}{2}\frac{c_i a_i(\theta_{\boldsymbol{x}})}{r_{\boldsymbol{x}}^{q_i}}\hat{\omega}_{\mathcal{P}^1}(\boldsymbol{x}) + \int_{\mathcal{P}^1}\frac{\partial G(\boldsymbol{x},\boldsymbol{x}')}{\partial n_{\boldsymbol{x}}}\frac{c_i a_i(\theta_{\boldsymbol{x}'})}{r_{\boldsymbol{x}'}^{q_i}}\hat{\omega}_{\mathcal{P}^1}(\boldsymbol{x}')dS(\boldsymbol{x}')\right) \\ + \left(-\frac{b(\boldsymbol{x})}{2} + \int_{\partial D}\frac{\partial G(\boldsymbol{x},\boldsymbol{x}')}{\partial n_{\boldsymbol{x}}}\cdot b(\boldsymbol{x}')dS(\boldsymbol{x}')\right),\end{aligned} \tag{5.1}$$

we start by evaluating the components involving the singular term, as indicated in what follows:

1. We evaluate the singular pairs $\{q_i, \{a_i^j, j = 1, \ldots, N_{sp}\}\}$ using equation (3.27).

2. With $\{q_i, \{a_i^j, j = 1, \ldots, N_{sp}\}\}$ we evaluate the sum in equation (4.26) for the target point positioned at a mesh point: $\boldsymbol{x} = \boldsymbol{x}^k(u_m^k, v_l^k)$ (The equi-spaced mesh (u_m^k, v_l^k) is introduced in Section 4.1). To evaluate (4.26) for points $\boldsymbol{x} = \boldsymbol{x}^k(u_m^k, v_l^k) \in S_{\frac{\sigma}{10}} \setminus O$, we use equation (3.38) to evaluate the sum (3.31) and proceed with the evaluation method described in Section 4.4 for the integral in equation (4.3). Adding these two contributions, we obtain the sum in equation (4.26). To evaluate the sum (4.26) in the limit $x^1(u_m^1 \to 0, v_l^1)$, in turn, we use the algorithm (3.38) with $r_{\boldsymbol{x}}$ set to 0.

3. For the target point $\boldsymbol{x} = \boldsymbol{x}^k(u_m^k, v_l^k) \in \mathcal{P}^1 \setminus S_{\frac{\sigma}{10}}$, as described in Section 4.4, we use the same scheme described in Sections 4.1 and 4.2 to evaluate the integral in equation (4.2), and take the sum of it with the singular term $-\frac{1}{2}\frac{a_i(\theta_{\boldsymbol{x}})}{r_{\boldsymbol{x}}^{q_i}}\hat{\omega}_{\mathcal{P}^1}(\boldsymbol{x})$. So as to obtain the sum in equation (4.26).

Since, as mentioned earlier, the surface ∂D determines the singular pairs (q_i, a_i^j), the evaluation procedure above needs to be performed only once for a given surface. For a given target point $\boldsymbol{x}$, we denote the numerical evaluation of the sum in equation (4.26) involving the singular terms by $Q_{\boldsymbol{x}}^+(a_i^{j'}, q_i)$:

$$Q_{\boldsymbol{x}}^+(a_i^{j'}, q_i) \simeq -\frac{a_i(\theta_{\boldsymbol{x}})}{2r_{\boldsymbol{x}}^{q_i}}\hat{\omega}_{\mathcal{P}^1}(\boldsymbol{x}) + \int_{\mathcal{P}^1}\frac{\partial G(\boldsymbol{x},\boldsymbol{x}')}{\partial n_{\boldsymbol{x}}}\frac{a_i(\theta_{\boldsymbol{x}'})}{r_{\boldsymbol{x}'}^{q_i}}\hat{\omega}_{\mathcal{P}^1}(\boldsymbol{x}')dS(\boldsymbol{x}'). \tag{5.2}$$

5.2 Discrete linear system

Recall the definition, given in Section 4.1, of the equi-spaced mesh $(u^{k'}_{m'}, v^{k'}_{l'})$ and associated nodal values $b^{k'}_{m',l'}$ that are used by our algorithm for numerical evaluation of the integral

$$\int_{\partial D} \frac{\partial G(\boldsymbol{x}, \boldsymbol{x}')}{\partial n_{\boldsymbol{x}}} b(\boldsymbol{x}') dS(\boldsymbol{x}'). \tag{5.3}$$

Our complete procedure for the numerical evaluation of this integral is described in Sections 4.1 and 4.2. In what follows we denote by $Q_{\boldsymbol{x}}(b^{k'}_{m',l'})$ the approximate integral provided by this algorithm on the basis of the nodal values $b^{k'}_{m',l'}$:

$$Q_{\boldsymbol{x}}(b^{k'}_{m',l'}) \simeq \int_{\partial D} \frac{\partial G(\boldsymbol{x}, \boldsymbol{x}')}{\partial n_{\boldsymbol{x}}} b(\boldsymbol{x}') dS(\boldsymbol{x}'). \tag{5.4}$$

We construct our linear system by evaluating high-order accurate numerical approximations each one of the terms the integral operator in equation (5.1); clearly, the unknowns in our problem are the quantities $b^{k'}_{m',l'}$ arising from the operator (5.3) and the quantities c_i in (5.1). Thus, we obtain a part of our linear system by enforcing a discrete version of equation (3.4) at each one of the mesh points $\boldsymbol{x}^k(u^k_m, v^k_l)$:

$$\begin{aligned} &\sum_{i=1}^{\chi} c_i \left(Q^+_{\boldsymbol{x}^k(u^k_m, v^k_l)}(a_i^{j'}, q_i) \right) + \left(-\frac{b^k_{m,l}}{2} + Q_{\boldsymbol{x}^k(u^k_m, v^k_l)}(b^{k'}_{m',l'}) \right) \\ &= g(\boldsymbol{x}^k(u^k_m, v^k_l)) \quad \text{for all } \{k, m, l\} \end{aligned} \tag{5.5}$$

where $Q^+_{\boldsymbol{x}^k(u^k_m, v^k_l)}(a_i^{j'}, q_i)$ is defined in equation (5.2); as shown in what follows, additional "conical-point" equations must be included, that correspond in some sense to the unknowns c_i, to obtain a uniquely solvable system of equations.

Clearly, the system (5.5) contains $\sum_k N^k_u \times N^k_v$ equations and $\sum_k N^k_u \times N^k_v + \chi$ unknowns: an additional χ equations must be obtained. We do this by considering the action of the operator at the conical point O. Specifically, we first take the difference of the limit of both sides of equation (5.5) as $\boldsymbol{x} \to O$ in N^1_v different directions: using equation (3.38) with $r_{\boldsymbol{x}}$ set to 0, we can obtain the limit $Q^+_{\boldsymbol{x}^k(u^1 \to 0, v^1_l)}(a_i^{j'}, q_i)$; noting that (5.4) can be evaluated numerically at any target point, including the conical point itself (by means of the method described in Sections 4.1 and 4.2), in turn, the limit $Q_{\boldsymbol{x}^k(u^1 \to 0, v^1_l)}(b^{k'}_{m',l'})$ can be obtained

simply by integration for the value $u^1 = 0$. We can thus obtain the quantities

$$h(v_l^1) = g(\boldsymbol{x}^1(u^1 \to 0, v_l^1)) - \sum_i c_i \left(Q^+_{\boldsymbol{x}^1(u^1 \to 0, v_l^1)}(a_i^{j'}, q_i) \right) - Q_{\boldsymbol{x}^1(u^1 \to 0, v_l^1)}(b^{k'}_{m',l'}) \quad \text{for } l = 1, \ldots, N_v^1, \tag{5.6}$$

where a term of the form $-\frac{b^k_{0,l}}{2}$ is not incorporated (compare equation (5.5)) since, indeed, $b(\boldsymbol{x})$ vanishes at the conical point [32]. Note that according to equation (5.5), the quantity $h(v_l^1)$ is an approximation to the term $\frac{b(\boldsymbol{x}^1(u^1 \to 0, v_l^1))}{2}$:

$$\frac{b(\boldsymbol{x}^1(u^1 \to 0, v_l^1)}{2} \simeq h(v_l^1) \quad \text{for } l = 1, \ldots, N_v^1,$$

which should vanish. In order to enable our linear system to enforce the vanishing of this quantity we need to provide a means to distinguish between the unknowns b and c_i; we do this by incorporating a number χ of "conical-point" equations of the form

$$\sum_l h(v_l^1) \cdot a(\theta_{\boldsymbol{x}^1(u^1 \to 0, v_l^1)}) = 0 \quad \text{for } i = 1, \ldots, \chi. \tag{5.7}$$

That is, we enforce an orthogonality condition between $h(\theta_{l'})$ and $a(\theta_{\boldsymbol{x}^1(u^1 \to 0, v_l^1)}), l = 1, \ldots, N_v^1$: clearly these conditions identifies b as a quantity that does not tend to infinity at the conical point. Equations (5.5) and (5.7) form our complete linear system, which we solve by using an iterative linear solver GMRES.

5.3 Conical-point preconditioning

In the continuous formulation, the singular terms $\sum_i c_i \frac{a_i(\theta_{\boldsymbol{x}})}{r_{\boldsymbol{x}}^{q_i}}$ and the regular term $b(\boldsymbol{x})$ are separated in the equation (3.4), so that $b(\boldsymbol{x}) \to 0$ as $\boldsymbol{x}$ tends to the conical point O; as shown in Sections 4.1 and 4.3 our discrete quadrature rule for the integral with function $b(\boldsymbol{x})$,

$$\int_{\partial D} \frac{\partial G(\boldsymbol{x}, \boldsymbol{x}')}{\partial n_{\boldsymbol{x}}} \cdot b(\boldsymbol{x}') dS(\boldsymbol{x}')$$

produces a high order of accuracy as a result of the fact that the integrand is smooth and periodic in the integration variables associated with the domains $\mathcal{H}^k$.

We have observed that errors introduced in the solution of the linear equations (5.5)

and (5.7) can give rise to significant errors in the qualitative behavior of $b(\boldsymbol{x})$ as $\boldsymbol{x}$ tends to the conical point, $b(\boldsymbol{x})$ should tend to zero as $\boldsymbol{x}$ approaches the conical point, yet some numerical solutions can exhibit a large peak instead; see e.g., Figure 5.1. This behavior suggests a degree of ill-conditioning in the determination of the quantity b near the conical point. (This is quite reasonable: recall that the true unknown in the problem is the sum $\nu = b(\boldsymbol{x}) + \sum_i \frac{c_i a(\theta_{\boldsymbol{x}})}{r_{\boldsymbol{x}}^{q_i}}$ of $b(\boldsymbol{x})$ and a term that tends to infinity at the conical point!)

In Figures 5.1, and 5.2 we display some of the the values of $b^1_{m,l_o}, m = 1, \ldots, N^1_u$ produced from our linear system by means of the iterative solver GMRES: the nodal values are shown for nodes along a polar curve of the surface ∂D. (Using the coordinates $(r_{\boldsymbol{x}}, \theta_{\boldsymbol{x}})$ defined in equation (2.5) a polar curve is given by $\theta_{\boldsymbol{x}} = \text{Const}$: a polar curve is a planar curve in ∂D that joins the conical point to the top of the cone body). In order to correct the numerical errors in $b(\boldsymbol{x})$ that are evident in Figures 5.1, and 5.2, we decrease the residue level ϵ for the GMRES convergence criterion. As shown in Figure 5.3, setting as low as $\epsilon = 10^{-16}$ we begin to obtain a solution $b(\boldsymbol{x})$ with a correct qualitative behavior. Unfortunately, however, the achievement of the low GMRES residue level requires a large and sometimes unacceptable number of iterations—increasingly so for finer and finer meshes.

In order to reduce the numerical errors in $b(\boldsymbol{x})$ we can instead modify the linear equations and the ill-conditioning inherent in the original problem: we recast equation (3.4), in the "preconditioned" form

$$\begin{aligned}
&\sum_i \left(-\frac{c_i a_i(\theta_{\boldsymbol{x}})}{2 r_{\boldsymbol{x}}^{q_i}} \hat{\omega}_{\mathcal{P}^1}(\boldsymbol{x}) + \int_{\mathcal{P}^1} \frac{\partial G(\boldsymbol{x}, \boldsymbol{x}')}{\partial n_{\boldsymbol{x}}} \frac{c_i a_i(\theta_{\boldsymbol{x}'})}{r_{\boldsymbol{x}'}^{q_i}} \hat{\omega}_{\mathcal{P}^1}(\boldsymbol{x}') dS(\boldsymbol{x}') \right) \\
&\quad + \left(-\frac{\tilde{b}(\boldsymbol{x})}{2 r_{\boldsymbol{x}}^{d}} + \int_{\partial D} \frac{\partial G(\boldsymbol{x}, \boldsymbol{x}')}{\partial n_{\boldsymbol{x}}} \frac{\tilde{b}(\boldsymbol{x}')}{r_{\boldsymbol{x}'}^{d}} dS(\boldsymbol{x}') \right) \\
&= g(\boldsymbol{x})
\end{aligned} \tag{5.8}$$

with some positive quantity d, where we have made the substitution

$$b(\boldsymbol{x}) = \frac{\tilde{b}(\boldsymbol{x})}{r_{\boldsymbol{x}}^{d}}; \tag{5.9}$$

clearly, in the discrete formulation the factor $1/r_{\boldsymbol{x}'}^{d}$ we introduced appears as a diagonal preconditioner. As shown in what follows, the preconditioned system determines b with a decreased degree of ill conditioning.

ϵ	Iterations	Accuracy Indicator
10^{-14}	86	Figure 5.2
10^{-15}	146	
10^{-16}	206	Figure 5.3
10^{-17}	238	Figure 5.4, in red
10^{-18}	268	

ϵ	Iterations	Accuracy Indicator
10^{-5}	84	
10^{-6}	116	
10^{-7}	146	
10^{-8}	177	Figure 5.4, in blue

Table 5.1: GMRES residual tolerances ϵ, number of iterations required to meet such tolerances, and accuracy indicators for the un-preconditioned (table on the left) and preconditioned (table on the right) systems.

With the modification embodied in equation (5.8), the error tolerance ϵ required in GMRES and the corresponding number of iterations it takes to converge to produce b with a given error level both change. To demonstrate the improvements arising from use of the preconditioned system, we present an example concerning a circular-conical-point surface with a right-hand-side $\frac{\partial N(\boldsymbol{x})}{\partial n}$. (The definition of both the circular-conical-point surface and the right-hand-side $\frac{\partial N(\boldsymbol{x})}{\partial n}$ are given in Chapter 6). In Table 5.1 Left we list the number of GMRES iterations required for convergence to GMRES residual tolerances ϵ using the un-preconditioned system (equation 5.8 with $d = 0$); in Table 5.1 Right, in turn, we present the corresponding number of GMRES iterations required when the value $d = 0.14$ is used in equation 5.8 instead. Using the numerical solution for the problem produced by the un-preconditioned system with ϵ set to 10^{-20} as the basis for evaluation of errors, we compare the errors of the numerical solutions produced by the un-preconditioned and preconditioned systems. The results presented in Table 5.1 demonstrate the advantages resulting from use of the preconditioned system. The preconditioned system can produce a given error in the solution obtained by means of significantly smaller iteration numbers and significantly larger residual tolerances than those required for the corresponding un-preconditioned system to produce a comparable error. This difference becomes more pronounced as the discretization meshes are refined.

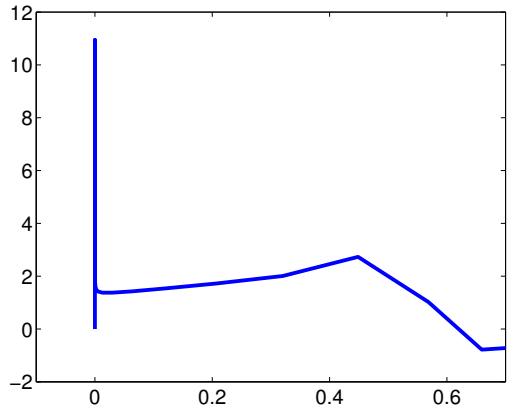

Figure 5.1: Error in the function b arising from use of the un-preconditioned system; residual tolerance $\epsilon = 10^{-12}$

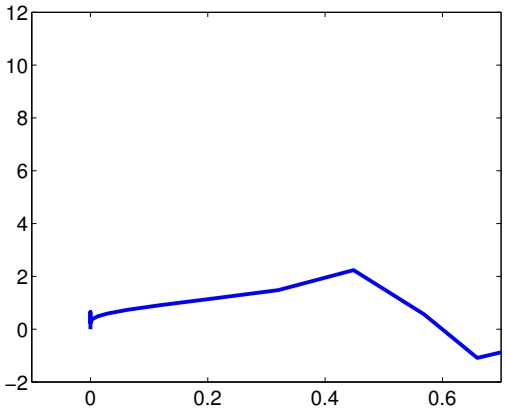

Figure 5.2: Same as Figure 5.1 but with residual tolerance $\epsilon = 10^{-14}$

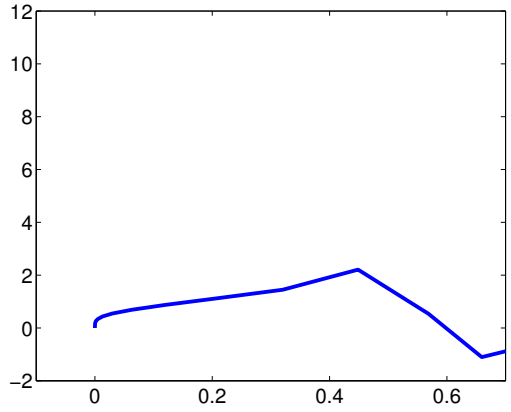

Figure 5.3: Same as Figure 5.1 but with residual tolerance $\epsilon = 10^{-16}$

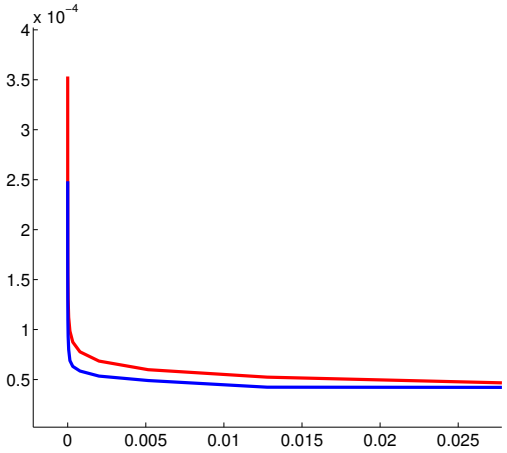

Figure 5.4: Red: error in the function b arising from use of the un-preconditioned system, $\epsilon = 10^{-17}$. Blue: error in the function b arising from use of the preconditioned system, $\epsilon = 10^{-8}$ (compare Table 5.1).

Chapter 6

Computational examples

In this chapter, we present a variety of numerical solutions for our problems. In all cases, the PDE is solved in a domain exterior to a surface containing a conical point, which coincides with a straight cone surface near the conical point. We provide a number of examples of varying degrees of complexity. The program we use to obtain the numerical solutions to equation (1.7) was implemented as a test-bed for our algorithm and our ideas, and has not been optimized or accelerated in any way.

We present numerical solutions for two closed surfaces, namely

1. a **circular-conical-point surface**, depicted in Figure 6.1, which, near the conical point coincides with a straight circular cone (of height = 1 and base-radius = 0.8); and

2. an **elliptical-conical-point surface**, depicted in Figure 6.2, which, near the conical point coincides with a straight elliptic cone (of height = 1, and whose base is an ellipse of major semi-axis = 1.2 and minor semi-axis = 0.8).

In both cases the upper part of the scattering body is a portion of a sphere.

To test our algorithm we consider exterior Neumann problems with two different boundary conditions and associated right hand sides (RHS) $g(x)$:

A. The first RHS is $g(x) = \frac{\partial P_{x_0}(x)}{\partial n}$, where $P_{x_0}(x) = \frac{1}{|x-x_0|}$, and where x_0 lies inside the body and away from its boundary. Note that the function $P_{x_0}(x)$ is a solution of the Laplace equation outside the body. Clearly, then, the solution arising from the first RHS is the function $P_{x_0}(x)$ itself; this case thus provides a valuable test for the accuracy and other properties of our algorithm: the numerical solution $\nu(x)$ of equation (1.7) can be used to evaluate the corresponding numerical values of $v^e(x)$ using equation (1.5),

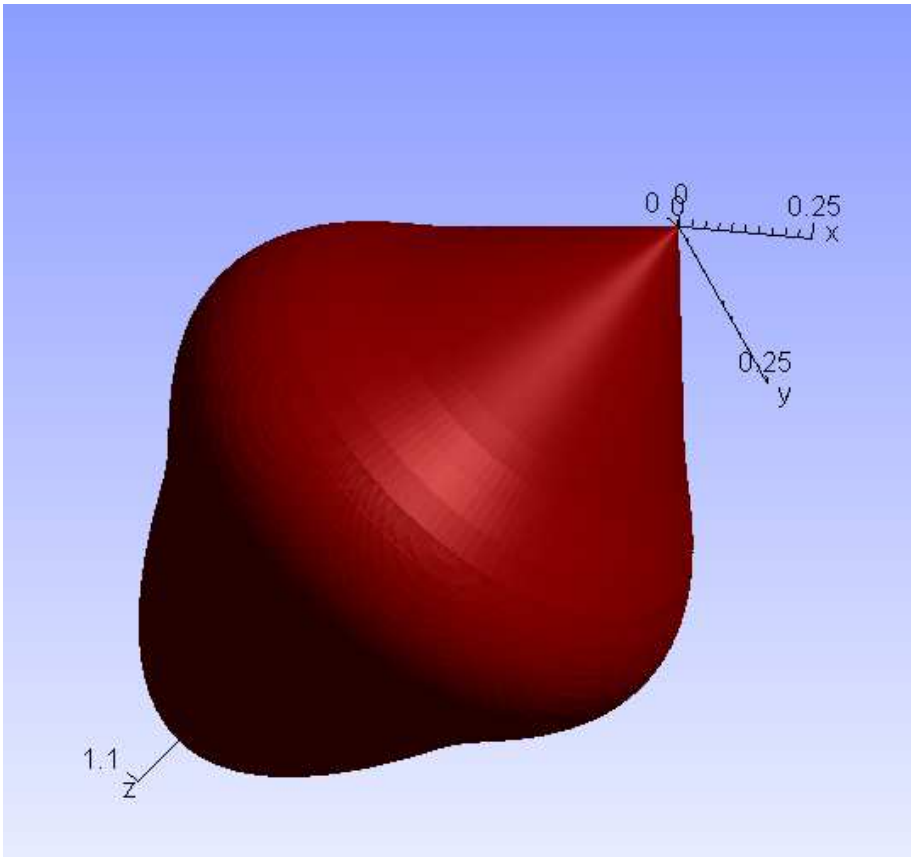

Figure 6.1: The circular-conical-point surface.

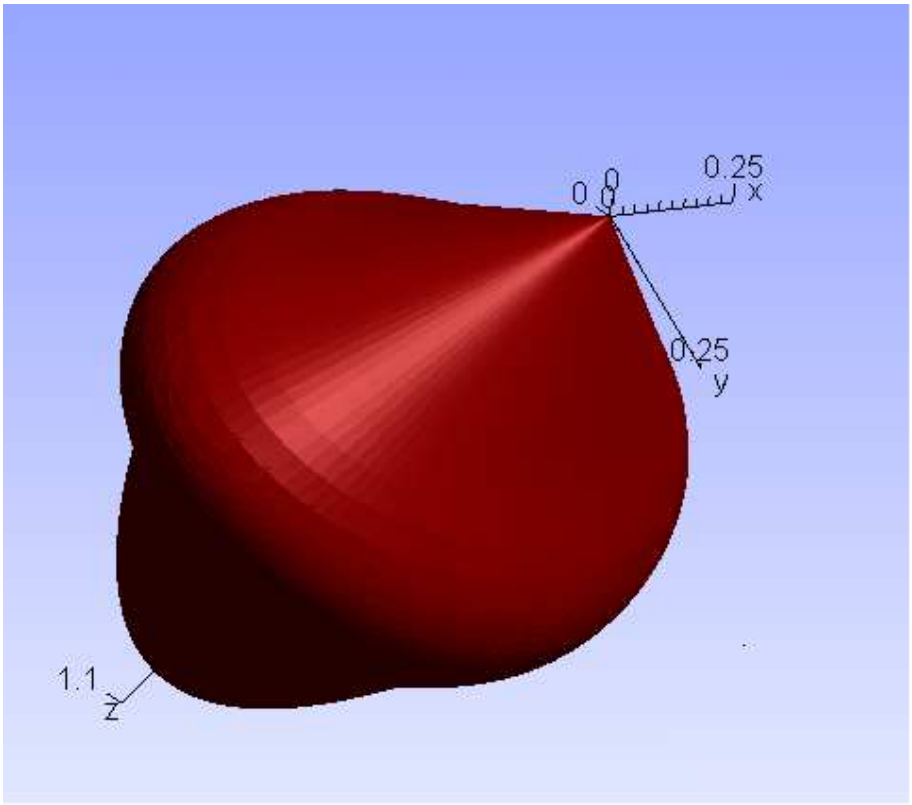

Figure 6.2: The elliptical-conical-point surface.

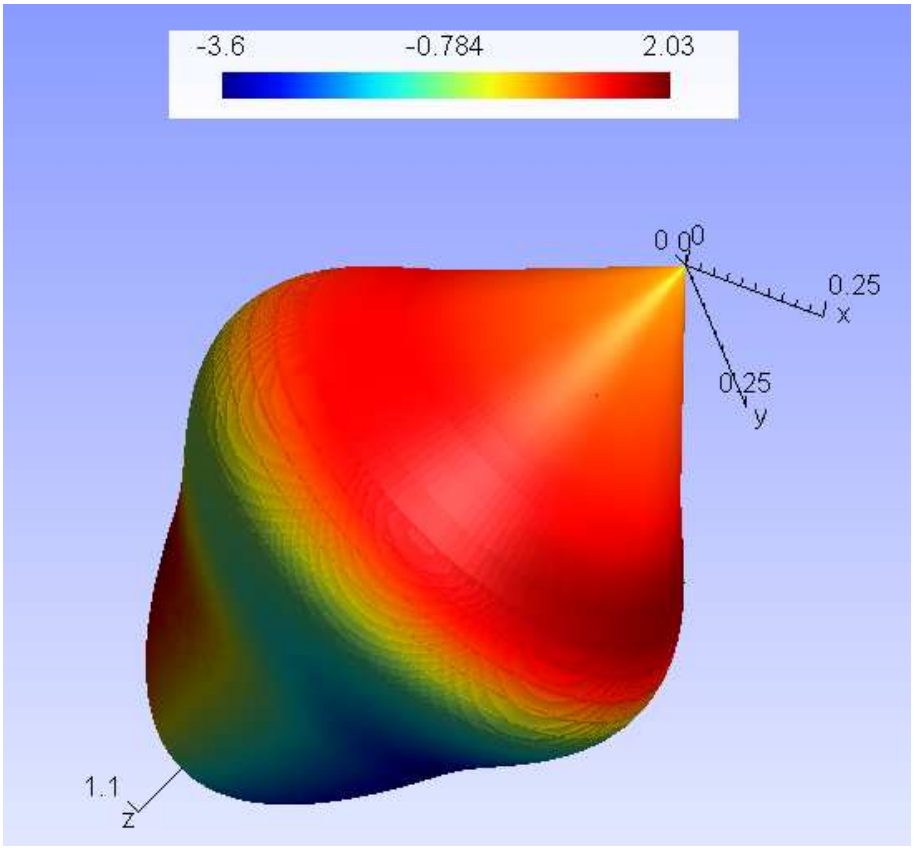

Figure 6.3: Bounded part $b(\boldsymbol{x})$ of the solution for the right-hand-side $\frac{\partial N(x)}{\partial n}$ on the circular-conical-point surface.

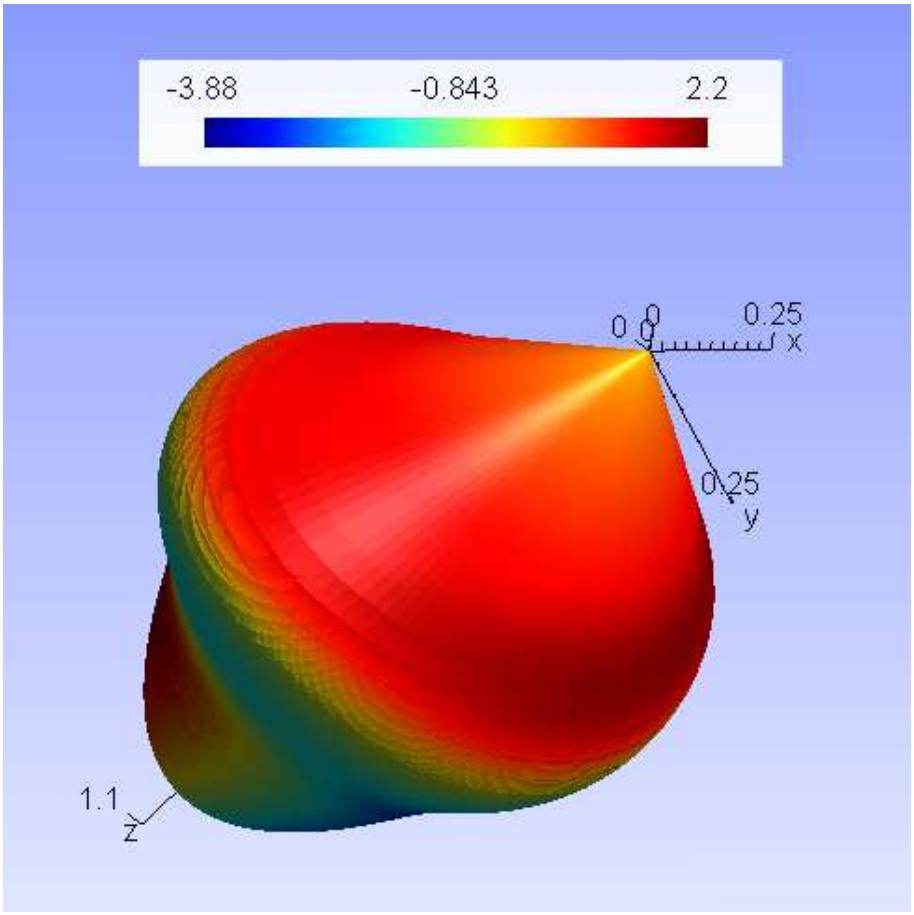

Figure 6.4: Bounded part $b(\boldsymbol{x})$ of the solution for the right-hand-side $\frac{\partial N(x)}{\partial n}$ on the elliptical-conical-point surface.

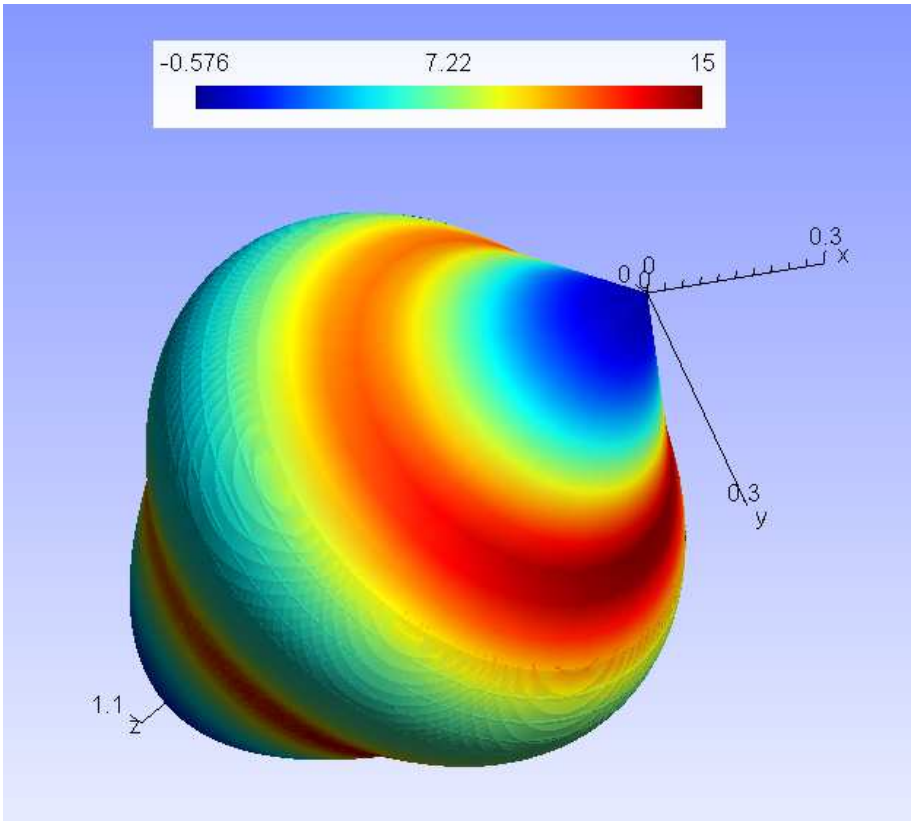

Figure 6.5: Bounded part $b(\boldsymbol{x})$ of the solution for the right-hand-side $\frac{\partial P_{x_0}(x)}{\partial n}$ on the circular-conical-point surface.

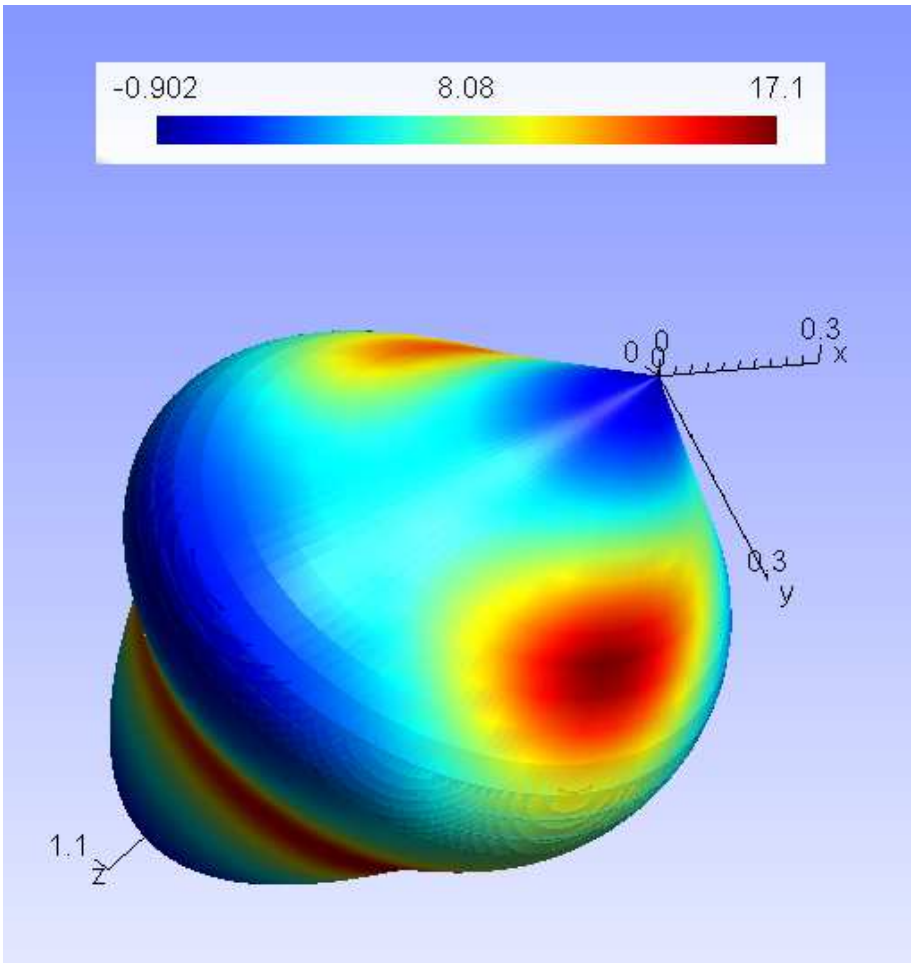

Figure 6.6: Bounded part $b(\boldsymbol{x})$ of the solution for the right-hand-side $\frac{\partial P_{x_0}(x)}{\partial n}$ on the elliptical-conical-point surface.

which can, in turn, be compared with the known analytic solution $P_{x_0}(x)$. We choose $P_0(0.11, 0.12, 0.75)$.

B. The second right hand side is $g(x) = \frac{\partial N(x)}{\partial n}$, where $N(x) = \bar{d} \cdot x$. $\bar{d}$ is an arbitrary direction. We choose $\bar{d} = (1, 2, 3)$.

6.1 Singular pairs: Numerical results

According to Reference [32], for a circular cone with apex angle 2δ, the associated singular exponents are

$$q_1 = q_2 = \Lambda(\cos\delta),$$

where

$$\lambda = \Lambda(x) \quad \text{if and only if } P_\lambda^{m=0}(x) = 0.$$

Here $P_\lambda^m(x)$ is an associated Legendre function of the first kind. It is shown in [32], further, that the associated singular functions are given by $a_1(\theta) = \sin\theta$ and $a_2(\theta) = \cos\theta$.

Using these circular-cone analytical expressions we obtained the "exact" values of the exponents of the singular terms for a circular cone with apex angle equal to $\pi/2$; these are given by $q_1 = q_2 = 0.14283232400194$. Table 6.1 displays the errors (obtained by comparison with this exact value) arising from our numerical evaluation of these exponents by means of the algorithm described in Section 3.1—with various numbers N_{sp} of discretization points.

In order to determine the accuracy with which the vectors $\{a_i^j, i = 1, 2; j = 1, \ldots, N_{sp}\}$ are obtained, in turn, we compute the projection error:

$$a_i^j - \frac{2\pi}{N_{sp}} \sum_{j'=1}^{N_{sp}} a_i^{j'} \cdot \frac{\sin(\theta_{j'})}{\sqrt{\pi}} \frac{\sin(\theta_j)}{\sqrt{\pi}} - \frac{2\pi}{N_{sp}} \sum_{j'=1}^{N_{sp}} a_i^{j'} \cdot \frac{\cos(\theta_{j'})}{\sqrt{\pi}} \frac{\cos(\theta_j)}{\sqrt{\pi}};$$

these errors are displayed in Table 6.2.

N_{sp}	Errors
32	2×10^{-6}
64	3×10^{-7}
128	4×10^{-8}
256	4×10^{-9}
512	5×10^{-10}

Table 6.1: Errors in the numerical values of q_i for a circular cone with apex angle π for various numbers of discretization points N_{sp}.

N_{sp}	Maximum error
4	0.5
8	0.35
16	2×10^{-15}
32	1×10^{-15}

Table 6.2: Maximum error ($0 \leq \theta \leq 2\pi$) in the numerical values of $a_i(\theta)$ for a circular cone with apex angle π for various numbers of discretization points N_{sp}.

6.2 Numerical solution for the circular- and elliptical-conical-point surfaces

In this section we present a number of results for the circular- and elliptical-conical-point surfaces described in points 1. and 2. above; in what follows these surfaces are referred to as surfaces 1. and 2., respectively. In all computations, we set $n_u = 7$ in equation (4.8). The values of the singular exponents resulting from numerical calculations based on the algorithm introduced in Section 3.1 are as follows: $q_1 = q_2 = 0.129333226$ for surface 1, and $q_1 = 0.105667028$ and $q_2 = 0.182260175$ for surface 2. The preconditioner exponents (see Section 5.3), in turn, were taken to equal $d = 0.14$ for surface 1., and $d = 0.19$ for surface 2. In all computations, we set the GMRES residue tolerance $\epsilon = 10^{-8}$.

Figures 6.3 through 6.6 display the values of the regular parts $b(\boldsymbol{x})$ of the solutions $\nu(\boldsymbol{x})$ (cf. equation (3.1)) on the boundary surfaces 1. and 2., for the right hand side (Neumann condition) $g(\boldsymbol{x}) = \frac{\partial N(\boldsymbol{x})}{\partial n}$ and $g(\boldsymbol{x}) = \frac{\partial P_{p_0}(\boldsymbol{x})}{\partial n}$. In Figure 6.7, in turn, we display the values of $b(\boldsymbol{x})$ on the polar line $\theta_{\boldsymbol{x}} = \pi/64$ (selected at a slight departure from $\theta_{\boldsymbol{x}} = 0$ for a degree of generality); in Figure 6.7, we display the values of $b(\boldsymbol{x})$ on azimuthal lines $u^1 = c$ (constant) for the six values of c (four of these constants are also listed in the first columns of Tables 6.3 through 6.5). Note that Figure 6.8 displays values of $b(\boldsymbol{x})$ along a curve that passes through the conical point, and thus, as expected, it has an infinite derivative that is expected there.

We discretize the parameter spaces (u^k, v^k) $(k = 1, 2)$ with an equi-spaced mesh (u^k_h, v^k_h),

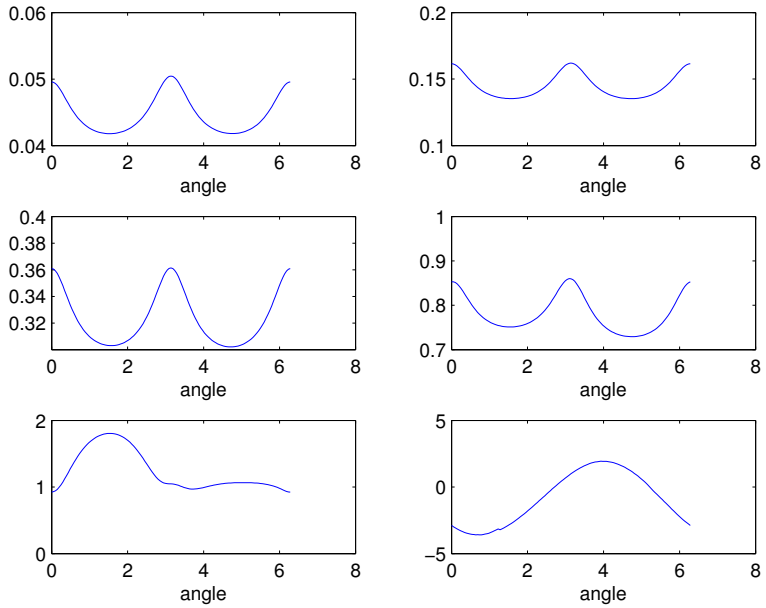

Figure 6.7: Bounded part $b(\boldsymbol{x})$ of the solution on the azimuthal lines $z_{\boldsymbol{x}} = \text{Const.}$ for an elliptical-conical-point body, and RHS $\frac{\partial N(x)}{\partial n}$.

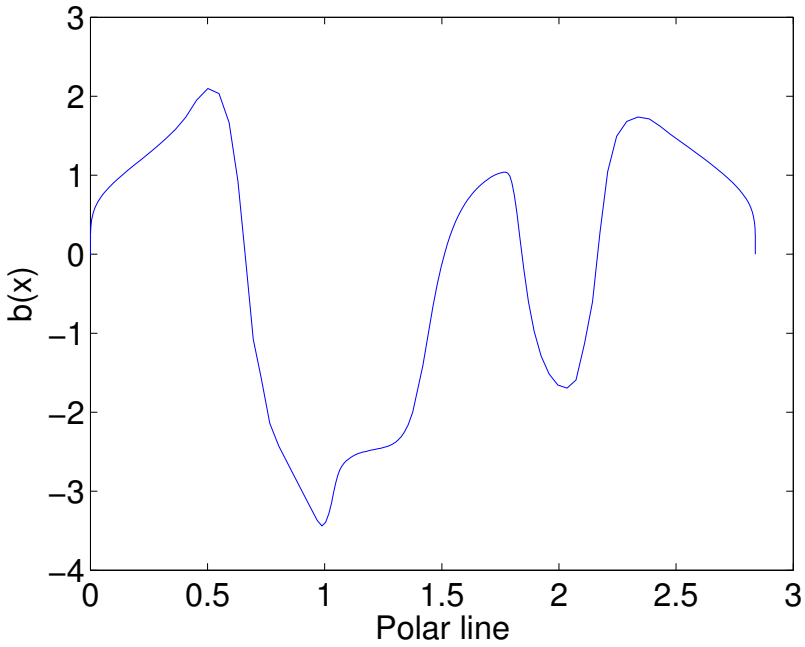

Figure 6.8: Bounded part $b(\boldsymbol{x})$ of the solution on the polar line $\theta_{\boldsymbol{x}} = \pi/64$ for an elliptical-conical-point body, and RHS $\frac{\partial N(x)}{\partial n}$.

	$\theta_{\boldsymbol{x}} = 0$	$\pi/8$	$2\pi/8$	$3\pi/8$	$4\pi/8$	$5\pi/8$	$6\pi/8$	$7\pi/8$
$z_{\boldsymbol{x}} = 4.7 \times 10^{-7}$	0.00913	-0.0021	-0.0043	-0.0007	0.0123	-0.0001	-0.0036	-0.0016
$z_{\boldsymbol{x}} = 6.1 \times 10^{-5}$	0.01186	0.0010	-0.0008	0.0020	0.0137	0.0023	-0.0005	0.0011
$z_{\boldsymbol{x}} = 3.5 \times 10^{-4}$	0.0289	0.0019	-0.003	0.0024	0.0302	0.0026	-0.0028	0.002
$z_{\boldsymbol{x}} = 4.4 \times 10^{-2}$	0.0203	-0.005	-0.0091	-0.0051	0.0220	-0.0040	-0.0077	-0.0043
$z_{\boldsymbol{x}} = 0.24$	0.0756	-0.018	-0.032	-0.013	0.012	-0.0267	-0.026	-0.0314

Table 6.3: Errors (shown at selected mesh points close to the conical point) in the bounded part $b(\boldsymbol{x})$ of the solution of an elliptical-conical-point problem with RHS $\frac{\partial N(x)}{\partial n}$ obtained from a computational mesh containing 16×16 points per patch.

	$\theta_{\boldsymbol{x}} = 0$	$\pi/8$	$2\pi/8$	$3\pi/8$	$4\pi/8$	$5\pi/8$	$6\pi/8$	$7\pi/8$
$z_{\boldsymbol{x}} = 4.7 \times 10^{-7}$	0.0011	-0.0016	-0.0018	-0.0009	0.00278	-0.0008	-0.0017	-0.00158
$z_{\boldsymbol{x}} = 6.1 \times 10^{-5}$	0.00033	-0.0008	-0.0007	-0.0003	0.0013	-0.0003	-0.0007	-0.0008
$z_{\boldsymbol{x}} = 3.5 \times 10^{-4}$	0.0018	-0.0021	-0.0025	-0.0018	0.0025	-0.0018	-0.0025	-0.002
$z_{\boldsymbol{x}} = 4.4 \times 10^{-2}$	-0.0026	-0.0044	-0.0045	-0.0040	-0.0019	-0.0039	-0.004	-0.0043
$z_{\boldsymbol{x}} = 0.24$	-0.0144	-0.020	-0.0184	-0.02	-0.021	-0.017	-0.012	-0.018

Table 6.4: Errors (shown at selected mesh points close to the conical point) in the bounded part $b(\boldsymbol{x})$ of the solution of an elliptical-conical-point problem with RHS $\frac{\partial N(x)}{\partial n}$ obtained from a computational mesh containing 32×32 points per patch.

and use the mesh step sizes $\{1/8, 1/16, 1/32, 1/64, 1/128\}$. The numerical solution resulting from the finest mesh, $h = 1/128$, is used to compute the errors in the solutions obtained on the coarser meshes. To highlight the quality with which our solver evaluates the function b near the conical point, we present the errors at various distances from the conical point. At these distances, we also present the errors on azimuthal lines of the elliptical-conical-point surface, to show how the errors vary in the variable θ for different distances from the conical point.

For the circular-conical-point and elliptical-conical-point surface, Tables 6.6 through 6.13 list errors of the numerical nodal values of $b(\boldsymbol{x})$ and the numerical singular term coefficients values c_k obtained with different mesh sizes. In each table for the error of numerical results of $b(\boldsymbol{x})$, maximum errors on azimuthal lines with various $r_{\boldsymbol{x}}$ coordinate values (column) are

	$\theta_{\boldsymbol{x}} = 0$	$\pi/8$	$1\pi/8$	$5\pi/8$	$7\pi/8$
$z_{\boldsymbol{x}} = 4.7 \times 10^{-7}$	-0.95×10^{-4}	-3.48×10^{-4}	-0.52×10^{-4}	-0.27×10^{-4}	-3.22×10^{-4}
$z_{\boldsymbol{x}} = 6.1 \times 10^{-5}$	-1.32×10^{-4}	-0.72×10^{-4}	1.09×10^{-4}	1.19×10^{-4}	-0.61×10^{-4}
$z_{\boldsymbol{x}} = 3.5 \times 10^{-4}$	0.34×10^{-4}	-0.46×10^{-4}	0.80×10^{-4}	0.82×10^{-4}	-0.44×10^{-4}
$z_{\boldsymbol{x}} = 4.4 \times 10^{-2}$	0.69×10^{-4}	0.62×10^{-4}	1.53×10^{-4}	2.21×10^{-4}	1.32×10^{-4}
$z_{\boldsymbol{x}} = 0.24$	-0.42×10^{-4}	1.17×10^{-4}	3.22×10^{-4}	3.39×10^{-4}	1.17×10^{-4}

Table 6.5: Errors (shown at selected mesh points close to the conical point) in the bounded part $b(\boldsymbol{x})$ of the solution of an elliptical-conical-point problem with RHS $\frac{\partial N(x)}{\partial n}$ obtained from a computational mesh containing 64×64 points per patch.

Mesh points per patch	$z_{\boldsymbol{x}} \sim 10^{-7}$	$z_{\boldsymbol{x}} \sim 10^{-5}$	$z_{\boldsymbol{x}} \sim 10^{-4}$	$z_{\boldsymbol{x}} \sim 10^{-2}$	$z_{\boldsymbol{x}} > 0.24$
8×8	9.8666	4.7239	3.1939	2.5367	1.7536
16×16	0.0123	0.0138	0.0302	0.0220	0.0770
32×32	0.0027	0.0013	0.0025	0.0045	0.0212
64×64	0.0005	0.0002	0.0003	0.0003	0.0023
b_{max}	0.0559	0.1706	0.3818	0.9083	3.4003

Table 6.6: Maximum errors and maximum function values b_{max} on various azimuthal lines $z_{\boldsymbol{x}} = \text{Const.}$ for the bounded part $b(\boldsymbol{x})$ of the solution of an elliptical-conical-point problem with RHS $\frac{\partial N(x)}{\partial n}$ obtained from meshes of varying degrees of fineness.

Mesh points per patch	Error
8×8	0.3066
16×16	0.0813
32×32	0.0148
64×64	0.00114

Table 6.7: Errors on the numerical values of the singular-term coefficients c_1 and c_2 for an elliptical-conical-point problem with RHS $\frac{\partial N(x)}{\partial n}$, obtained from meshes of varying degrees of fineness (the coefficients obtained from the finest (128×128) mesh are $c_1 = 19.197$ and $c_2 = -42.1$).

presented.

Finally, using the computed integral density ν on the 128×128 mesh, equation (1.5) and Simpson's rule we produce our numerical solution $v^e(\boldsymbol{x})$ of the exterior Neumann problem with Neumann data $g(\boldsymbol{x}) = \frac{\partial P_{p_0}(\boldsymbol{x})}{\partial n}$ on the elliptical-conical-point surface. The errors of the numerical values of $v^e(\boldsymbol{x})$, which were computed by comparison with the analytical solution $v^e(\boldsymbol{x}) = P_{p_0}(\boldsymbol{x})$, are displayed in Table 6.14. This table gives the values of the numerical errors on points outside the region D around the conical point with various $r_{\boldsymbol{x}}$ and $\theta_{\boldsymbol{x}}$ coordinates. In Table 6.15, we show errors of the numerical $v^e(\boldsymbol{x})$ computed on points outside the region D, tending to a point on the boundary surface ∂D. Clearly, the quality of the solutions is very high indeed.

Mesh points per patch	$z_{\boldsymbol{x}} \sim 10^{-7}$	$z_{\boldsymbol{x}} \sim 10^{-5}$	$z_{\boldsymbol{x}} \sim 10^{-4}$	$z_{\boldsymbol{x}} \sim 10^{-2}$	$z_{\boldsymbol{x}} > 0.24$
8×8	0.9460	0.5248	0.4424	2.0339	1.4312
16×16	0.0073	0.0072	0.0159	0.0505	0.6833
32×32	0.0027	0.0027	0.0036	0.0124	0.1972
64×64	0.0008	0.0005	0.0005	0.0004	0.0073
b_{max}	0.0010	0.0007	0.0046	1.4950	12.1382

Table 6.8: Maximum errors and maximum function values b_{max} on various azimuthal lines $z_{\boldsymbol{x}} = \text{Const.}$ for the bounded part $b(\boldsymbol{x})$ of the solution of an elliptical-conical-point problem with RHS $\frac{\partial P_{x_0}(x)}{\partial n}$ obtained from meshes of varying degrees of fineness.

Mesh points per patch	Error
8×8	3.6566
16×16	0.6631
32×32	0.0540
64×64	0.0036

Table 6.9: Maximum of the errors on the numerical values of the singular-term coefficients c_1 and c_2 for an elliptical-conical-point problem with RHS $\frac{\partial P_{x_0}(x)}{\partial n}$, obtained from meshes of varying degrees of fineness (the exact singular coefficients are $c_1 = 0$ and $c_2 = 0$).

Mesh points per patch	$z_{\boldsymbol{x}} \sim 10^{-7}$	$z_{\boldsymbol{x}} \sim 10^{-5}$	$z_{\boldsymbol{x}} \sim 10^{-4}$	$z_{\boldsymbol{x}} \sim 10^{-2}$	$z_{\boldsymbol{x}} > 0.24$
8×8	3.3375	2.1740	1.4186	1.0461	1.1225
16×16	0.0266	0.0186	0.0112	0.0139	0.0395
32×32	0.0060	0.0027	0.0034	0.0059	0.0115
64×64	0.0016	0.0007	0.0005	0.0004	0.0008
$b_{max}(\boldsymbol{x})$	0.0762	0.1861	0.3551	0.7251	1.1040

Table 6.10: Maximum errors and maximum function values b_{max} on various azimuthal lines $z_{\boldsymbol{x}} = \text{Const.}$ for the bounded part $b(\boldsymbol{x})$ of the solution of a circular-conical-point problem with RHS $\frac{\partial N(x)}{\partial n}$ obtained from meshes of varying degrees of fineness.

Mesh points per patch	Error
8×8	-13.9034
16×16	-0.0237
32×32	-0.0067
64×64	-0.0032

Table 6.11: Maximum of the errors on the numerical values of the singular-term coefficients c_1 and c_2 for an circular-conical-point problem with RHS $\frac{\partial N(x)}{\partial n}$, obtained from meshes of varying degrees of fineness (the coefficients obtained from the finest (128×128) mesh are $c_1 = -23.00635$ and $c_230.56074$).

Mesh points per patch	$z_{\boldsymbol{x}} \sim 10^{-7}$	$z_{\boldsymbol{x}} \sim 10^{-5}$	$z_{\boldsymbol{x}} \sim 10^{-4}$	$z_{\boldsymbol{x}} \sim 10^{-2}$	$z_{\boldsymbol{x}} > 0.24$
8×8	3.7787	2.5741	1.8566	2.3220	1.7998
16×16	1.1428	0.6760	0.4577	0.2980	1.0821
32×32	0.0036	0.0041	0.0060	0.0153	0.2157
64×64	0.0008	0.0005	0.0004	0.0005	0.0098
$b_{max}(\boldsymbol{x})$	0.0009	0.0006	0.0007	0.7837	11.5502

Table 6.12: Maximum errors and maximum function values b_{max} on various azimuthal lines $z_{\boldsymbol{x}} = \text{Const.}$ for the bounded part $b(\boldsymbol{x})$ of the solution of a circular-conical-point problem with RHS $\frac{\partial P_{x_0}(x)}{\partial n}$ obtained from meshes of varying degrees of fineness.

Mesh points per patch	Error
8×8	20.9947
16×16	5.1226
32×32	0.0592
64×64	0.0028

Table 6.13: Maximum of the errors on the numerical values of the singular-term coefficients c_1 and c_2 for an circular-conical-point problem with RHS $\frac{\partial P_{x_0}(x)}{\partial n}$, obtained from meshes of varying degrees of fineness (the exact singular coefficients are $c_1 = 0$ and $c_2 = 0$).

	$\theta_{\boldsymbol{x}} = \pi/5$	$\theta_{\boldsymbol{x}} = 2\pi/5$	$\theta_{\boldsymbol{x}} = 3\pi/5$	$\theta_{\boldsymbol{x}} = 4\pi/5$
$r_{\boldsymbol{x}} = 1$	9.02×10^{-5}	7.79×10^{-5}	7.56×10^{-5}	8.19×10^{-5}
$r_{\boldsymbol{x}} = 2$	5.83×10^{-5}	5.18×10^{-5}	5.05×10^{-5}	5.41×10^{-5}
$r_{\boldsymbol{x}} = 3$	4.23×10^{-5}	3.85×10^{-5}	3.77×10^{-5}	3.99×10^{-5}
$r_{\boldsymbol{x}} = 4$	3.30×10^{-5}	3.06×10^{-5}	3.01×10^{-5}	3.15×10^{-5}

Table 6.14: Errors in the solution $v^e(\boldsymbol{x})$ of the exterior Neumann problem on an elliptical-conical-point surface, at various points outside the body (characterized by their $r_{\boldsymbol{x}}$ and $\theta_{\boldsymbol{x}}$ coordinates).

distance to p_k	p_1	p_2
1e-1	18.1×10^{-5}	14.7×10^{-5}
1e-2	6.91×10^{-5}	16.3×10^{-5}
1e-3	44.3×10^{-5}	15×10^{-5}
1e-4	49.1×10^{-5}	112×10^{-5}
1e-5	49.6×10^{-5}	112×10^{-5}
1e-6	49.6×10^{-5}	112×10^{-5}
1e-10	49.6×10^{-5}	112×10^{-5}

Table 6.15: Errors in the solution $v^e(\boldsymbol{x})$ of the exterior Neumann problem for an elliptical-conical-point surface, at points outside the body limiting at $p_1(-0.33, 0.24, 0.53)$ and $p_2(0.38, 0, 0.32)$. The corresponding solution values are $v^e(p_1) = 1.54$ and $v^e(p_2) = 1.95$.

Chapter 7

Conclusions

We have introduced a new method for the evaluation of singular solutions of the Laplace equation in domains whose boundaries contain conical singularities. Our algorithm evaluates the most singular terms of the solution separately and with high accuracy, on the basis of a method of regularization related to a certain cancellation of infinities. This procedure allows us to treat the remaining (smoother) integrands by means of a high order scheme, thus giving rise to solutions with a high degree of accuracy.

As far as we know, these are by far the most accurate solutions to date for the cases we considered, namely, solutions of the Laplace equation in three dimensional space, which blow up at a conical point of general cross section. For example, Reference [32] only provides the singular part of the solution for the case of a circular conical point. Reference [5], which provides the full solution for a general geometrical singularity, only treats cases in which the solution is *bounded*, and results in accuracies of low-order. Similar accuracy issues exist in Reference [31]. We believe the accuracy gains resulting from the methods introduced in this thesis for blow-up solutions at conical points are very significant indeed.

A number of issues associated with our problem have been left for future work. These include 1) Matters associated with the ill-conditioning arising at the conical points and requirement of large numbers of iterations in the iterative linear algebra solver: the pre-conditioner introduced in Chapter 5 has only partially alleviated this problem. Future contributions should also include 2) A generalization of the methodologies introduced in this work to cases in which the boundary surface *does not* coincide with the boundary of a straight cone near the conical point. To deal with such cases a detailed theoretical treatment of the perturbations induced by the departure from a straight cone geometry must be undertaken. An additional

item of interest concerns 3) Extension of the methodology developed to produce the most singular term in the integral-equation solution to enable evaluation of a full asymptotic expansion for it. Such a result should enable us to improve the conditioning issues mentioned in point 1) above, and, we expect, it allows one to tackle problems containing conical points of small spherical angle without requiring inordinately large numbers of iterations. Certainly, 4) Extensions of the ideas introduced in this thesis to other singular problems, including the Maxwell equations and the elasticity equations, should prove useful in a range of areas of science and engineering.

Appendix A

Parameterizations of the patches $\mathcal{P}^k$ and the fixed POU functions

The auxiliary one-dimensional function $P(x, t_1, t_0)$, which is depicted in Figure 2.4, should smoothly vary from 1 to 0 between t_1 and t_0 and be infinitely smooth for all real values of x; a possible such function is given by the expression

$$P(x,t_1,t_0) = \begin{cases} 1 & x < t_1 \\ e^{\frac{2.56085}{\frac{x-t_0}{t_1-t_0}-1} \times e^{-\frac{t_1-t_0}{x-t_0}}} & t_1 < x < t_0 \\ 0 & x > t_0; \end{cases} \tag{A.1}$$

see [6].

Using the auxiliary function (A.1) we construct our model surface and its associated partition of unity. The mapping $(x^1, y^1, z^1)\boldsymbol{x}^1(u^1, v^1)$ from the domain $(u^1, v^1) \in \mathcal{H}^1 = [0,1] \times [0,1]$ to the patch $\mathcal{P}^1$ (which we use, indeed, to define this patch) is constructed follows: we first map the domain $\mathcal{H}^1$ to the surface of a straight cone by means of the transformation

$$\begin{cases} \tilde{x}^1 &= h \cdot (u^1)^{n(u^1)} \sin\phi(2\pi v^1) \cos 2\pi v^1 \\ \tilde{y}^1 &= h \cdot (u^1)^{n(u^1)} \sin\phi(2\pi v^1) \cos 2\pi v^1, \\ \tilde{z}^1 &= h \cdot (u^1)^{n(u^1)} \end{cases} \tag{A.2}$$

where h is the height of the straight cone surface, and where $\phi(2\pi v^1)$ describes the shape of the straight cone surface. Here, $(u^1)^{n(u^1)}$ is the change of variable displayed in equation (4.7). We then deform the cone so as to prepare it for addition of a sphere top; a com-

plete parametrization for the deformed cone patch $\mathcal{P}^1$ (as a function of u^1 and v^1; see (A.2)) is given by

$$\begin{cases} x^1 & = \tilde{x}^1 \cdot P(\frac{\tilde{z}^1}{h}, t_1, t_0) + \sqrt{(h+d)^2 - (d+\tilde{z}^1)^2} \cdot \frac{\tilde{x}^1}{\sqrt{(\tilde{x}^1)^2+(\tilde{y}^1)^2}} \cdot P(1 - \frac{\tilde{z}^1}{h}, t_1, t_0), \\ y^1 & \tilde{y}^1 \cdot P(\frac{\tilde{z}^1}{h}, t_1, t_0) + \sqrt{(h+d)^2 - (d+\tilde{z}^1)^2} \cdot \frac{\tilde{y}^1}{\sqrt{(\tilde{x}^1)^2+(\tilde{y}^1)^2}} \cdot P(1 - \frac{\tilde{z}^1}{h}, t_1, t_0), \\ z^1 & = \tilde{z}^1. \end{cases} \tag{A.3}$$

Here $d > 0$ is a parameter for the sphere surface to be attached: the sphere is centered at $(0, 0, -d)$ and has radius $h + d$. The quantities $0 < t_1 < t_0 < 1$ are two parameters defining the points at which the conical surface and the sphere surface are joined. The fixed POU function $\omega^1(\boldsymbol{x}^1(u^1, v^1))$ on patch $\mathcal{P}^1$ is, quite simply, given by

$$\omega^1(\boldsymbol{x}^1(u^1, v^1)) = P(\frac{z^1}{h}, t_1, t_0). \tag{A.4}$$

To describe the mapping $(x^2, y^2, z^2) = \boldsymbol{x}^2(u^2, v^2)$ from the domain $(u^2, v^2) \in \mathcal{H}^2 = [0, 1] \times [0, 1]$ to the patch $\mathcal{P}^2$, we first map $\mathcal{H}^2$ to the surface of the sphere centered at $(0, 0, -d)$ with radius $h + d$:

$$\begin{cases} \tilde{x}^2 & = 2u^2 - 1 \\ \tilde{y}^2 & = 2v^2 - 1 \\ \tilde{z}^2 & \sqrt{(h+d)^2 - ((\tilde{x}^2)^2 + (\tilde{y}^2)^2)} - d. \end{cases} \tag{A.5}$$

Then we deform the sphere surface so as to match it with $\mathcal{P}^1$; and we thus obtain the parametrization of the patch $\mathcal{P}^2$:

$$\begin{cases} x^2 & = \tilde{x}^2 \cdot P(1 - \frac{\tilde{z}^2}{h}, t_1, t_0) + \tilde{z}^2 \cdot \tan(\phi(\arctan(\tilde{x}^2, \tilde{y}^2)) \cdot \frac{\tilde{x}^2}{\sqrt{(\tilde{x}^2)^2+(\tilde{y}^2)^2}} \cdot P(\frac{\tilde{z}^2}{h}, t_1, t_0) \\ y^2 & = \tilde{y}^2 \cdot P(1 - \frac{\tilde{z}^2}{h}, t_1, t_0) + \tilde{z}^2 \cdot \tan(\phi(\arctan(\tilde{x}^2, \tilde{y}^2)) \cdot \frac{\tilde{y}^2}{\sqrt{(\tilde{x}^2)^2+(\tilde{y}^2)^2}} \cdot P(\frac{\tilde{z}^2}{h}, t_1, t_0), \\ z^2 & = \tilde{z}^2. \end{cases} \tag{A.6}$$

(Here, $\arctan(\tilde{x}^2, \tilde{y}^2)$ maps a point $(\tilde{x}^2, \tilde{y}^2)$ to the angle between the positive x-axis and the line crossing the origin O and point $(\tilde{x}^2, \tilde{y}^2)$.) The fixed POU function $\omega^2(\boldsymbol{x}^2(u^2, v^2))$ is defined as

$$\omega^2(\boldsymbol{x}^2(u^2, v^2)) = P(\frac{z^2}{h}, t_1, t_0). \tag{A.7}$$

Bibliography

[1] F. Assous, P. Ciarlet, and S. Labrunie. Theoretical tools to solve the axisymmetric Maxwell equations. *Math. Methods in the Appl. Sci.*, Vol. 25 No. 1:49–78, 2002.

[2] F. Assous, P. Ciarlet, Jr., and J. Segre. Numerical solution to the time-dependent Maxwell equations in two-dimensional singular domains: The singular complement method. *J. of Comp. Phys.*, Vol. 161:218–249, 2000.

[3] I. Babuska, R.B. Kellogg, and J. Pitkaranta. Direct and inverse error estimates for finite elements with mesh refinements. *Numer. Math.*, Vol. 33:447–471, 1979.

[4] I. Babuska and A. Miller. The post-processing approach in the finite element method-Part 2: the calculation of stress intensity factors. *Int. j. numer. methods eng.*, Vol. 20:1111–1129, 1984.

[5] I. Babuska, T. von Petersdorff, and B. Anderson. Numerical treatment of vertex singularities and intensity factors for mixed boundary value problems for the Laplace equation in $\mathbb{R}^3$. *SIAM J. on Numer. Anal.*, Vol. 31, No. 5:1265–1288, Oct., 1994.

[6] O.P. Bruno and L.A. Kunyansky. A fast, high-order algorithm for the solution of surface scattering problems: Basic implementation, tests, and applications. *J. of Comp. Phys.*, Vol. 169:80–110, 2001.

[7] P. Ciarlet, Jr., B. Jung, S. Kaddouri, S. Labrunie, and J. Zou. The Fourier singular complement method for the Poisson problem. II. Axisymmetric domains. *Numer. Math.*, 102(4):583–610, 2006.

[8] L.J. Clancy. *Aerodynamics*. Pitman Publishing Limited, London, 1975.

[9] D. Colton and R. Kress. *Integral Equation Methods in Scattering Theory*. John Wiley & Sons, 1983.

[10] D. Colton and R. Kress. *Inverse Acoustic and Electromagnetic Scattering Theory*. Springer, 1997.

[11] M. Costabel and M. Dauge. General edge asymptotics of solutions of second-order elliptic boundary value problems I. *Proceedings of the Royal Society of Edinburgh*, Vol. 123A:109–155, 1993.

[12] M. Costabel and M. Dauge. General edge asymptotics of solutions of second-order elliptic boundary value problems II. *Proceedings of the Royal Society of Edinburgh*, Vol. 123A:157–184, 1993.

[13] M. Costabel and M. Dauge. Singularities of electromagnetic fields in polyhedral domains. *Arch. Rational Mech. Anal.*, Vol. 151:221–276, 2000.

[14] J.M. Cowley. *Diffraction physics*. North-Holland, 1975.

[15] C.L. Cox and G.J. Fix. On the accuracy of least square methods in the presence of corner singularities. *Comp. Math. Appl.*, Vol. 10:463–471, 1984.

[16] L. Demkowitz, P. Devloo, and J.T. Oden. On an h-type mesh refinement strategy based on a minimization of interpolation error. *Comp. Methods Appl. Mech. Eng.*, Vol. 53 No. 3:67–89, 1983.

[17] P.R. Devloo. Recursive elements, an inexpensive solution process for resolving point singularities in elliptic problems. *Proc. 2nd World Congress on Computational Mechanics, Stuttgart, Germany, 1990, IACM,*, pages 609–612, 1990.

[18] E. Erdogan. Fracture mechanics. *Int. J. of Sol. and Str.*, Vol. 27:171–183, 2000.

[19] E.B. Fabes, M. Jodeit, and J.E. Lewis. Double layer potentials for domains with corners and edges. *Indiana university mathematics journal*, Vol. 26 No. 1:95–114, 1977.

[20] G.J. Fix, S. Gulati, and G.I. Wakoff. On the use of singular function with finite element approximations. *J. Comp. Phys.*, Vol. 13:209–228, 1973.

[21] A.A. Griffith. The phenomena of rupture and flow in solids. *Phil. Trans. Roy. Soc. Lond.*, Vol. 221:163–198, 1920.

[22] P. Grisvard. *Elliptic Problems in Nonsmooth Domains*. Pitman Advanced Publishing Program, 1985.

[23] J. Helsing. Corner singularities for elliptic problems: special basis functions versus 'brute force'. *Comm. in Numer. Methods in Eng.*, Vol. 16:37–46, 2000.

[24] T.J.R. Hughes and J.E. Akin. Techniques for developing 'special' finite element shape function with particular reference to singularities. *Int. J. Numer. Methods Eng.*, Vol. 15:733–751, 1980.

[25] G. Irwin. Analysis of stresses and strains near the end of a crack traversing a plate. *J. of Appl. Mech.*, 24:361–364, 1957.

[26] J.B. Keller, D. Givoli, and L. Rivkin. A finite element method for domains with corners. *Int. J. for Numer. Methods in Eng.*, Vol. 35:1329–1345, 1992.

[27] R. Kress. A Nyström method for boundary integral equations in domains with corners. *Numer. Math.*, Vol. 58:145–161, 1990.

[28] A.M. Kuethe and J.D. Schetzer. *Foundations of Aerodynamics*. John Wiley & Sons, 1959.

[29] K.Y. Lin and P. Tong. Singular finite elements for the fracture analysis of V-notched plate. *Int. J. Numer. Methods Eng.*, Vol. 15:1343–1354, 1980.

[30] M. Maischak and E.P.Stephan. The hp-version of the boundary element method in $\mathbb{R}^3$ the basic approximation results. *Mathematical Methods in the Applied Sciences*, Vol. 20:461–476, 1997.

[31] M. Maischak, P. Mund, and E.P. Stephan. Adaptive multilevel BEM for acoustic scattering. *Comp. Methods Appl. Mech. Engrg.*, Vol. 150:351–367, 1997.

[32] V.G. Maz'ya and A.V. Levin. Asymptotics of densities of harmonic potentials near the vertex of a cone. *Z. Anal. Anwend.*, Vol. 8, No. 6:501–514, 1989.

[33] B. Nkemzi. On the solution of Maxwell's equations in axisymmetric domains with edges. *Z. Angew. Math. Mech.*, Vol. 85 No. 8:571–592, 2005.

[34] B. Nkemzi. Optimal convergence recovery for the Fourier-finite-element approximation of Maxwell's equations in non-smooth axisymmetric domains. *Appl. Numer. Math.*, Vol. 57 No. 89:989–1007, 2007.

[35] E. Orowan. Fracture and strength of solids. *Reports on Progress in Physics XII*, pages 185–232, 1948.

[36] P. Park. *Multiscale Numerical Methods for the Singularly Perturbed Convection-Diffusion Equation*. PhD thesis, California Institute of Technology, Caltech, CA 91125, 2000.

[37] T.V. Petersdorff and E.P. Stephan. Decompositions in edge and corner singularities for the solution of the Dirichlet problem of the Laplacian in a polyhedron. *Math. Nachr.*, Vol. 149:71–104, 1990.

[38] F. Reitich. Singular solutions of a transmission problem in plane linear elasticity for wedge-shaped regions. *Numer. Math.*, Vol. 59:179–216, 1991.

[39] V.P. Smyshlyaev. The high-frequency diffraction of electromagnetic waves by cones of arbitrary cross sections. *SIAM J. on Appl. Math.*, Vol. 53, No. 3:670–688, 1993.

[40] M. Stern. Families of consistent conforming elements with singular derivative field. *Int. J. Numer. Methods Eng.*, Vol. 14:409–421, 1979.

[41] H.C. van de Hulst. *Light scattering by small particles*. Dover publications, Inc. New York, 1981.

[42] G. Verchota. Layer potentials and regularity for the Dirichlet problem for Laplace's equation in Lipschitz domains. *J. of Func. Anal.*, Vol 59:572–611, 1984.

[43] W. Wasow. Asymptotic development of the solution of Dirichlet's problem at analytic corners. *Duke Math. Journal*, Vol. 24:47–56, 1957.

[44] X. Wu and H. Han. A finite-element method for Laplace- and Helmholtz-type boundary value problems with singularities. *SIAM J. Numer. Anal.*, vol. 34:1037–1050, 1997.

[45] X. Wu and W. Xue. Discrete boundary conditions for elasticity problems with singularities. *Comp. Methods Appl. Mech. Engrg.*, Vol. 192:3777–3795, 2003.

[46] L.A. Ying. Infinite element method for the exterior problems of the Helmholtz equations. *J. of Comp. Math.*, Vol. 18 No. 6:657–672, 2000.